

Final Report

ULTRA-HIGH ALTITUDE MEASUREMENT SYSTEMS FOR
PRESSURE, DENSITY, TEMPERATURE, AND WINDS

Prepared for
George C. Marshall Space Flight Center
Huntsville, Alabama

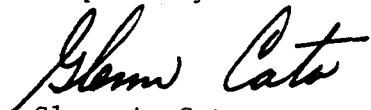
Contract NAS8-5226, TP3-81046 (IF)

EOS Report 3780-Final

15 January 1964

cy 2

Prepared by



Glenn A. Cato
Project Supervisor

Approved by



M.B. Prince, Manager
AEROSPACE ELECTRONICS DIVISION

ELECTRO-OPTICAL SYSTEMS, INC. - PASADENA, CALIFORNIA

FOREWORD

This final report covers the study program conducted from February to November 1963 on contract NAS 8-5226. The work was performed at Electro-Optical Systems, Inc. by the staff of the Aerospace Electronics Division. The Project Supervisor was G. A. Cato. The following persons assisted in the program and the preparation of this report: M. L. Dalton, J. M. Palmer, J. D. Van Putten, K. D. Nichols, C. Skinner, W. J. Swenson and A. Y. Yahiku. The program was under the technical direction of Mr. John Baur of the NASA-George Marshall Space Flight Center.

ABSTRACT

16714

Methods of measuring the properties of the free atmosphere from on board a large launch vehicle such as Saturn are evaluated. The properties to be measured are pressure, temperature, density and wind of the undisturbed atmosphere above 30 km. Measurement techniques and instrumentation are recommended for each property with special emphasis on remote measurement techniques, wherein the instrument is located aboard the vehicle but the measurement actually is made beyond the shock layer.

Author

CONTENTS

1.	INTRODUCTION	1
2.	CONCLUSIONS AND RECOMMENDATIONS	2
	2.1 Conclusions	2
	2.2 Recommendations for Onboard Instruments	2
	2.3 Recommendations for Dropsonde Instruments	3
3.	MEASUREMENT SYSTEM REQUIREMENTS	7
	3.1 Instrument Requirements	7
	3.1.1 Range	7
	3.1.2 Accuracy Requirements	8
	3.1.3 Resolution	10
	3.1.4 Frequency	10
	3.1.5 Time Constant	13
	3.1.6 Vibration and Shock	18
	3.1.7 Sustained Acceleration	18
	3.1.8 Temperature	18
	3.1.9 Size and Weight	19
	3.1.10 Power Consumption	19
	3.1.11 Output	19
	3.2 Measurement Technique Requirements	19
4.	PRESENT SYSTEMS	24
5.	DENSITY	31
	5.1 Ultraviolet Air Density Gage	32
	5.1.1 Theory	34
	5.1.2 Received Signal Strength	36
	5.1.3 Sky Background	36
	5.1.4 Ultraviolet Source Type	37
	5.1.5 Ultraviolet Source Configuration	38
	5.1.6 Detector	40
	5.1.7 Instrument Circuit	43
	5.1.8 Error Sources	43

CONTENTS (cont)

5.1.8.1	Background Error Suppression	45
5.1.8.2	Nonlinearity	46
5.1.9	Accuracy	46
5.1.10	Calibration	51
5.1.10.1	Calibration Apparatus	51
5.1.10.2	Requirements on the Technique	51
5.1.10.3	Calibration Procedure	51
5.1.11	Operation Below 75 km	52
5.1.12	Instrument Location	52
5.2	Filter Photometer Air Density Gage	54
5.2.1	Theory	54
5.2.2	Wavelength Selection	55
5.2.3	Optical Materials	62
5.2.3.1	Windows	62
5.2.3.2	Filter Materials	62
5.2.4	Incident Energy	64
5.2.5	Detector Selection	64
5.2.6	Background Radiation	66
5.2.7	Errors	67
5.2.7.1	Outgassing	67
5.2.7.2	Detector Drift	68
5.2.7.3	Absolute Energy Calibration	69
5.2.7.4	Atmospheric Dust	69
5.2.8	Electronics	69
5.2.9	Data Processing	71
5.2.10	Instrument Calibration	73
5.2.11	Instrument Configuration	74
5.3	Electron Beam Density Gage	77
5.3.1	Penetration Distance	79
5.3.2	Signal Strength	79
5.3.3	Background	81

CONTENTS (cont)

5.3.3.1	Photomultiplier Tube Noise	81
5.3.3.2	Light from the Day Sky	82
5.3.4	Scattering	82
5.3.5	Effect of Electron Beam Energy	83
5.3.6	Electron Gun	86
5.3.7	Conclusions	86
5.4	Backscatter Density Gage	86
5.5	X-Ray Density Gage	90
5.6	Ionization Gage	91
6.	PRESSURE	93
6.1	Pitot-Static Probe	93
6.2	Hypsometer	94
6.3	Risesonde	95
6.4	Radioactive Gas Puffs	96
6.5	Calculation	97
7.	TEMPERATURE	100
7.1	Total Temperature Tube	100
7.2	Acoustic Meter	100
7.3	Resistance Thermometer	104
7.4	Vortex Thermometer	105
7.5	Calculation	105
7.6	Natural Radiation	106
8.	WIND	109
8.1	Fixed Cone	110
8.1.1	Theory	110
8.1.2	Use of F-16 Q-Ball	112
8.2	Electro-Optical Data Pickoff	113
8.2.1	Light Beam Deflection Technique	114
8.2.2	Light Intensity Change Technique	119
8.2.3	Interferometric Technique	122
8.2.4	Index of Refraction Change Technique	122

CONTENTS (cont)

8.3 Spin Pressure Modulation	123
8.3.1 Spin-Pressure-Modulation Technique	125
8.3.2 Expected Pressure-Peak Displacement	125
8.3.3 Detecting Shift of Pressure Peak	127
8.3.4 Rate of Spin	127
8.3.5 Calculation of Wind Speed and Direction	129
8.4 Internal Accelerometers	131
8.5 Wind Sphere	132
8.5.1 Instrument Drive Range	132
8.5.2 Required Response Speed	133
8.5.3 Vibration	133
8.5.4 Sustained Acceleration	133
8.5.5 Wind Pressure	133
8.5.6 Pressure Equivalent of Acceleration	134
8.5.7 Pressure Equivalent of Vibration	135
8.5.8 Pressure Sensor	135
8.5.9 Deflection Due to Wind	136
8.5.10 Deflection Due to Sustained Acceleration	137
8.5.11 Deflection Due to Vibration	137
9. VEHICLE AND ENVIRONMENT	138
REFERENCES	141
APPENDIX	145
REFERENCES FOR APPENDIX	149

ILLUSTRATIONS

<u>Figure</u>		<u>Page</u>
1	Onboard measurement techniques	4
2	Free flight measurement techniques	6
3	Density measurement accuracy	11
4	Pressure measurement accuracy	11
5	Temperature measurement accuracy	12
6	Wind measurement accuracy	12
7	Rate of change of pressure and density	14
8	Rate of stagnation temperature change	15
9	Shock and boundary layers around the Saturn	21
10	Error in pressure ratio	23
11	Ultraviolet density gage location	33
12	Reflectance of platinum	39
13	Source configuration	41
14	Detector configuration	42
15	Ultraviolet air density gage schematic	44
16	Effect of number of photoelectrons	49
17	Number of photoelectrons	50
18	Accuracy of gage reading	50
19	Penetration of solar radiation into the atmosphere	58
20	Atmospheric transmission in x-ray and ultraviolet ionizing wavelengths when the sun is overhead	59
21	Photometer density gage electronics	70
22	Typical detector output	72
23	Signal input to FM oscillators	72
24	Instrument and solar tracking mounting	75
25	Detector and sun sensor assembly	76
26	Electron beam densitometer geometry	78
27	Penetration range of electron beam	80
28	Radius of electron beam	85

ILLUSTRATIONS (cont)

<u>Figure</u>		<u>Page</u>
29	Backscatter count rate	89
30	Configuration of a pitot-static tube	92
31	Acoustic meter mounting configuration	102
32	Fixed-cone wind gage flow angle notation	111
33	Angular deflection of light method of sensing diaphragm deflection using lateral photocell	115
34	Detail of light reflection geometry	117
35	Intensity variation of light method of sensing diaphragm deflection	121
36	Configuration of a pitot-static tube	124
37	Pressure profile around a cylinder in a normal flow field shown above	126
38	Pressure-peak shift caused by local winds	126
39	Crossover method for determining wind direction	128
40	Error caused by the mangus effect	128
41	Large launch vehicle configuration	139
42	Model launch vehicle performance data	140
<u>Table</u>		<u>Page</u>
I	Instrument Range	7
II	Composition of Atmosphere	56
III	Optical Scale Height and Number Density	60
IV	Wavelengths and Absorbing Species	61
V	Transmission of Various Materials in the Vacuum Ultraviolet	62
VI	Thickness of Aluminum Films for Which the Transmission is 0.5 Percent	63
VII	Extinction Coefficients of Filter Materials	63
VIII	Bandwidth Requirements	73
IX	Maximum Expected Angle of Shift of Pressure-Peak Caused by Wind	127
X	Boundary Layer Thickness (inches)	140

LIST OF SYMBOLS

α	angle of attack
A	amperes
β	impingement angle
γ	wind direction from true north
γ	ratio of specific heats
δ	direction of resultant wind (Fig. 38)
Δ	change between two measurements
τ	cone half angle (see Wind, Section 8)
σ	gage time constant
ρ	density
ξ	$\sin \theta / \sin \tau$ (Fig. 32)
φ	angle of roll (see Wind, Section 8)
λ	$\gamma - 1 / \gamma + 1$
Λ	molar heat of vaporization
γ	ratio of specific heats
ζ	boiling temperature of hypsometer fluid (Section 6.2)
K	constant of proportionality (Section 3.1.5)
ν	frequency of radiant energy
a	speed of sound
c	speed of light
C_p	surface pressure coefficient
d	distance to the volume being measured (Section 5)
D	diameter of collector
E	system response (Section 3.1.5)
F	a constant = $0.0341648^\circ\text{K/m}$ (Section 6.5)
g	acceleration of gravity
h	altitude
h	Planck's constant
H	scale height
I	intensity

LIST OF SYMBOLS (cont)

k	Boltzmann constant
L	distance between booms (Fig. 31)
\bar{M}	mean molecular weight
M	Mach number
p	local pressure
P	free air pressure
q	ambient specific humidity
Q	steady state response (Section 3.1.5)
R	universal gas constant
S	wind shear
t	time
T	ambient temperature
\bar{T}	mean ambient temperature of layer
U	most probable velocity of air inside pressure chamber
v	tangential velocity of cylinder (Section 8.2.4)
V	launch vehicle velocity
V	volume
w	instrument package vector velocity
W	wind vector
z	path length
Z	altitude

SUBSCRIPTS

0	at the reference altitude (usually sea level)
1	lower level
2	upper level
n	optical
∞	free, undisturbed atmosphere
s	shock layer
b	boundary layer

LIST OF SUBSCRIPTS (cont)

R	resultant
S	stagnation or total value
M	molecular-scale temperature
v	virtual temperature
ϵ	error in measurement or calculation (Section 6.5)
*	an erroneous value of the parameter (Section 6.5)

1. INTRODUCTION

The objective of this research is to seek out and evaluate methods of measuring several characteristics of the free atmosphere from on board a large launch vehicle. Characteristics to be determined are the density, pressure, temperature and wind of the undisturbed atmosphere above the altitude of 30 km. Typical large launch vehicles are Nova and Saturn.

The conclusions and recommendations are given in Section 2 of this Summary Report. Section 3 sets forth the requirements that measurement techniques and instruments must meet. A survey of present measurement methods is presented in Section 4. Sections 5, 6, 7, and 8 discuss, respectively, density, pressure, temperature, and wind measurement techniques. Launch vehicle and environmental parameters that were used during the research are detailed in Section 9.

2. CONCLUSIONS AND RECOMMENDATIONS

2.1 Conclusions

As a result of our research we have concluded that the most promising measurement technique is remote measurement. Here the instruments are located aboard the launch vehicle, but the actual measurement is made remotely in the undisturbed air outside the shock layer. This method avoids placing the instruments in the nose tip where they are lost when the escape rocket is jettisoned. However, the only property amenable to remote measurement is density. Consequently, we have formulated recommendations for immersion type measurements for the other properties. A promising alternative to onboard instrumentation is free flight or dropsonde techniques. We have formulated recommendations for these techniques also.

2.2 Recommendations for Onboard Instruments

Based on our study of large liquid-fueled launch vehicle requirements we make the following recommendations.

Density: either an ultraviolet-induced fluorescent or a differential solar absorption technique. In each case the instrument is located aboard the launch vehicle and the actual measurement is made in the undisturbed air outside the shock layer. (See Section 5).

Pressure: a pitot-static tube mounted on the launch vehicle tip. A cylindrical pitot tube is preferred because it is less sensitive to error due to angle of attack. However, a stagnation pressure port in the tip of a conical nose could be utilized if it is well calibrated for angle-of-attack effects. (See Section 6).

Temperature: a total temperature probe mounted on the launch vehicle nose. The total temperature is converted to the ambient value by computation using the measured pressure data and shock-expansion theory. (See Section 7).

Wind: monitor the differential dynamic pressure across a set of pitch and yaw ports located in a conical nose tip such as the F-16 Q-Ball. If an electro-optical data pickoff is used it should be possible to cover the entire altitude range with a minimum number of individual pressure gages. (See Section 8).

These recommendations are depicted schematically in Fig. 1.

Since the techniques and instruments recommended for density are novel, at least for use aboard a launch vehicle, we have discussed them in detail in Section 5. The ultraviolet density gage utilizes a physical principle that apparently has not been exploited heretofore, and which enables the gage to operate at altitudes that are unobtainable with other ultraviolet devices.

The density instruments would be particularly valuable, because if the air density (and composition) can be measured to great heights the pressure and temperature can be calculated from the density profile. There will be an increasing need for density and similar data at high altitudes as the manned space flight programs progress. Therefore, we strongly recommend that the development of one or both of the ultraviolet density gage and the absorption density gage discussed in Section 5 be undertaken at once.

2.3 Recommendations for Dropsonde Instruments

The only way to completely escape the perturbed environment of the launch vehicle and to guarantee a near-perfect isentropic flow-field is to employ dropsondes. The instruments are jettisoned at the proper altitudes and measurements made as they descend in free flight. The survey reported in Section 4 revealed that suitable instruments that have been extensively flight tested are available from current sounding rocket programs. Except for the ejection mechanism, no extensive development program is required.

The disadvantage of free flight techniques is that the test range is cluttered with data acquisition units, since each instrument

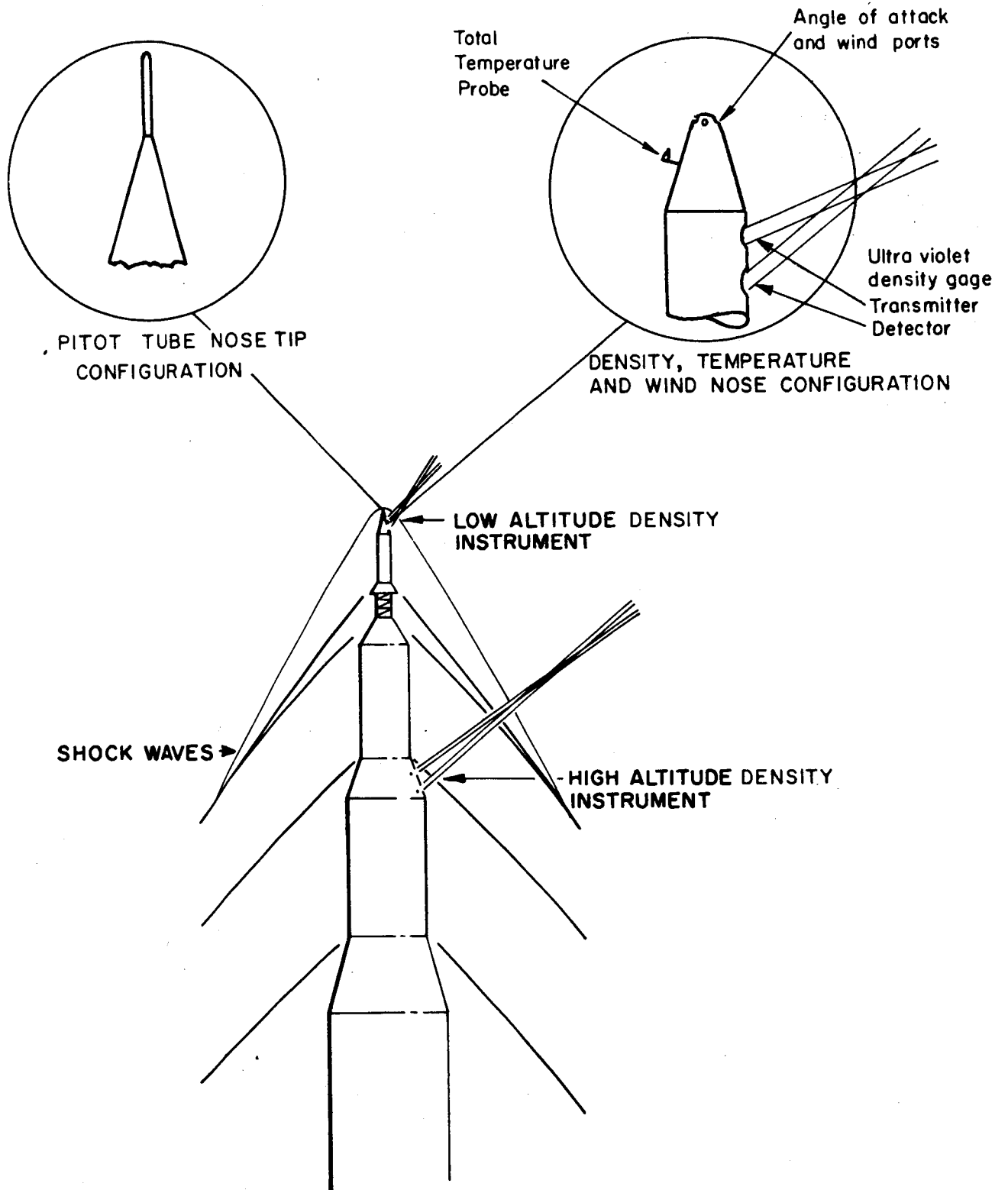


FIG. 1 ONBOARD MEASUREMENT TECHNIQUES

must be monitored separately. Also, the soundings are made down-range of the actual trajectory and only the upper portion of the sounding is made in the vicinity of the vehicle.

In order to determine the additional system requirements imposed by the use of separate free-flight instruments an analysis was made to select those measurement techniques which best fit the current situation. Our recommendations are portrayed in Fig. 2. A significant altitude for free flight techniques is 60 to 70 kilometers, because it is roughly the dividing line between the use of parachute-stabilized payloads and true free-fall payloads. Above 70 km there is insufficient dynamic pressure to open a parachute and cause it to stream in a reliable manner.

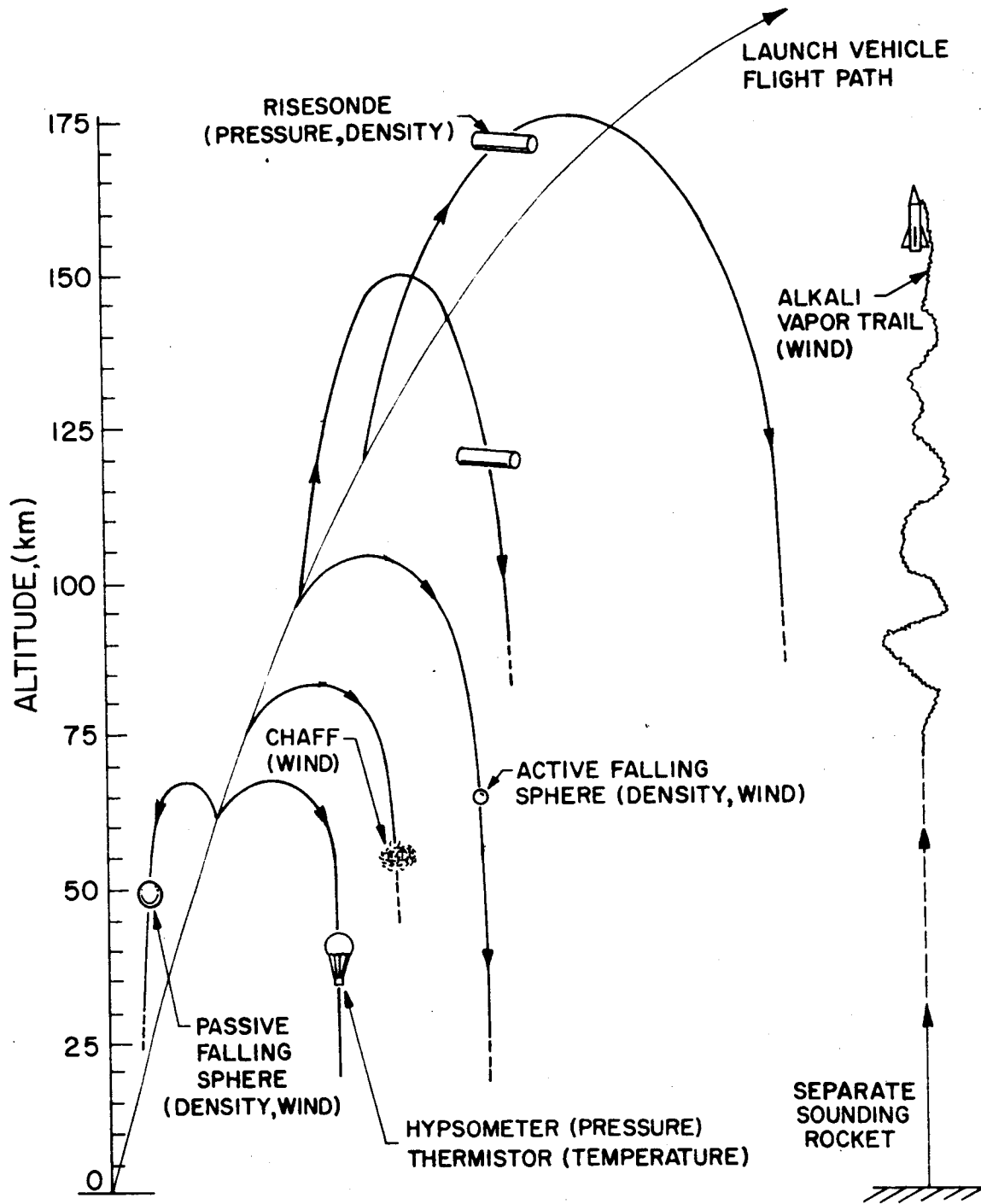
We visualize that these devices would be carried in an interstage compartment and jettisoned at appropriate intervals. A single parachute stabilized device could be dropped at 60 to 70 km for a single sounding somewhat remote from the actual launch vehicle flight path, or a number could be dropped in sequence to give data closer to the actual flight path of the vehicle. A similar procedure could be followed for the free fall devices above 70 km.

Density below 100 km can be measured by the falling sphere technique. Above 65 km an active type sphere is used and below 65 km a passive type is used. In the free molecule flow domain above 85 km a risesonde is recommended. (See Section 5.)

Pressure can be measured at parachute altitudes by a descent-type hypsometer. Above 85 km it can be measured by the risesonde. (See Section 6.)

Temperature below 70 km can be measured by a thermistor carried aboard a dropsonde. Above this altitude it must be calculated from a density profile. (See Section 7.)

Wind can be determined by tracking a parachute at low altitudes, chaff at medium altitudes, and a vapor trail at higher altitudes as is depicted in Fig. 2. (See Section 8.)



ALL INSTRUMENTS EJECTED CLEAR OF LAUNCH VEHICLE EXHAUST

FIG. 2 FREE FLIGHT MEASUREMENT TECHNIQUES

3. MEASUREMENT SYSTEM REQUIREMENTS

The requirements that must be met by the measurement system are imposed by good measurement practice and by the unique environment in which the measurements are to be made. The first part of this section discusses the requirements that must be met by the instruments. The second part concerns the requirements that must be met by the measurement technique in order that the measurement be truly representative of the free, undisturbed atmosphere.

3.1 Instrument Requirements

3.1.1 Range

For those instruments that measure the ambient or free atmosphere directly the dynamic range that is required is set by the altitude interval of concern, i.e., 30 to 100 km. The range of each property is set forth in the column of the following table labeled Ambient.

TABLE I

Instrument Range

<u>Property</u>	<u>Ambient</u>	<u>Stagnation</u>	<u>Reference</u>
Pressure (torr)	$10-10^{-4}$	$80-10^{-1}$	-1
Temperature ($^{\circ}$ K)	200-300	830-1500	-1
Density (kg/m^3)	$10^{-2}-10^{-7}$	$10^{-1}-10^{-5}$	-1
Wind speed (meters/sec)	50-300	-	-2
Wind shear (m/sec/m)	0.03-0.113	-	-2

The second column specifies the dynamic range that would be required of an instrument that measured the stagnation or

total value. The range of this property is dependent upon the vehicle speed, and the cited ranges are based on the representative trajectory for a large, liquid-fueled booster shown in Section 9.

Instruments that measure the ambient pressure or density must have a greater range than their stagnation counterparts. This is due to compression process in the stagnation instrument, caused by the increasing vehicle ascent speed, offsetting in part the natural decrease of the free air pressure and density with altitude. Temperature is an exception because the ambient temperature does not vary a great deal, while compressional heating greatly increases the stagnation temperature as the vehicle speed increases.

It is not implied that a single sensor can cover the six decades of pressure change or the five decades of density change. An instrument probably would have to contain multiple sensors or their equivalent in order to cover the required dynamic range.

3.1.2 Accuracy Requirements

A generally accepted goal in vacuum instrument design is that the error be 1 percent of the full scale reading. Of course, when the dynamic range of the gage is several decades, the error at the low end of the scale can be on the order of 100 percent of the actual reading. This design goal is due in part to the present lack of calibration facilities. In an article which reviewed measurement standards, Ref. 3, it is stated that the National Bureau of Standards can calibrate pressure instruments to one part in one (or 100 percent error) at a pressure of 10^{-4} torr, the pressure which corresponds to 100 km.

Since this study should remain general rather than specific, no attempt was made to establish specific accuracy requirements. We believe that a reasonable accuracy requirement is that the error be comparable to that obtainable with careful aeronomical soundings. To provide an indication of the magnitude of this error, the measurement error characteristic of several of the instruments tabulated in Section 4 is represented in pictorial form in the following figures.

Figure 3 depicts the error of representative current density techniques. Error estimates are available for the passive Robin-type falling sphere which is useful below 65 km, but not for the active type that can be used to above 100 km. Density from a pitot-tube system is a calculated density. References from which these data are taken are given in Section 4.

Figure 4 depicts the error of current pressure measurement systems. The hypsometer curve is a composite of a balloon-borne type up to 70 km and a dropsonde type above. Based on present aeronomical techniques the accuracy requirement of pressure-measuring instruments is about 2 percent of full scale reading up to 50 km increasing to 5 percent above this.

Temperature accuracy runs from about 2 percent at 30 km to 5 percent above 75 km according to Fig. 5. Above dropsonde altitude the temperature is calculated from density measurements or obtained by the rocket grenade technique.

It is claimed that with precise tracking of an Arcas parachute it is possible to measure the wind speed to within 2 to 3 meters per second up to 60 km (Ref. Fig. 6). The currently operational Meteorological Rocket Network is able to achieve only 7 mps. Above 50 km an accuracy of 10 mps appears to be a reasonable requirement.

The following wind gage performance goals have been developed by the Experimental Aerodynamics Branch, Aeroballistics Division for use internal to GMSFC. These performance goals are applicable to the Saturn and are cited here as being typical of those for large liquid launch vehicles in general. Because wind instrument requirements appear to be intimately related to the dynamics of the particular vehicle, no detailed requirements will be specified in this report.

Wind

<u>Altitude</u> (km)	<u>Velocity Range</u>		<u>Gust Accuracy</u> (m/sec)	<u>Vector Accuracy</u> (percent)
	<u>Required</u> (m/sec)	<u>Desired</u> (m/sec)		
0-30	0-75	0-97	±9	5 rms
30-100	0-140	0-180	±9	10 rms

3.1.3 Resolution

The resolution requirement for pressure and density gages is set by the low end point of the reading. For example if a pressure gage is to be used to 100 km altitude it must have a low end point of 10^{-4} torr. The resolution then must be at least 10^{-4} torr. Temperature should be resolved within 1 degree.

3.1.4 Frequency

It is customary to specify gage requirements in terms of a frequency; for example, 20 cps. This type of specification would be artificial in the present situation because most of the quantities being measured vary relatively slowly and uniformly with time. An exception is wind, the frequency response of which is intimately related to the dynamics of the particular vehicle. Because of the uniqueness of the wind frequency requirement, no general specification will be made for wind.

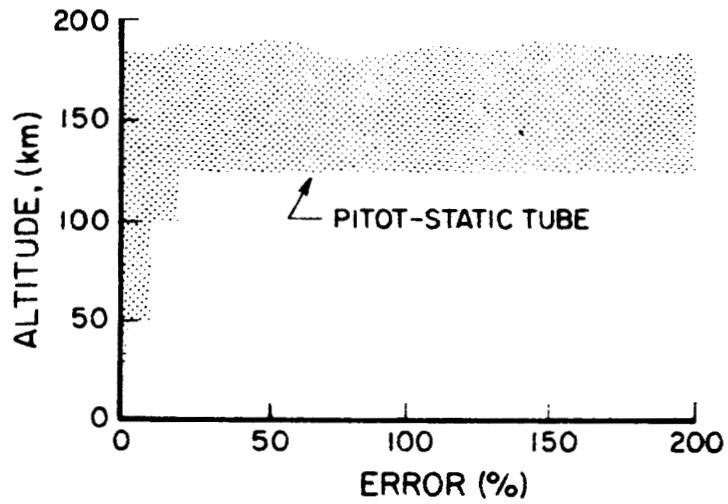
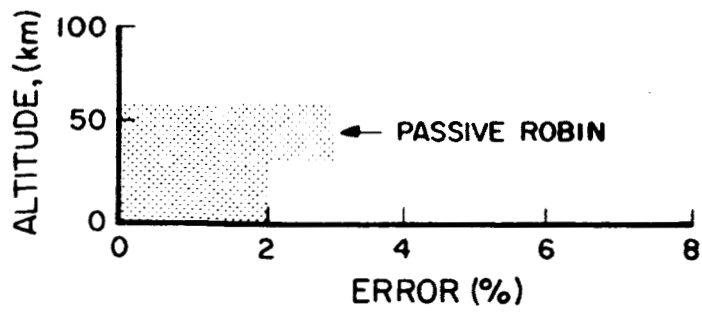


FIG. 3 DENSITY MEASUREMENT ACCURACY

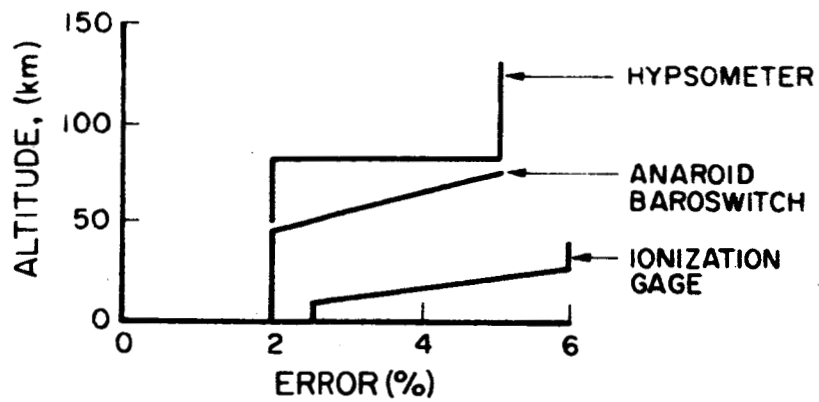


FIG. 4 PRESSURE MEASUREMENT ACCURACY

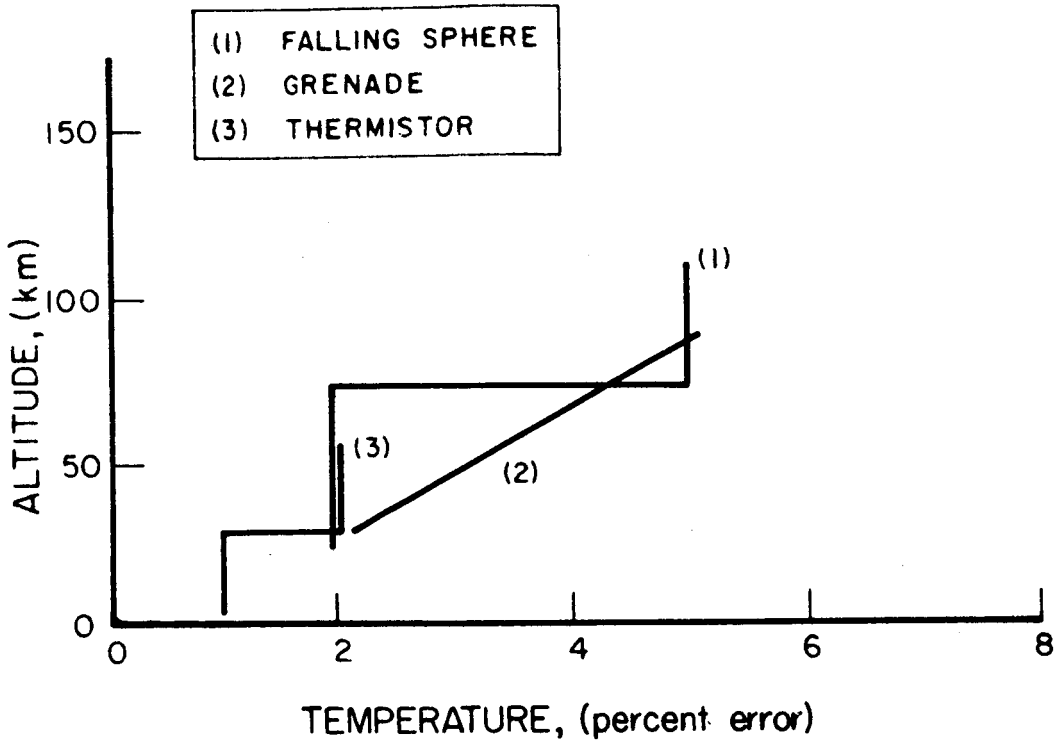


FIG. 5 TEMPERATURE MEASUREMENT ACCURACY

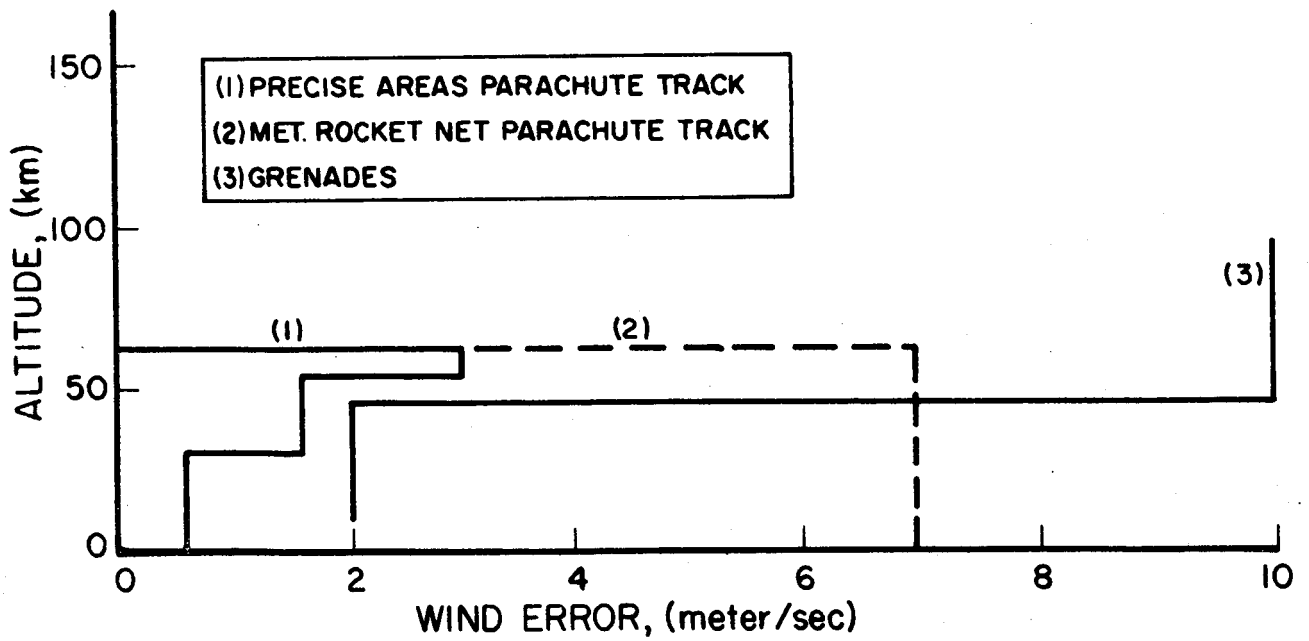


FIG. 6 WIND MEASUREMENT ACCURACY

This low rate of change is illustrated in Figs. 7 and 8. These figures show the rates of change of the free air and stagnation pressure, density and temperature that would be seen by a rocket, ascending vertically, at various speeds. The speed-altitude curve, which is typical of a large, liquid launch vehicle, has been superimposed on the stagnation charts. It is seen that the maximum rate of change of stagnation pressure is only slightly greater than that of free-air pressure. However, a stagnation temperature instrument aboard a typical launch vehicle would have to follow a rate of change which is about seven times greater than for a free-air temperature instrument.

For all cases the rates of change are relatively low. In view of this, we believe that the concept of time-constant is a more useful parameter for a discussion of the dynamic performance of the pressure, density and temperature instruments.

3.1.5 Time Constant

The time constant requirements for pressure, density and temperature were established by studying the error that would be caused by a given instrument lag. To establish an upper limit on time constant a value of 1 second was assumed and the reading error calculated. The error incurred with this large time constant was not excessive. Thus, it appears that a time constant of $\frac{1}{4}$ to $\frac{1}{2}$ second would be entirely adequate.

Most sensing systems exhibit a simple, one-time constant behavior, so that they can be represented by an equivalent mechanical system having only a spring and dashpot or an electrical system having only capacity and resistance.

The equation for this system is

$$RI + \frac{Q}{C} = E \quad (1)$$

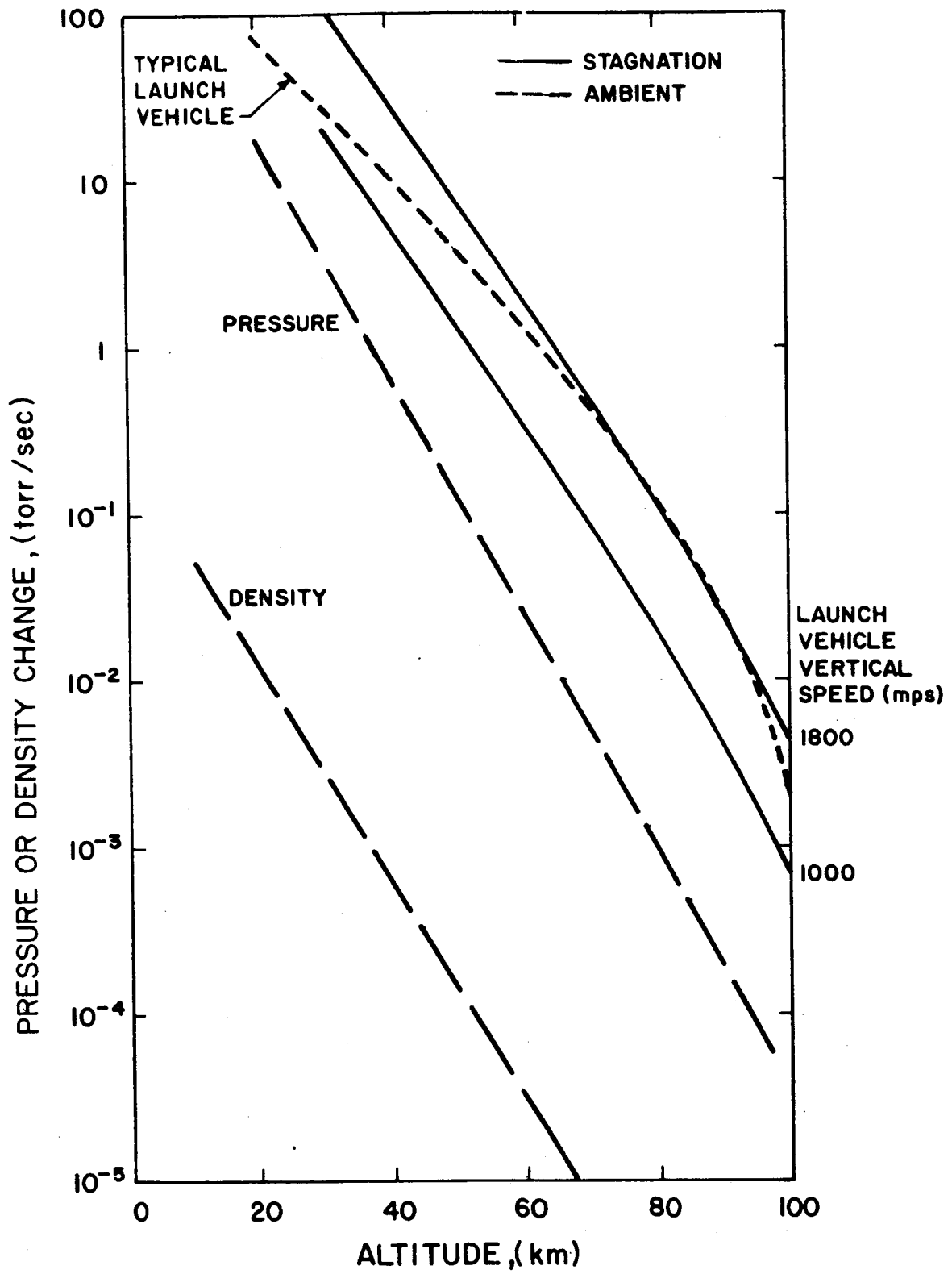


FIG. 7 RATE OF CHANGE OF PRESSURE AND DENSITY

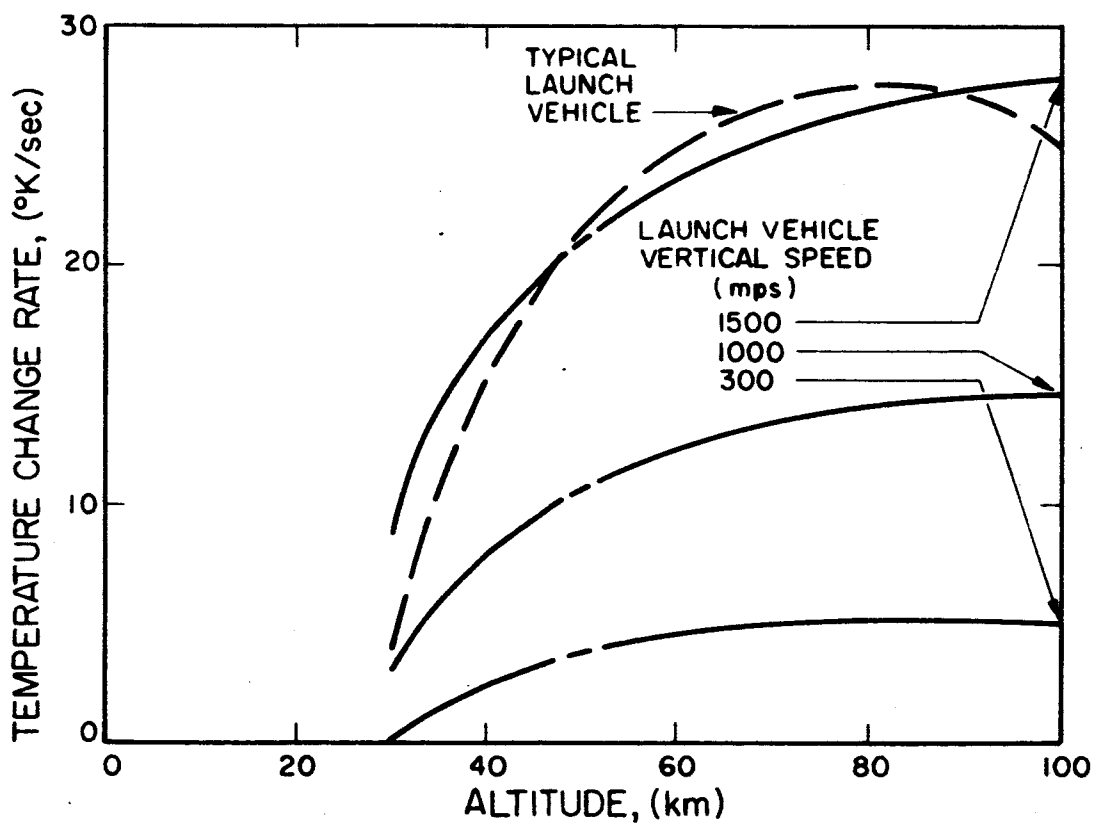


FIG. 8 RATE OF STAGNATION TEMPERATURE CHANGE

The variable of interest is Q, not I, because I will vanish if E is constant. Therefore, if I represented the system response, there would be no output for a steady stimulus, as for example, an unvarying temperature. Q, on the other hand, will be a constant if E is a constant, and is, thus, the proper choice to represent system response. Equation 1 is then written

$$R \frac{dQ}{dt} + \frac{Q}{C} = E \quad (2)$$

If the instrument is a densitometer, for example, then E would be represented by

$$E = \kappa\rho = \kappa\rho_0 e^{-h/H} \quad (3)$$

Also, assuming constant vertical velocity, V,

$$h = Vt \quad (4)$$

Substituting Equations (3) and (4) in (2)

$$Q = \frac{Q_0}{1 - \sigma \frac{V}{H}} \left[e^{\frac{-Vt}{H}} - \sigma \frac{V}{H} e^{-\frac{t}{\sigma}} \right] \quad (5)$$

In this equation, σ is the system time-constant $\sigma = RC$, Q_0 is the steady-state response up to time zero, and Q is the response thereafter. The denominator, $1 - \sigma \frac{V}{H}$, is independent of time and can be regarded as a gain or scale factor. The first exponential is the desired response, and the second exponential represents the disturbing effect of the system time-constant.

If one assumes a vertical velocity of 1 kilometer per second, a scale height of 7 km, and a time constant of 1 second

(a time-constant much greater than any suitable instrument is likely to have) the percentage of error in Q as a function of time will be as given in the following table.

<u>Time (sec)</u>	<u>Error (percent of reading)</u>
0	0
1	5.9
2	2.6
3	1.07
4	0.46

It is clear, therefore, that even with the unrealistically long time-constant of 1 second the error would be unimportant after a few seconds. Thus, a time constant of less than 1 second would be adequate. This analysis would apply equally well to a pressure instrument, which also obeys Eq. 3.

Atmospheric temperature does not follow Eq. 3, which therefore cannot be used as the force function in Eq. 2. The stagnation temperature vs. time curve can be fitted with the parabolic approximation

$$T = a + bt^2 \quad (6)$$

Using this as the force function in Eq. 2 the solution is;

$$Q = A \left[T + 2b^2\sigma \left(1 - e^{-t/\sigma} \right) \right] - 2b\sigma t \quad (7)$$

where T is the true stagnation temperature. Assuming $\sigma = 1$ sec, time zero to be at an altitude of 8 km, $a = 300$ and $b = 0.27$, the error history will be as follows:

<u>Time (sec)</u>	<u>Altitude (km)</u>	<u>Stagnation Temperature (°K)</u>	<u>Error (% of reading)</u>
10	11	312	-1.6
30	22	533	-2.8
50	39	1022	-2.5
70	64	1620	-2.2

The calculation was not carried beyond 70 seconds because the stagnation temperature subsequently decreases. This will cause the error due to instrument lag to decrease. We believe that these calculations verify our contention that a time-constant of 1/4 to 1/2 second would be adequate.

3.1.6 Vibration and Shock

All instrumentation that is carried by a launch vehicle typically must be capable of operation in a vibration environment of 20 to 2000 cps and 7.5 to 12.0 g rms. A typical shock specification is 40 g rms for a duration of 6 to 11 msec. Since this frequency is well above that of any of the atmospheric parameters (see Section 3.1.4), it should be possible to distinguish the slowly varying atmospheric parameter signal from the rapidly varying vibration-induced noise.

3.1.7 Sustained Acceleration

Instrumentation that is carried aboard a large, liquid launch vehicle will be subjected to a transverse acceleration which will increase from about 0.1 g at 30 km, to about 4 g at first stage burnout. Depending upon the particular vehicle, the first stage will burn out between 60 and 80 km. Lateral acceleration due to the turning of the vehicle along the flight path will impose negligible acceleration on the instruments. A typical test specification is 20 g for at least 1 minute.

Instrumentation that is carried aboard a solid propellant sounding rocket must be capable of withstanding an acceleration of about 26 g. It has been reported that an acceleration of around 60 g is imposed on instrumentation during jettisoning of a dropsonde. Therefore, the acceleration environment will impose no unusually severe requirements on the instrumentation.

3.1.8 Temperature

It is a requirement that all instrumentation be capable of operation at an elevated temperature and not subject to significant temperature error due to a zero shift, sensitivity shift, etc. At this time it is not possible to specify the heat input to the instruments

because it is dependent upon the configuration and location aboard the launch vehicle. An instrument located at a stagnation point probably would reach a peak temperature of about 85 percent of the peak air temperature, or around 1300°K. The minimum temperature would be influenced by the proximity of the cryogenic fuel tanks. A typical test condition is a temperature range of $\pm 85^{\circ}\text{C}$.

3.1.9 Size and Weight

Since the instrumentation is to be used aboard large launch vehicles, size and weight are not as critical as with sounding rockets. No size requirement will be stated, except that the instrument should be as compact as possible and should not weigh over a few pounds.

3.1.10 Power Consumption

The power source for onboard measurement systems should be the launch vehicle's primary power source. The maximum power requirement should be 28 volts dc at 200 ma.

3.1.11 Output

Instrument output may be either a continuous function of the measure and in the form of a current or voltage amplitude, change of frequency, or a variation of resistance. There are no unusual requirements imposed on the measurement system other than that its output must be compatible with the vehicle telemetry.

3.2 Measurement Technique Requirements

Our calculations have established that it is a requirement that the measurement be made directly in the ambient air if measurements of the highest accuracy are desired. If this is impracticable the instrument must be located on the nose tip. It is impossible to make accurate free-air measurements with instruments located aft on the vehicle unless they are the remote-reading type and have a very large penetration distance.

Figure 9 illustrates the complicated, nonisentropic flow field around a Saturn at Mach 1.93, and probably is typical of the flow field around any large, liquid launch vehicle. The sketch was taken from a wind tunnel photograph and was supplied to us by the NASA Contract Technical Monitor. If a total pressure probe were placed on the nose tip the flow field would be relatively simple and steady, and the shock angle at the probe intake orifice would remain 90 degrees. However, if the probe were placed in the flow aft of the nose tip the flow field would be less certain. Assuming that the flow field shown in Fig. 9 is representative, the large number of detached, curved shock waves in the flow aft of the nose stations would make hopeless the task of analytically following a streamtube upstream to the point where it entered the bow shock.

Ideally, a measurement of the environment should be made out in the undisturbed free air. This way there is no error due to the conversion from the measured local stream to the free-stream values. To determine how far away from the launch vehicle a measurement would have to be made in order to get beyond the shock layer, an estimate was made of the shock layer thickness from Fig. 9. It was found to be about 2 body diameters. Thus, unless the measurements were made near the nose tip, the measurement technique must be able to reach a distance from 8 to 15 meters from the launch vehicle.

The characteristics of the local-flow field within the shock layer then were studied to establish the range necessary to get beyond the boundary layer. Wind tunnel tests have indicated that for a vehicle like the Saturn the boundary layer is turbulent and has a thickness of about 8 cm at forward stations and as much as 35 cm at aft stations. In addition, such thick boundary layers are prone to separate. Thus, in order to reach beyond the boundary layer an ideal instrument mounted anywhere but on the nose tip must have a range of at least 8 centimeters.

FREE STREAM CONDITIONS:
MACH NO.: 1.93
REYNOLDS NO.: 6.90×10^6 /ft
ANGLE OF ATTACK: 0 DEG.

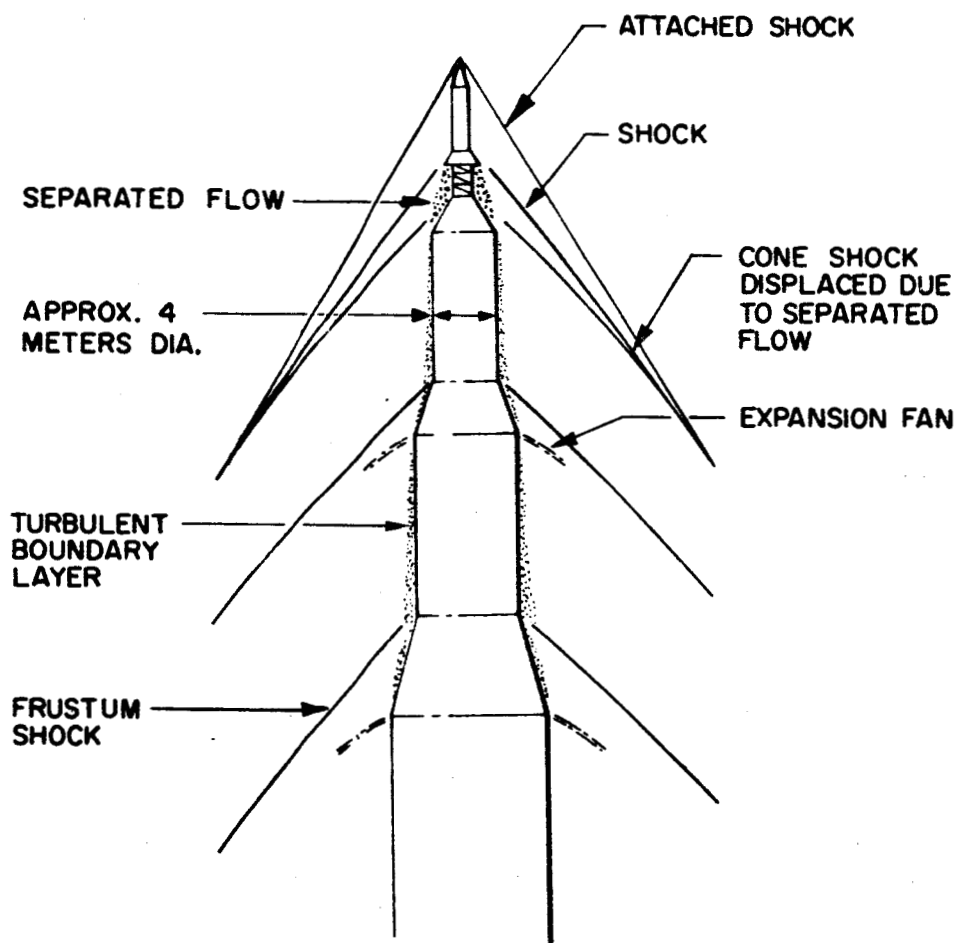


FIG. 9 SHOCK AND BOUNDARY LAYERS AROUND THE SATURN

The importance of careful selection of the position within the shock layer flow at which the measurement is to be made was investigated next. The conversion of a measurement made in the local-flow into its corresponding value in the free air requires an estimate of the Mach number and the angle of the upstream shockwave(s) through which the streamtube being investigated has passed. Using cone theory it was found that an error in overestimating the shock wave angle by as little as 5 percent will cause, grossly, a positive error of about 10 percent in the conversion of local pressure to free air pressure and a 2.5 to 3.5 percent error in upstream Mach number. The error is the ratio of cone surface pressure to free stream stagnation pressure and is depicted in Fig. 10. As this figure shows, a 10-percent underestimate in shock wave angle will result in a negative error of about 17 percent error in free air pressure.

The conclusion to be drawn here is that it is vital that measurements be made in as well-defined and simple a flow field as possible. A highly precise measurement of the local flow would be of little value if a 10- to 17-percent error is incurred in converting it into the corresponding value in the free air. This conclusion lead us to concentrate our initial effort, not on instruments and sensors, but on remote-field measurement techniques that can measure the desired atmospheric characteristics.

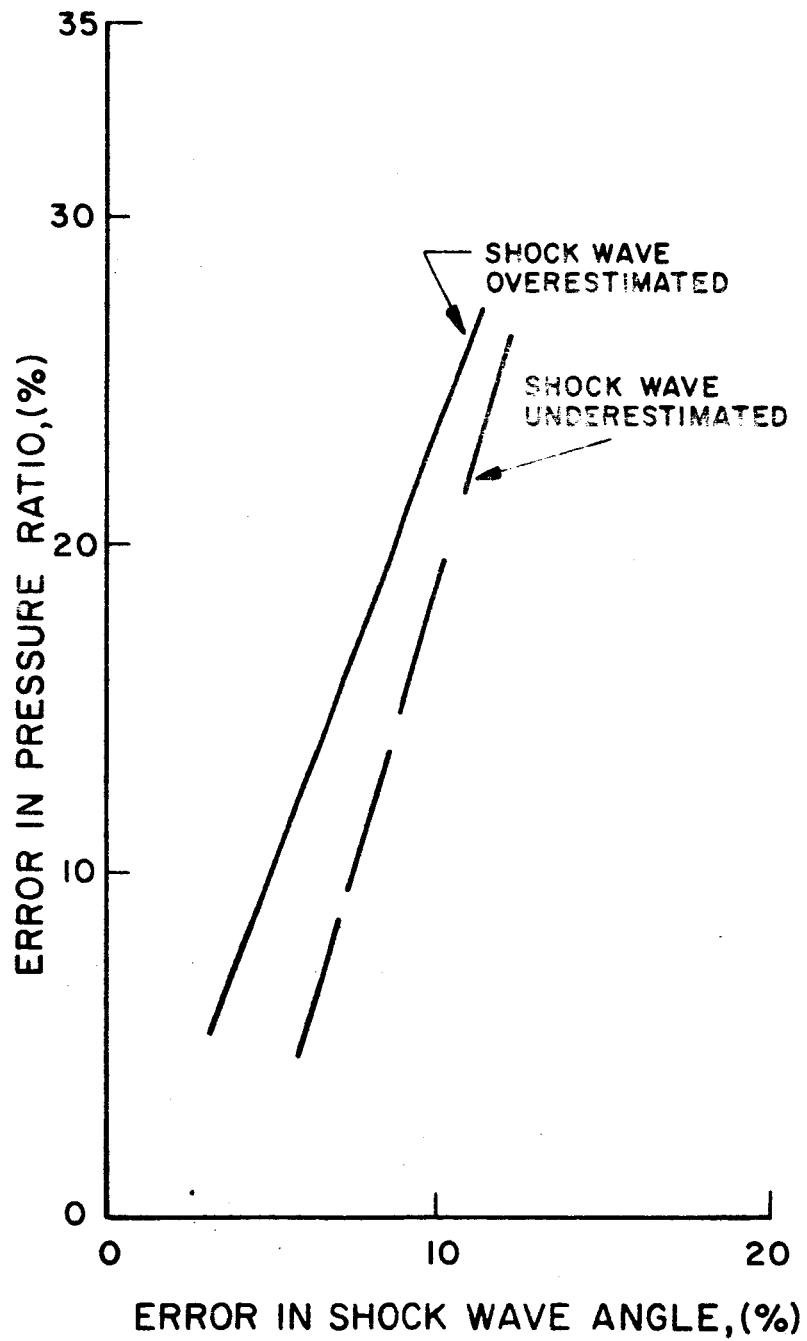


FIG. 10 ERROR IN PRESSURE RATIO

4. PRESENT SYSTEMS

One of the first tasks was to survey presently used methods to measure density, pressure, temperature, and wind. Each of these methods was to be evaluated for application to the present case. To provide a ready reference we summarized our findings in tables which make up the balance of this section. There are separate tables for each of the four atmospheric properties.

In many instances measurement techniques and instrumentation are recommended in other sections of this report without much detail on how they function. This is done because they are common aeronautical items and are extensively written up in the literature. It is deemed necessary to repeat this material here. Several excellent summaries of aeronautical instrumentation and techniques have been written. They are listed in Refs. 4 through 13.

SPACE INSTRUMENTS

PRESSURE TRANSDUCERS

Instrument	Principle of Operation	Error	Range (torr)	Altitude (km)	Remarks	Reference No.
Aneroid barometer	Elastic diaphragm	1.5 torr 3 torr	3.75-760	<15 <25	Subject to mechanical linkage friction and back lash. Ceiling is 25 km	15
Strain gage	Crystal deformity		$10^1 - 10^{-6}$ mm (modified type) 0-35000 PSI	150		21
Hypsometer	Temp. change of boiling liquid	2-5% 5%		46 69	Ascent type sensitivity increases with increase in altitude. Descent type requires excessive power to boil liquid for equilibrium	4,6
Bourdon tube gage	Tube distortion	0.5% full range		30	Subject to mechanical linkage friction, hysteresis of tube	3
Quartz Bourdon tube	Tube distortion	1%		61	Uses variable capacitance pickoff; has low temp. coef.	3
Thermionic ionization gage	Ionization caused by electrons from hot filaments; ion current varies with pressure		$10^{-5} - 10^{-9}$	135-620	See Alphanatron remarks	
Radioactive ionization gage, (Alphanatron)	Radioactive source ionizes particles	2% lower altitudes $\pm 5\%$ at 110 km, more at higher alt.	10^{-5}	<120	Measures relative no. of ions formed; composition dependent; temperature dependent; external ion source dependent (radiation hazard, Alphanatron only)	4,6,11, 13,16

SPACE INSTRUMENTS (continued)

PRESSURE TRANSDUCERS

Instrument	Principle of Operation	Error	Range (torr)	Altitude (km)	Remarks	Reference No.
Bayard-Alpert ionization gage	Inverted hot cathode ionization gage, ionization caused by electrons colliding with molecules		10^{-2} - 10^{-9}	70-620	See Alphatron remarks	6
Cold cathode inverted magnetron ionization gage	Ionization caused by electrons emitted from cold cathode and moving in crossed electric and magnetic fields		$>10^{-13}$	<2000	See Alphatron remarks	16
Phillips gage	Ionization caused by electrons emitted from a cold cathode		10^{-1} - 10^{-7}	70-380	Cold cathode with active emitter	4,16,21
Pirani gage	Thermal conductivity		10^{-1} - 10^{-3}	65-80	Temperature dependent	16
Havens gage	Pirani gage pumped with mechanical bellows		$>10^{-5}$	<135	Long response time	11
Hastings altimeter	Compensated hot thermopile thermococonductivity (modified Pirani gage)		10 - 10^{-3}	20-95		11

SPACE INSTRUMENTS (continued)

PRESSURE TRANSDUCERS

Instrument	Principle of Operation	Error	Range (torr)	Altitude (km)	Remarks	Reference No.
Pitot-static tube		5-15%		30-120	Diaphragm manometers and ionization gages used for sensors	23,26
Thermocouple gage		20-50%		110-150	Signal output level very low	22
Mass spectrometer	RF, dc fields and quadrupole mass filter (Massen filter) Linear mass spectrum is obtained from a linear voltage sweep measures partial pressures			>200	Requires no magnetic field; construction is simple and rugged. Initial conditions affect only percentage transmission and resolution.	17
Calculation	From measured temperature profile	2-5%		60	Used by Navy HASP	6

UPPER ATMOSPHERIC INSTRUMENTS AND TECHNIQUES

DENSITY TRANSDUCERS

Instrument	Principle of Operation	Accuracy (%)	Altitude (km)	Remarks	Reference No.
Falling Sphere	Radar track or accelerometer	Passive: 3 Active: 5-7	30-61 100	Wind dependent; passive requires precision radar and large computer; active is expensive	6,16,26 27,28
Glow discharge at rocket surface	Paschen's law relating density to breakdown voltage and geometry	5	<80	Measures local air density behind shock wave; require 0.1% stability in power supply	4,18
Glow discharge in ambient air	Voltage breakdown caused by focused microwaves of varying amplitude and frequency ahead of rocket			Measures ambient density	18
Pitot-static tube	Calculated from stagnation pressure and Rayleigh pitot formula for diatomic gas	2-10 20-200	20-110 110-300	Diaphragm manometers and ionization manometers used as sensors	14,20
Pressure modulation on rolling rocket	Modulation proportional to density		30-220	Wind, yaw and outgassing are sources of possible error	22
Pressure on nose cone of rocket	Taylor-Maccoll theory, density is calculated quantity		30-120	Wind, yaw and outgassing are possible sources of error	22
Pressure on side of rocket	Ambient pressure ring exists on flying rocket. Pressure primary, density and temperature calculated		30-120	Wind, yaw and outgassing are possible sources of error	22
X-ray absorption	Variation of X-ray intensity with altitude	30 50	75 150	Uses sun as reference and requires instrument to point towards the sun	6,25
α or β backscatter	Number of particles which are reflected back to downstream collector				
Induced fluorescence	Ultraviolet or electron beam induces fluorescence in air			Amount fluorescence is measure of density	

SPACE INSTRUMENTS

TEMPERATURE TRANSDUCERS

Instrument	Principle of Operation	Accuracy (\pm °C)	Range (°C)	Altitude (km)	Remarks	Reference No.
Thermistor	Resistance varies with temperature	2-3 5-6	3 decades	to 30 to 45 to 60	Time constant limits use to below 60 km. Use 10 mil head above 25 km	6,15 16,28
Thermocouple	Seebeck effect	20	2 decades	to 75	Signal out is small	18,26
Rocket-grenade	Velocity of sound is dependent on wind and temperature	5 10		to 30 to 90	Wind is also derived from data. Gas constants become uncertain at high altitude	5,14
Conical pitot-static tube	Taylor-Maccoll and Stone theories of aerodynamic flow around right circular cones at >Mach 1	5 7		50 >50	Temperature calculated from shock expansion theory	5,14
Shock wave angle pressure	Angle of shock wave is dependent on temp., velocity (Taylor-Maccoll Theory)				Must know velocity of vehicle	15
Ceramic rod	Element is a lead carbonate pigment	1	-90 to +60	<30		15
Bimetallic	Thermal expansion coefficient	2	-80 to +60	<30	Time constant limits use to less than 30 km	15
Sonic thermometer	Sound speed in air			100	Laboratory use only, so far. Transducers heat air	5
Falling sphere	Calculated from density profile	2% 30% 5%		25-70 70-75 >75	See density sheet	7,10
Pressure gage	Calculated from pressure profile	25 15 20 40		50-60 65-75 72.5 >100	Russian report	10
Resistance thermometer	Resistance varies with temperature	10 20		50 75		5

SPACE INSTRUMENTS

WIND INSTRUMENTS

Instrument	Principle of Operation	Accuracy (mps)	Range	Altitude (km)	Remarks	Reference No.
Balloon	Radar track	7		<35		6
Parachute	Radar track	4-7		31-61		5,7,26
Sphere	Radar track	1-10		31-61	FPS-16 radar req'd	5,7,26
Exhaust trail	Drift	1		80-200		5,7,26
Meteor trail	Drift	1		80-110		5,7,26
Alkali vapor	Drift	1		80-210		5,7,8,10,26
Chaff	Drift	1		45-80	Limited to over 50 km	5,7,8,10,26
Grenade	Speed of sound is dependent on wind and temperature	2		35	Temp. is also determined ±18° in azimuth	5,11,14
Static pressure probe	Spin pressure modulation	10		90		23
Windvane	Airflow over a cone surface			80		24
Conical pitot-static tube	Pressure pattern on cone surface				Currently used for angle of attack	29,30

5. DENSITY

Atmospheric density is the one property that is very amenable to remote measurement. A "remote measurement" is the case where the instrument is located on board the launch vehicle but the actual measurement takes place at a point remote from the vehicle. As pointed out in Section 3.2, if the instruments are to be mounted anywhere but on the nose tip they must be of the remote measuring type to avoid the errors inherent in measurements made within the shock layer. Each of the remote techniques that was uncovered during the preparation of Section 4 was analyzed to determine if it met the system requirements. Novel methods suggested by the EOS staff also were investigated. The more promising density instruments and our findings concerning them are discussed in this section.

Two devices which showed exceptional promise and which are recommended for development are discussed in Sections 5.1 and 5.2. These are the ultraviolet air density gage and the solar absorption air density gage. One technique to measure the local density with on-board instrumentation is discussed in Section 5.4.

5.1 Ultraviolet Air Density Gage

A technique that utilizes the rearrangement radiation from molecular nitrogen shows great promise for the remote measurement of density. The method of detection would be to excite the air to visible fluorescence by shining a beam of ultraviolet light through it. The intensity of the fluorescence as a function of the amount of energy fed into the ultraviolet source would be a measure of air density. The instrument would consist of a collimated, excitation ultraviolet source and a photomultiplier tube detector with focused optics. Figure 11 shows where the devices would be located aboard a launch vehicle.

This technique is capable of measuring atmospheric densities from 5×10^{-8} gm/cm³ (80 km) to 10^{-14} gm/cm³ (350 km) at a distance up to 3 meters from the vehicle carrying the device. It detects the fluorescence of molecular nitrogen when bombarded by 500 Å to 700 Å photons. A sequence of filters and source modulators is utilized to make certain that only gas molecules can contribute to the signal, and not reflections from dust particles or ice crystals.

This latter characteristic is important because other ultraviolet densitometers rely on absorption and reradiation. Both the bombarding light and the returned signal are of the same wavelength. Thus, the presence of dust, ice, or particles from entrained exhaust could cause a large error due to reflection from their surface. Accurate measurements in the region of nacreous and noctilucent clouds might be very difficult. An illustration of this difficulty was a recent attempt to calibrate an absorption-reradiation type ultraviolet density gage in a vacuum chamber. The dust in the chamber caused the instrument to read no higher than 25,000 feet altitude, although the chamber density actually was nearer 40,000 feet.

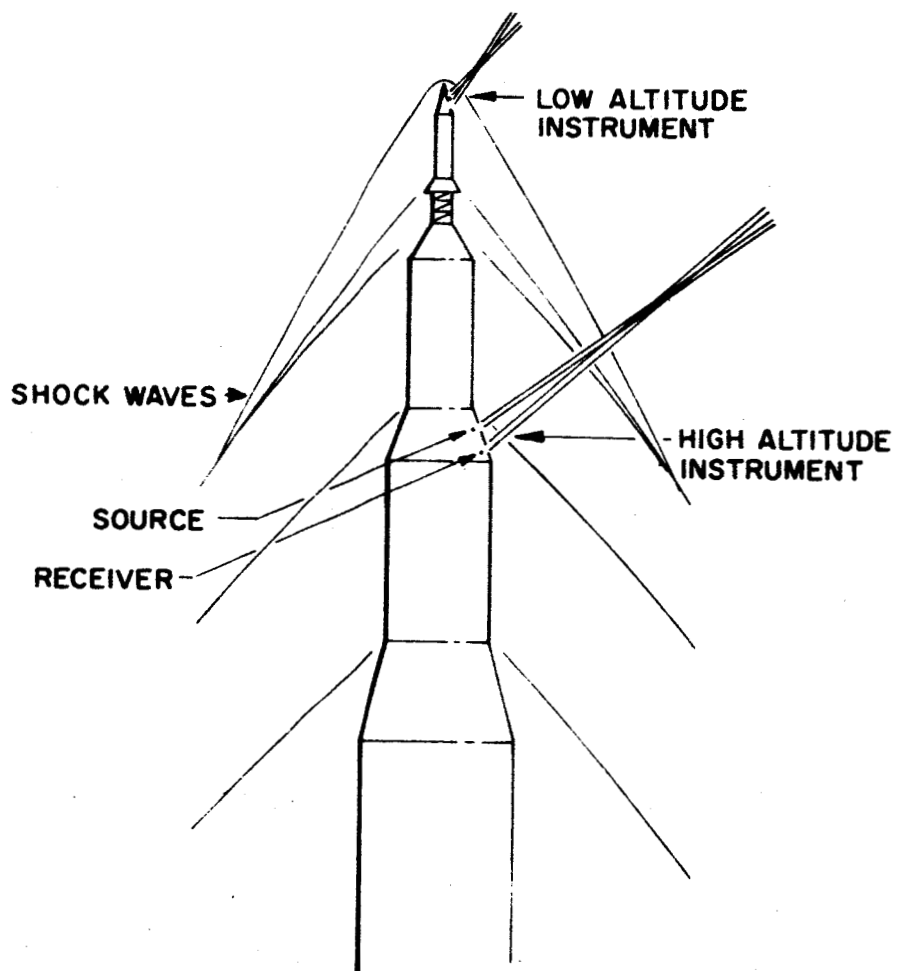


FIG. 11 ULTRAVIOLET DENSITY GAGE LOCATION

We believe that the rearrangement radiation type ultraviolet gage also will provide accurate density measurements in regions where the absorption-reradiation type cannot because of lack of returned signal. The EOS technique enables measurements to be made at a frequency where the most probable cross section is from 100 to 1000 times greater than at other practical frequencies. Thus, the return signal is orders of magnitude greater and the operational ceiling correspondingly greater. Moreover, the return signal is in the visible and very-near ultraviolet portion of the spectrum where a photomultiplier (P-M) tube detector is the most sensitive. In general, a P-M tube is ten times more efficient with visible light than with ultraviolet. In addition, if a P-M tube is used in the ultraviolet, a sodium silicate coating is required over the P-M tube window to convert the incident ultraviolet photons to visible photons. With the EOS technique this coating is not necessary and the efficiency of the P-M tube is enhanced.

5.1.1 Theory

The absorption length where the intensity has dropped to $1/e$ of its initial intensity is given by

$$L = \frac{A}{N_0 \sigma} \quad (8)$$

where A is the molecular weight of the gas, N_0 is the Avogadro number, and σ is the cross section for nitrogen. Evaluating Eq. 8 we find

$$L = \frac{28}{6 \times 10^{23} \times 2 \times 10^{-17}} = 2.33 \times 10^{-6} \text{ gm/cm}^2 \quad (9)$$

To find the physical path length l , we take

$$l = \frac{L}{\rho} \quad (10)$$

Evaluating Eq. 10 at an altitude of 95 km we find that the physical path length is 2.33×10^3 cm.

The intensity of fluorescence at a given distance x is then

$$I = I_0 \exp \left[\frac{-x_1}{2.33 \times 10^3} \right] \quad (11)$$

where x_1 is given in centimeters. The change in intensity between x_1 and x_2 is:

$$\Delta I = I_0 \left[\exp(x_2/2.33 \times 10^3) - \exp(x_1/2.33 \times 10^3) \right] \quad (12)$$

If $x \ll l$ then, a first approximation:

$$\Delta I = I_0 (x_2 - x_1)/2.33 \times 10^3 \quad (13)$$

The change in intensity, ΔI , is the amount of the initial radiation that is absorbed between x_1 and x_2 . $\Delta I/I_0$ is then the fraction of the initial energy between 500 Å and 700 Å that is absorbed between x_1 and x_2 .

Five percent of the energy absorbed between x_1 and x_2 is reradiated in the visible, thus

$$E_v = 0.05 E_0 \frac{\Delta I}{I_0} \quad (14)$$

where E_0 is the initial energy available between 500 Å and 700 Å. The reradiated energy is reradiated isotropically. The fraction of the reradiated energy E_v seen by a detector of area A and at a distance R from the radiating element is

$$f = \frac{A}{4\pi R^2} \quad (15)$$

For $A = 1.5 \text{ cm}^2$ and $R = 300 \text{ cm}$, $f = 1.3 \times 10^{-6}$. The total energy received at the detector E_R is thus given by

$$E_R = 0.05 f E_0 \frac{\Delta I}{I_0} \text{ or}$$

$$E_R = 0.05 f E_0 \left[\frac{x_2 - x_1}{2.33 \times 10^3} \right]$$

For $E_0 = 0.1 \text{ joules}$ and $x_2 - x_1 = 100 \text{ cm}$, the energy received at the detector is

$$E_R = 2.8 \times 10^{-10} \text{ joules} = 2.8 \times 10^{-3} \text{ ergs} \quad (16)$$

The number of photons incident on the detector can be calculated by first finding the average energy \bar{e} of the received photons.

$$\bar{e} = \frac{hc}{\lambda} \quad (17)$$

h is Planck's constant = 6.6×10^{-27} erg-seconds; $c = 3 \times 10^{10}$ cm/sec;
and λ , the average wavelength, is in cm.

Choosing $\lambda = 4000 \text{ \AA} = 4 \times 10^{-5}$ cm

$$\bar{e} = 5 \times 10^{-12} \text{ ergs/photon} \quad (18)$$

The average number of photons incident on the detector area A is then

$$\bar{N} = \frac{E_R}{\bar{e}} = \frac{2.8 \times 10^{-3}}{5 \times 10^{-12}} = 6.5 \times 10^8$$

5.1.2 Received Signal Strength

If the pulse lasts 10^{-6} seconds, the signal is at least 10^5 times as large as needed by a good photomultiplier detector, such as a 1P28. The range of the instrument is then from approximately 10^{-8} gm/cm³ to 10^{-14} gm/cm³ when the sampling is done at a distance of 300 cm from the vehicle. The lower limit to the density is determined mainly by the background skylight, rather than noise in the phototube.

5.1.3 Sky Background

An average albedo light at 30 km is 500 candles/ft² = 0.5 lumens/cm²-sterad. At 5550 Å, 621 lumens = 1 watt. The background is then 8.1×10^{-4} watts/cm²-sterad. If the photomultiplier is observed for 10^{-6} seconds, the background light is 8.1×10^{-10} joules/cm² sterad = 8.1×10^{-3} ergs/cm²-sterad. The solid angle of the detector Ω is given by

$$\Omega = \frac{a}{R^2} \quad (19)$$

where a is the projected area of the observed region on a sphere of radius R. An approximation is

$$a = 100 \text{ cm} \times 10 \text{ cm} = 1000 \text{ cm}^2$$

then

$$\Omega = \frac{10^3}{9 \times 10^4} = 1.1 \times 10^{-2} \quad (20)$$

We find that for a 1.5 cm^2 photocathode, the background light energy E_B is

$$E_B = 8.1 \times 10^{-3} \times 1.5 \times 1.1 \times 10^{-2} = 1.35 \times 10^{-4} \text{ ergs}$$

or the number of background photons is

$$\bar{N}_B = \frac{1.35 \times 10^{-4} \text{ ergs}}{5 \times 10^{-12} \text{ ergs/photon}} = 2.7 \times 10^7 \text{ photons} \quad (21)$$

If the albedo light varies with altitude, as does the density of the atmosphere, the number of noise photons should be down by a factor of 10^4 from the signal. In the very unlikely event that it is constant between 30 km and 100 km, one will have trouble at a density of 10^{-12} gm/cm^3 and less. If the albedo drops only by a factor of 100 between 30 km and 150 km (a conservative estimate since the density drops by a factor of 10^7) we will have at least a 20:1 signal-to-noise ratio up to 300 km altitude. Thus, the device should be effective well above 300 km. A technique for background suppression is discussed in Subsection 5.1.8.1.

5.1.4 Ultraviolet Source Type

The excitation source presents the only major difficulty in designing the air density instrument. The first approach to this problem was to use an electron gun as a source of excitation energy. Calculations revealed that when using a 100 keV electron beam the scatter due to the shockwave would completely diffuse the beam and render it useless.

A second approach was to use a laser beam as an excitation source. Only a ruby laser would yield a useful power output, and this wavelength is about 6943 \AA . What must be avoided here is the use of an excitation source at or near the same wavelength region of the detector. The reason for this is that direct reflection from dust particles or ice crystals may cause an erroneous input signal to the detector. We investigated a method whereby two laser beams intersected at the remote point of interest causing frequency doubling or excitation at a half wavelength at

the remote point. However, it was not clear that this effect would be reliable for a variable air density environment, and also the efficiency of frequency conversion was questionable.

A third and final approach was to use a collimated spark discharge as an excitation source. In an abstract by H.E. Hinteregger (Ref. 31), the photoionization cross section for molecular nitrogen is given as $2 \times 10^{-17} \text{ cm}^2$, for a wavelength region of 500 Å to 700 Å. From this it would appear that a spark source emitting within the 500 Å to 700 Å area would be most readily absorbed by molecular nitrogen, and we anticipate that this energy would be reradiated in the visible portion of the spectrum. Mr. G.L. Weissler of the University of Southern California, reported in his paper (Ref. 32) that a 555 Å source was used by coworkers and himself to excite molecular nitrogen, with about 5 percent of the input energy being reradiated in the visible spectrum.

It is this spark source system radiating at one wavelength and reradiation and detection at another wavelength that seems most promising for an air density measuring instrument.

5.1.5 Ultraviolet Source Configuration

The ultraviolet beam can be collimated with a reflecting mirror placed an appropriate distance away from the spark gap. As described by G. Hass, R. Tousey, and coworkers (Ref. 33) the best reflecting surface for a wavelength region between 500 Å and 700 Å is evaporated platinum of about 300 Å thickness. Figure 12 is a copy of the reflectance curve for platinum. As indicated, the total reflectance expected at 600 Å is about 20 percent. This figure combined with the 5 percent reradiation factor indicates that, for every 100 watts of power input to the spark, 1 watt will be in the form of visible radiation. The total conversion factor will be a very adequate 1 percent.

The mirror substrate would most effectively consist of a fused-quartz mirror ground and polished to an appropriate focal length. A convenient size would be 4 inches in diameter and 3/4 inch thick with an 8-inch focal length. The supporting tube would then

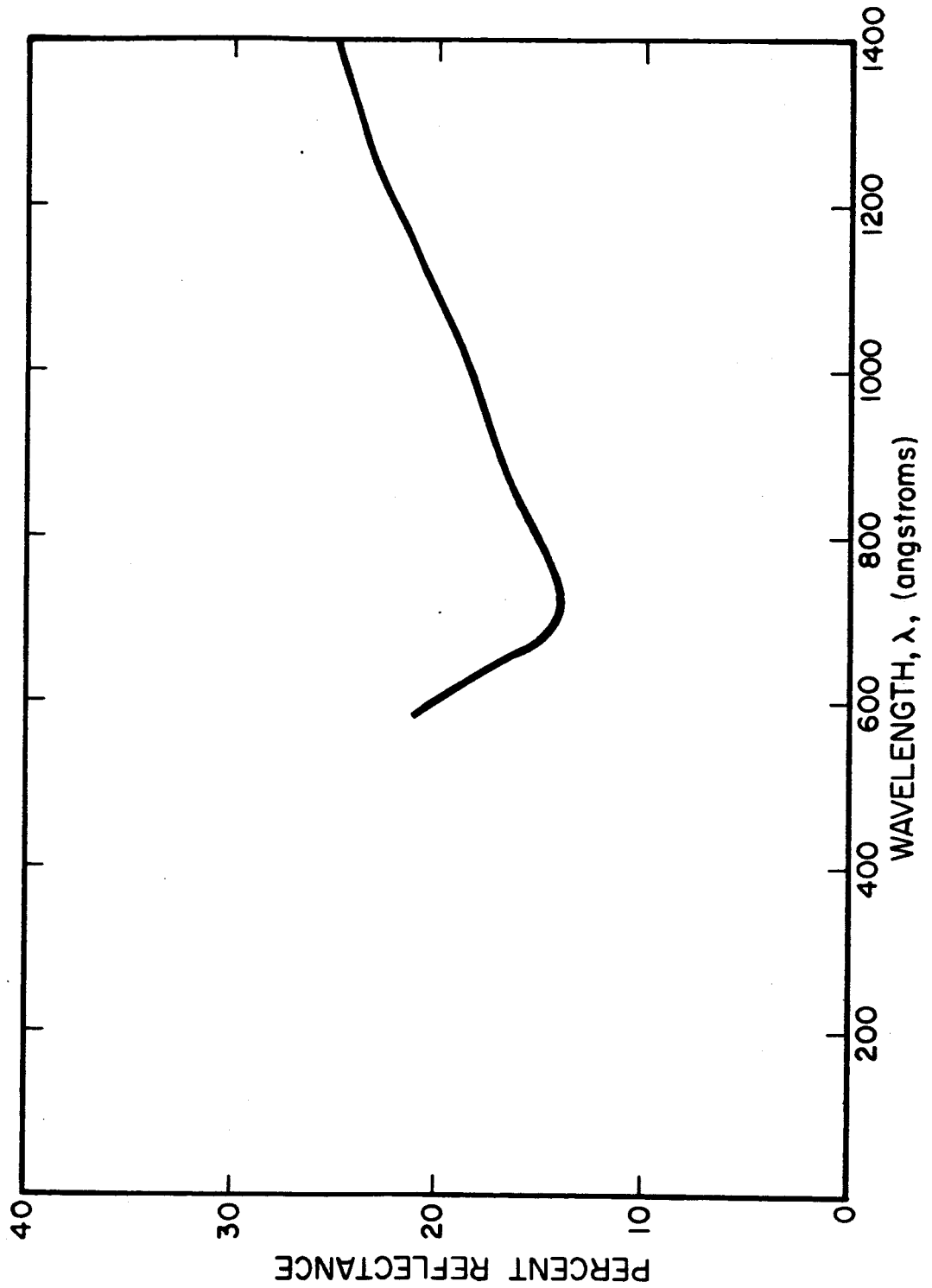


FIG. 12 REFLECTANCE OF PLATINUM

measure 12 inches in length, 5 inches in diameter, and 1/8 inch wall thickness and could either be aluminum or fiberglass. Referring to Fig. 13, (A) represents the support tube, and (B) the mirror (directly behind the mirror is a group of three spring-loaded adjusting screws for use in alignment of the focus); (C) is the partially open end of a coax line which contains the spark gap; (D) is the high-voltage coax line from the high-voltage power supply and is fabricated from concentric copper tubing; (E) is a double-ended rotary filter assembly which is rotated at a predetermined rate through a gear linkage and motor assembly at (F). The filter will consist of ultraviolet absorbing glass and an opaque window. The filter assembly is used for in-flight instrument calibration as discussed in Subsection 5.1.8, Error Sources. (G) is a phototransistor at the end of a small collimating tube. This device will be used to monitor the spark intensity and timing.

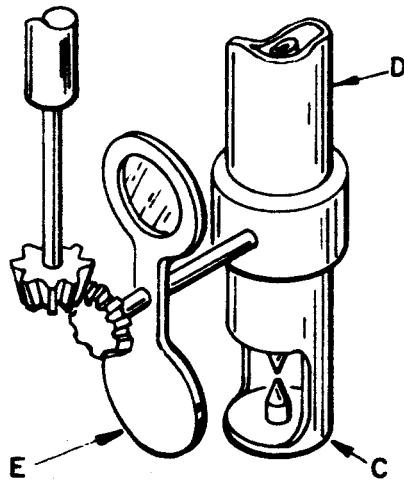
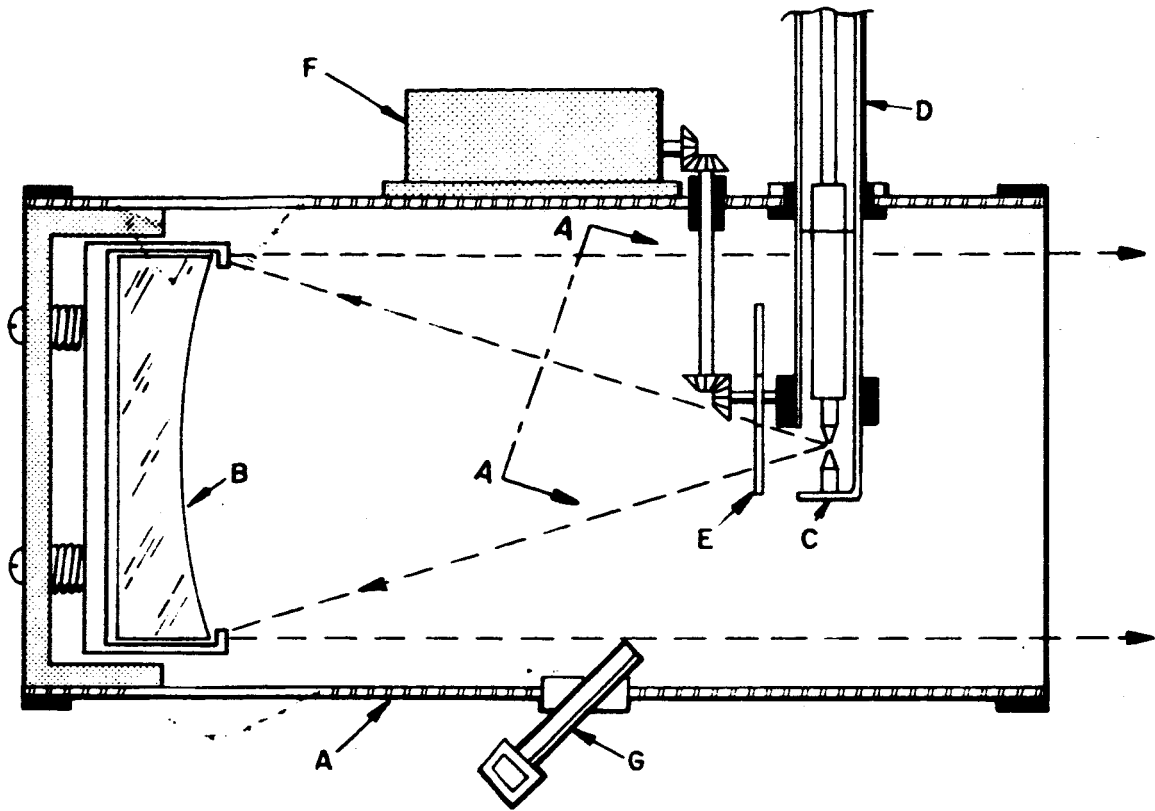
A chronic problem with density gages is the large dynamic range encountered. We propose to circumvent this by varying the energy to the spark source with altitude to maintain a reasonably constant return signal. Source characteristics are sufficiently flexible that this can be done with relative ease. The less flexible photomultiplier detector, then, needs a dynamic range of only 100 to 1.

5.1.6 Detector

About 5 percent of the ultraviolet light sent outward from the missile in a collimated beam will be reradiated as visible light, and a portion of this beam will be collected by the detection instrumentation.

The dimensions and outward appearance of the detector will closely resemble the spark source instrument. The collecting mirror would be of the same size and focal length but could be made of pyrex and coated with aluminum.

Referring to Fig. 14, (A) is the instrument support tube, and (B) is the aluminized mirror; (C) is an aluminized flat diagonal mirror that is used to direct the incoming light to one side and onto



SECTION A—A

FIG. 13 SOURCE CONFIGURATION

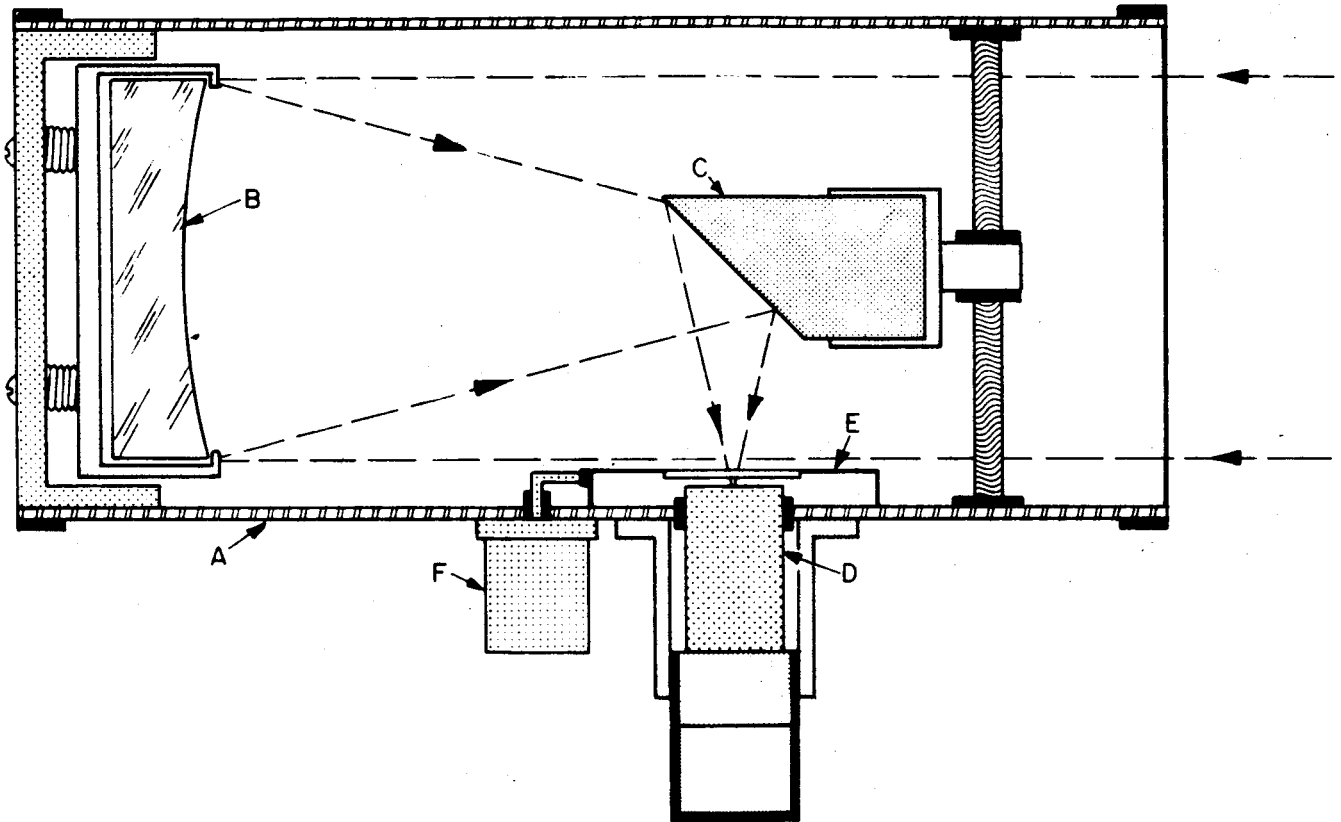


FIG: 14 DETECTOR CONFIGURATION

the face of the photomultiplier tube (D); (E) is a shutter to control the detection of incident light and (F) the shutter actuating mechanism. The shutter is operated synchronously with the rotary filter in the source instrument and is employed for calibration purposes (see Sub-section 5.1.8).

5.1.7 Instrument Circuit

The complete density instrument circuit is depicted in block form in Fig. 15. The spark timing circuit will depend upon the charging rate of the capacitor banks in the high-voltage power supply and should be capable of about one pulse per second for each capacitor bank.

The timing circuit will also produce a triggering signal for the P-M tube so that the P-M tube will only operate during the duration of the spark; about 1 microsecond. This circuit will also be used to limit dynode current to a safe maximum to prevent tube damage in case of an unusually large light input, such as would occur with an accidental sweep past the sun.

The amplifier circuit will contain a stable zero output reference level and the varying pulse amplitude will be a direct measure of gas density. A phototransistor can be used at the source so that any variation in spark amplitude can be accounted for at the detector.

The variable amplitude output signal can then be fed to the telemetry circuitry.

5.1.8 Error Sources

The absolute accuracy of the air density measurement depends on a knowledge of the sky albedo, internal background and systematic errors in the determinations. The internal background to the desired signals will arise from extraneous electrical signals that might simulate the phototube, or from visible light from the source that is reflected or scattered into the phototube by dust particles,

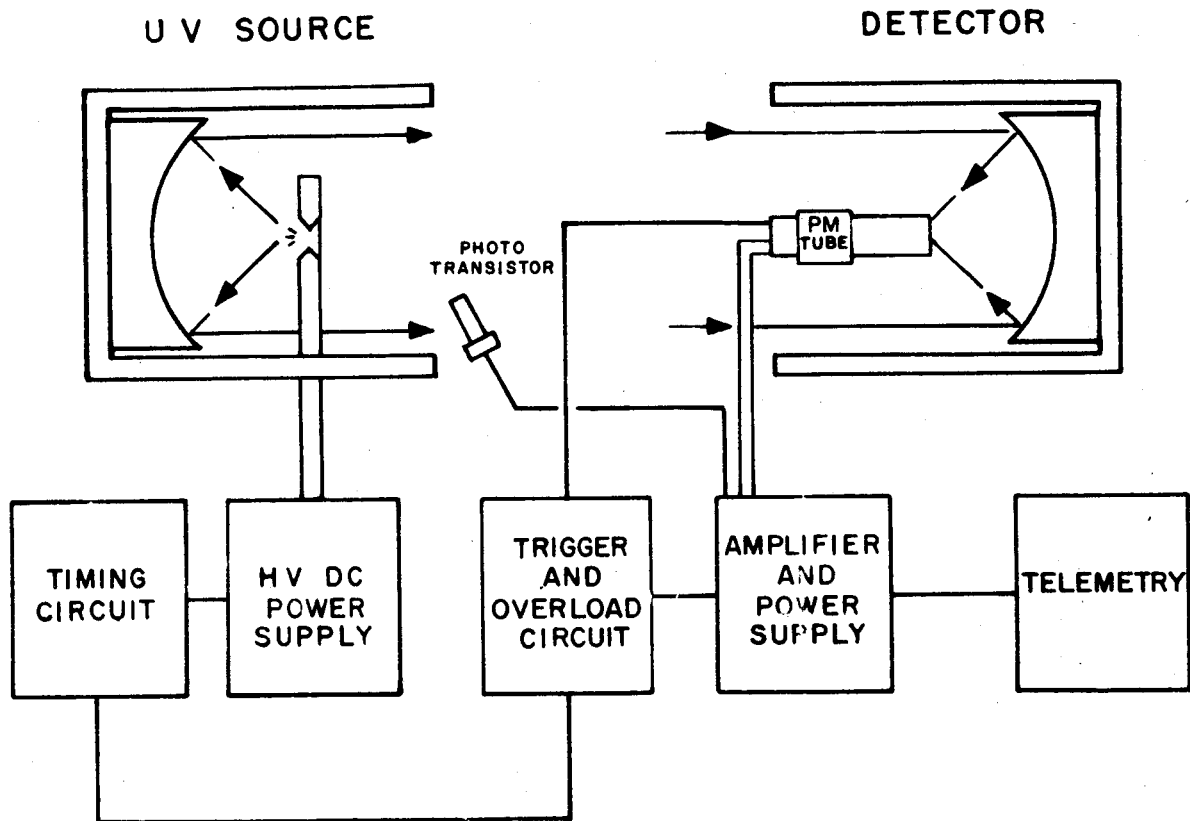


FIG. 15 ULTRAVIOLET AIR DENSITY GAGE SCHEMATIC

ice crystals, engine exhaust products or other condensed matter. The systematic errors will arise from nonlinearities in the detection system and from variations in the source strength.

5.1.8.1 Background Error Suppression

The backgrounds in this instrument can be measured during flight by the following method. Inasmuch as we desire to measure the amount of visible light emitted by gas excited by 500 Å to 700 Å ultraviolet light, we can measure the phototube signal both with and without the ultraviolet light being emitted from the source. Thus, one determines the amount of visible light that actually originates in the interactions of the 500 Å to 700 Å photons by subtracting the incident irradiance when the source is not emitting from the irradiance when it is emitting.

$$H_{\text{Gas}} = H_{\text{Total}} - H_{\text{Background}} \quad (22)$$

H_{Total} is the total visible light signal that is seen by a 1 cm^2 element of the phototube. When the ultraviolet absorbing filter shown in Fig. 13 (which eliminates all wavelengths shorter than 2000 Å) is placed in front of the source, the visible light signal $H_{\text{Background}}$ which the phototube senses is due only to specular reflection of the visible light emitted by the spark source. H_{Gas} , then, is the visible light signal actually due to the gas being excited to fluorescence. The strength of this latter signal is directly related to the density of the gas.

The density instrument must be sensitive to a small signal of short duration, and so it also may be subject to electrical interference from the spark source or other equipment on board the rocket. If one can assume that the extraneous signals are unvarying in successive periods of time, then the subtraction performed to extract the signal due only to the ultraviolet interactions will eliminate the interference of the electrical noise. This will be particularly true of the extraneous signal from the spark source, which definitely should be unvarying with each spark.

If one makes the following measurements during every time period (each second for example):

H_R : total signal with no filter

H_B : signal with the ultraviolet filter in front of the source

H_S : signal with the opaque filter in front of the source, but source pulsed

H_P : signal with phototube covered, but source pulsed

then one can determine the following quantities:

$$H_{\text{Gas}} = H_R - H_B: \text{signal related directly to the gas density} \quad (23)$$

$$H_{\text{Dust}} = H_B - H_S: \text{signal related to the area of specular reflecting material suspended in the gas} \quad (24)$$

$$H_{\text{Albedo}} = H_S - H_P: \text{signal related to the albedo light} \quad (25)$$

(also see Subsection 5.1.3)

5.1.8.2 Nonlinearity

The systematic errors due to nonlinearities in the system can be greatly reduced by adjusting the source strength as a function of altitude such that the received signal is always at approximately the same amplitude. Most phototubes are linear over a 100 to 1 dynamic range while the density between 80 km and 350 km varies over a range of 10,000 to 1. Thus, a scheme for varying the source strength will be necessary if nonlinearities are to be avoided. These variations in the source strength must be monitored and recorded for each pulse to accurately give the necessary scale factor.

If the total linearity due to both the source monitor and the phototube amplifier are known to 1 percent, the systematic error in the density measurement will be 1 percent.

5.1.9 Accuracy

It is not possible to calculate the accuracy of the density gage from physical laws and existing data. The accuracy of the instrument must be determined by calibration. Thus, the accuracy

of the density gage will depend to a great extent upon the accuracy of the calibration.

To meet the accuracy requirement of 1.5 to 2 percent of the reading specified under the current contract is a formidable task. Conventional high-altitude density gages have accuracies of a few percent of full scale which can amount to 100 percent of the reading at the higher altitudes. For this reason we recommend a two stage development of the gage. The first stage should seek to verify the promising results of our analysis by building and testing a breadboard. We anticipate that a 10 to 20 percent accuracy could be achieved here. The second stage should be to fabricate and ground test a flight prototype. Refined components and design techniques should be utilized here and it should be possible to achieve the 1.5 to 2 percent accuracy with this version of the gage. This accuracy is, of course, contingent upon sufficiently accurate vacuum calibration facilities being available.

Let H_R be the total signal received by a unit area of the photomultiplier. H_G is the signal due to the ionization of the gas, and H_B is the background signal as in Subsection 5.1.8.1. Then repeating Eq. 23:

$$H_G = H_R - H_B$$

Let K be defined by

$$H_B = KH_R \tag{26}$$

Then as the variation:

$$(\partial H_G)^2 = (\partial H_R)^2 + (\partial H_B)^2 = (1 + K^2)(\partial H_R)^2 \tag{27}$$

The fractional error in the gas signal is:

$$\frac{\partial H_G}{H_G} = \pm \frac{\sqrt{1 + K^2}}{1 - K} \frac{\partial H_R}{H_R} \tag{28}$$

Now

$$\frac{\partial H_R}{H_R} = \frac{\sqrt{N}}{N} = \frac{1}{\sqrt{N}} \quad (29)$$

where N is the number of photoelectrons at the first dynode of the photomultiplier. Finally we get

$$\frac{\partial H_G}{H_G} = \pm \frac{\sqrt{1 + K^2}}{1 - K} \cdot \frac{1}{\sqrt{N}}$$

As H_G is proportional to the density of the gas ρ ,

$$\frac{\partial \rho}{\rho} = \pm \sqrt{\frac{1 + K^2}{N}} \cdot \frac{1}{(1 - K)}$$

The number of photoelectrons at the first dynode is approximately one-tenth the number of photons incident on the photocathode. Thus, for a minimum of 10^4 photons, $N = 10^3$. This can be maintained up to a density of 10^{-13} gm/cm³, but will decrease with decreasing density due to the lack of source power. From the graph in Fig. 16, one can read off the accuracy of the instrument as a function of the number of incident photoelectrons and K . The actual construction of such a graph would be part of the calibration procedure.

If we choose a source strength as a function of density to give the number of photoelectrons as sketched in Fig. 17, then the absolute error in density can be expressed by

$$\partial \rho = \pm \sqrt{\frac{1 + K^2}{N}} \cdot \frac{\rho}{(1 - K)}$$

This relation is sketched in Fig. 18.

We must keep in mind, however, that there would always be a lower limit to the error. This will be equal to the error in the knowledge of the systematic effect of nonlinearity in the monitoring and detection system no matter how large N becomes. Thus, if the known limit of linearity is 1 percent, there would not be much point in arranging for more than 10^4 photoelectrons (equivalent to 10^5 photons) at the phototube.

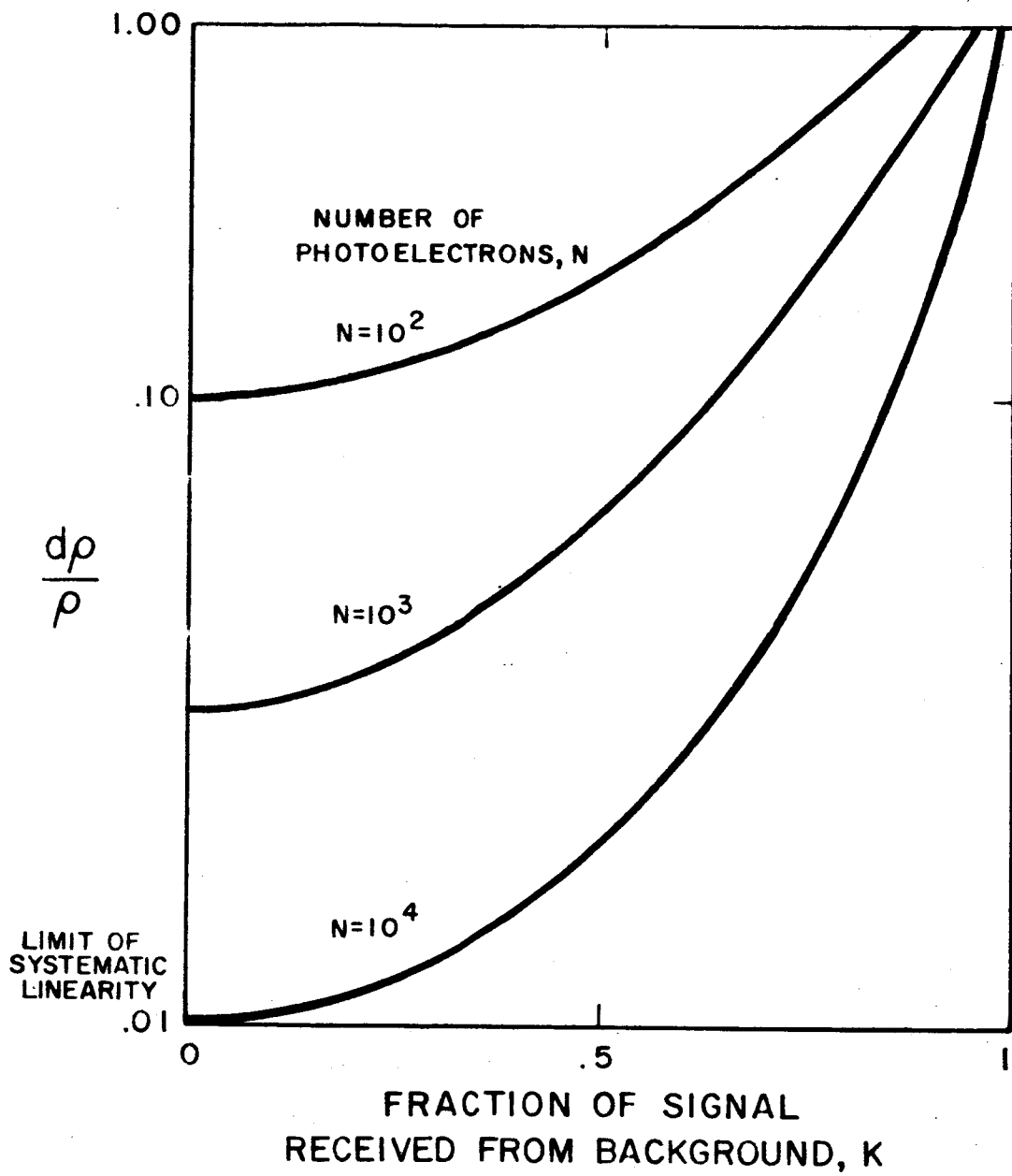


FIG. 16 EFFECT OF NUMBER OF PHOTOELECTRONS

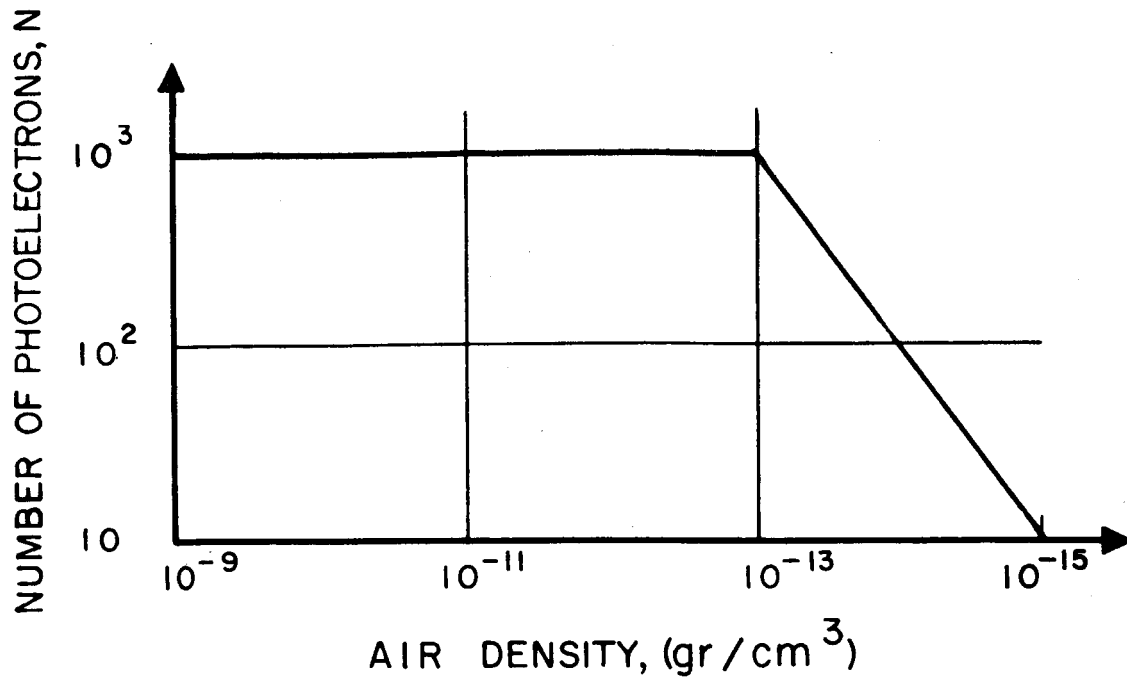


FIG. 17 NUMBER OF PHOTOELECTRONS

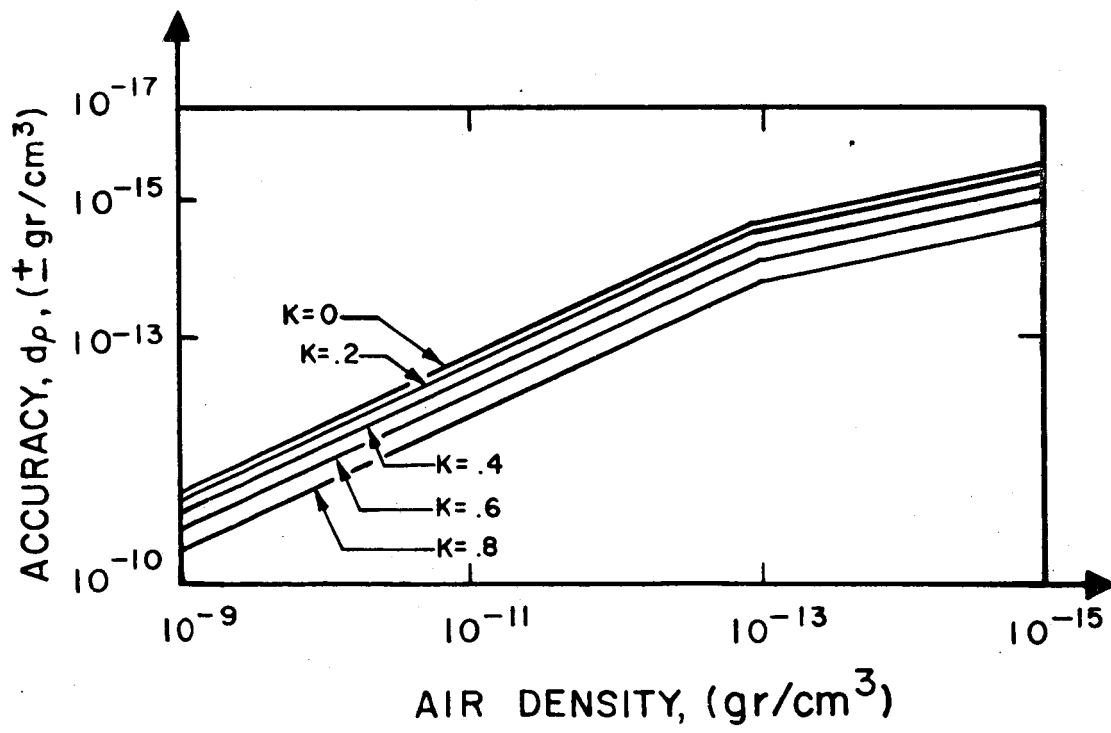


FIG. 18 ACCURACY OF GAGE READING

5.1.10 Calibration

The accuracy of this instrument rests on its calibration. If an absolute accuracy of 2 percent is desired, the calibration accuracy must be at least that good. This means that precise techniques must be used in all aspects of the design and construction of the instrument and the calibration apparatus.

5.1.10.1 Calibration Apparatus

The source is mounted in the end of a high-vacuum chamber. It produces a beam of ultraviolet plus visible light that transverses the vacuum chamber and the gas in it. The photomultiplier detector observes a volume of the beam through a window. The vacuum chamber is then pumped down to a low pressure and a controlled amount of gas is let in. The source is pulsed and its output monitored, while the fluorescent yield is measured by the photomultiplier detector.

5.1.10.2 Requirements on the Technique

Each of the following items must be known within a given percent if one is to achieve a given percent instrument.

1. The variation of source strength from pulse to pulse.
2. Reflection from walls of the calibration chamber.
3. The exact volume of air contained within the intersecting light beam and detector field of view.
4. Linearity and gain stability of all amplifiers and readouts.
5. Amount and composition of the gas in the test chamber.

These are the items that will be given careful consideration during the test phase of the density gage development.

5.1.10.3 Calibration Procedure

After all the above requirements are satisfied the calibration would proceed as follows. First, the chamber must be pumped down until the residual gas density is less than 1 percent of the density of the gas to be measured. The vacuum pump must be closed off and it must

be ascertained that during the measurement time no significant leakage or outgassing takes place. Then a carefully measured amount of gas is introduced into the chamber. Its density is known by the ratio of volumes of the chamber and the gas measuring vessels. The source is then pulsed and the detected signal recorded. The ultraviolet light is then filtered from the beam and the test repeated. Finally, the beam from the source is absorbed before entering the chamber and the source pulsed.

By taking the difference between the final two measurements, one knows the signal due to the fluorescence of the gas at a particular density and source strength. By taking the difference between the second and third measurements, one measures how much reflected visible light exists in the chamber.

This process is repeated for different gases and densities until the instrument is calibrated and the total fluorescence yield as a function of gas density is known. Then, by correcting for the difference in solid angles between the test setup and the actual flight configuration, the detector output for a given gas density can be predicted.

5.1.11 Operation Below 75 km

At present the EOS ultraviolet densitometer does not compete with current densitometers below 75 km. At 500 Å to 700 Å, the absorption cross section is so large that the penetration distance is on the order of only centimeters in the higher densities of the mesosphere and stratosphere. A possible way to extend it to lower altitudes might be to use longer wavelength radiation, 1000 Å to 2000 Å, where the absorption cross section is lower, and to look at weaker fluorescent resonances. These should be detectable because the density of the atmosphere has increased and so the reaction probability has also. Sources for this wavelength are available, but this extension will require new experimental work on the nature of the fluorescence to be expected.

5.1.12 Instrument Location

Shockwaves will exist at the apex and edges of all the stages of the missile as depicted in Fig. 11. This situation requires

that air density measurements be made a decimeter or two above the nose, or no less than 10 meters from the side of the missile. The figure shows probable locations for one or more air density measuring instruments. As indicated, one instrument might be located in the escape rocket tip near the apex of the bow shockwave. This would be a logical placement for an instrument operating at the lower altitude range since the vacuum ultraviolet is readily absorbed and the beam penetration distance for a practical instrument will be less than 1 meter. This instrument will be lost when the escape tower is jettisoned.

Another instrument is carried in the inner stage structure for use at altitudes above where the escape tower is jettisoned, and it is this instrument that is discussed in detail in this section.

5.2 Filter Photometer Air Density Gage

Another promising density technique is to measure the variation of the radiated ultraviolet solar energy in selected wavelength bands as the rocket ascends, and thus determine the absorbing air mass between the rocket and the sun. Data taken in this way is little affected by the pressure field distortion caused by shock waves or by local contaminants. The absorbing air mass may be converted into air density with the knowledge of the relative atmospheric composition and ultraviolet absorbance. These data are known with sufficient accuracy to enable the density determination to an accuracy of 10 percent. Compared with current density gage accuracy at high altitudes, this instrument would be very good.

The following sections cover the analytical aspects of the photometer in some detail and suggest a practical instrument design.

5.2.1 Theory

Atmospheric density can be determined by measurements of optical absorption of the sun's radiation in various spectral regions in accordance with the equation

$$\ln \frac{I_2}{I_1} = \alpha H \rho_2 \exp \left(\frac{h_2 - h_1}{H_1} - 1 \right) \quad (30)$$

where

I = radiant flux

α = mass absorption coefficient

h = altitude

H = scale height

ρ = density

Subscript

1 = lower altitude

2 = higher altitude

The absorption coefficient, α , depends on the molecular species responsible for the absorption; which in turn determines the choice of

wavelength. From about 40 km to 90 km altitude, the absorption is almost exclusively due to molecular oxygen. Since the composition of the atmosphere shown in Table II appears to be constant up to about 90 km, a determination of the amount of absorption by molecular oxygen will yield an accurate measure of the density at the instrument. In order to span such a wide range of altitude, it probably will be necessary to monitor the absorption in at least three and possibly four different wavelengths, beginning with 2,000 Å at 40 km and diminishing to 1,800 Å at 90 km. Above 90 km oxygen is dissociated, so that measurements based on molecular oxygen are no longer useful. At high altitudes, one can use the absorption of soft x rays, which is proportional to total mass and is independent of molecular aggregation.

It appears that the lowest level to which one could extend this technique is about 40 km. The region lower than 40 km presents a special problem. At these altitudes ultraviolet energy below 2,000 Å is mostly absorbed by the upper atmosphere, and that above 2,000 Å is absorbed by ozone. The only apparent solution is to monitor ozone absorption and correlate the ozone density with the oxygen density on the basis of the photochemical reactions involved.

5.2.2 Wavelength Selection

Absorption of electromagnetic radiation may take place through several mechanisms: ionization and reemission, photon capture and dissociation, resonance absorption and multiple scattering. Reference to the ultraviolet absorption spectra of the atmosphere will show that the presence of oxygen absorption bands is quite prominent between 2,000 Å and 1,000 Å. At longer wavelengths above 2,000 Å, the absorption due to ozone is prominent.

The absorption may be calculated by Lambert's relation

$$I = I_0 e^{-\mu x} \quad (31)$$

where

I_0 = the original intensity

μ = the absorption coefficient

x = the path length in cm at STP (760 torr and 0°C)

TABLE II

COMPOSITION OF ATMOSPHERE

Altitude km	P (torr)	σN (N/cm^3)	T ($^{\circ}K$)	N_2 (N/cm^3)	O_2 (N/cm^3)	O_3 (N/cm^3)	O (N/cm^3)
0	760	2.5×10^{19}	288	2.1×10^{19}	5.6×10^{18}		0
20	41.3	1.85×10^{18}	217	2.1×10^{19}	5.6×10^{18}	2.4×10^{13}	
30	8.9	3.7×10^{17}	231	2.1×10^{19}	5.6×10^{18}	2.4×10^{13}	
40	2.25	8.3×10^{16}	261	2.1×10^{19}	5.6×10^{18}	0.43×10^{13}	
50	0.675	2.3×10^{16}	283	2.1×10^{19}	5.6×10^{18}	0.59×10^{12}	
60	0.191	7.53×10^{15}	245	2.1×10^{19}	5.6×10^{18}	0.8×10^{11}	
70	35×10^{-6}	1.96×10^{15}	173	2.1×10^{19}	6.9×10^{14}	0.68×10^{10}	5×10^{11}
80	50×10^{-6}	2.84×10^{14}	168	2.1×10^{19}	6.9×10^{14}		0.10^{12}
90	7.1×10^{-6}	3.9×10^{13}	176	2.1×10^{19}	1.8×10^{13}		
100	1.3×10^{-6}	6.0×10^{12}	208	4.8×10^{12}			
120	0.25×10^{-6}	6.3×10^{11}	390				
140	0.078×10^{-6}	1.07×10^{11}	662				
160	0.038×10^{-6}	4.0×10^{10}	926				
	*1	*1	*1	*2	*2	*2	*2

*1 U.S. Standard Atmosphere, 1962

*2 Physics of the Upper Atmosphere, Ratcliff, 1960

The absorption coefficient μ is independent of temperature and pressure and related to the absorption cross section σ by:

$$\mu = \sigma N$$

where N is the Loschmidt number, 2.687×10^{19} number/cm³. The cross section is dependent on which of the particular absorption processes predominates - resonant absorption in the current instance.

The transmission, T , is defined as:

$$T = \frac{I}{I_0} = e^{-\mu x} \quad (32)$$

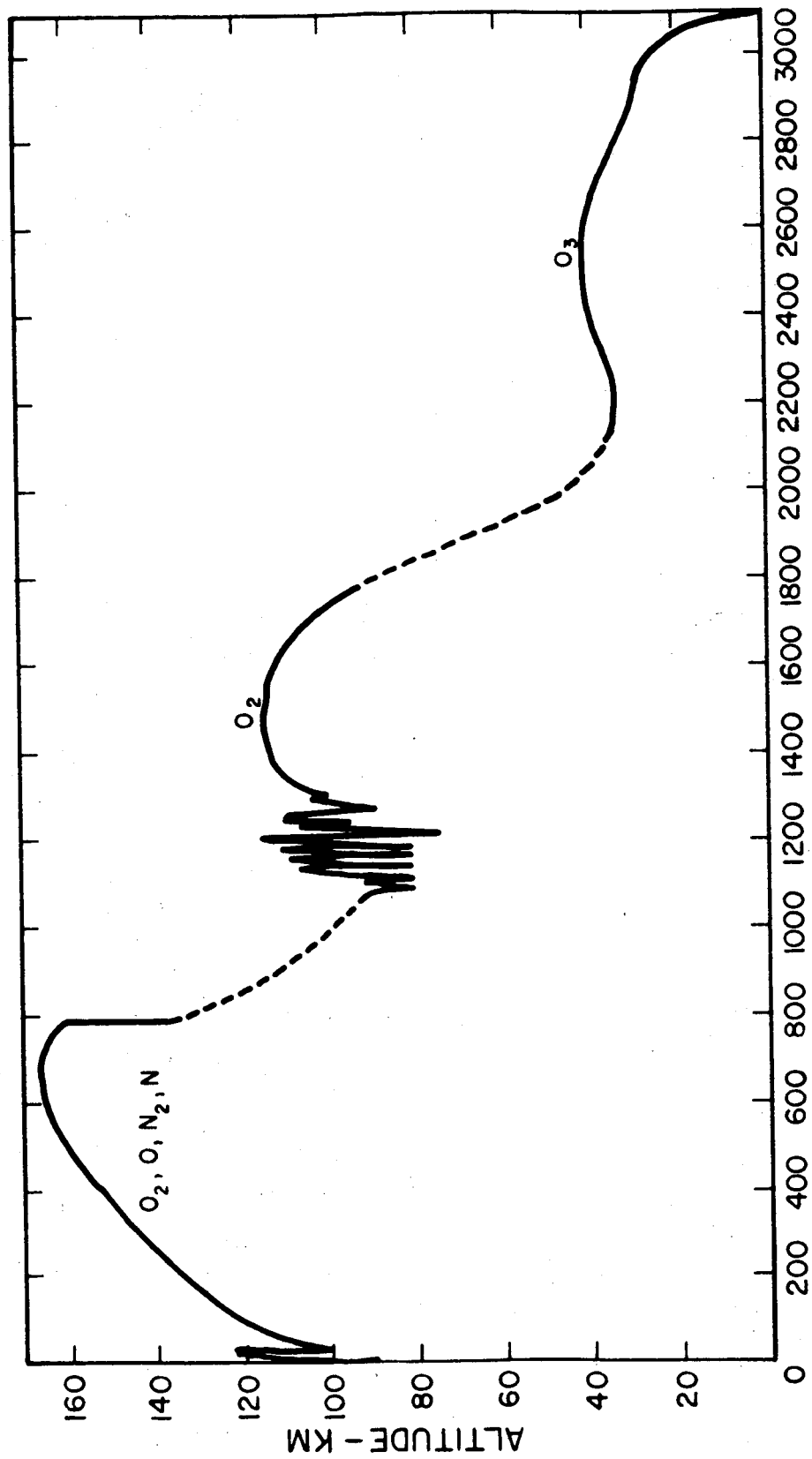
The scale height, H_n , is defined as the distance traversed for a change in intensity of e^{-1} , namely:

$$H_n = \frac{1}{\mu} \quad (33)$$

The altitude at which the solar radiation in the earth's atmosphere falls to e^{-1} of its original intensity is shown in Fig. 19 (Ref. 34.) Absorption above 2,000 Å is principally due to ozone, between 850 Å and 2,000 Å to molecular oxygen, and below 850 Å to all constituents. The transmission is shown in Fig. 20. These two graphs will be used to select the appropriate wavelength bands in which the density may be measured between 30 and 150 km.

Referring to Fig. 20, it can be seen that above about 80 percent and below about 10 percent the transmission percentage changes very little with altitude. This is due to the exponential behavior of Eq.32. Thus, we see that the useful dynamic range is perhaps 8:1, or 80-percent to 10-percent transmission. This is roughly two scale heights ($e^2 \sim 7.4$).

Wavelength selection will therefore be determined by going up or down one scale height from the curve in Fig. 19. Optical scale height versus altitude is given in Table III for the U.S. 1962 Standard Atmosphere. For example, starting at 48 km one



WAVELENGTH - ANGSTROMS

FIG. 19 PENETRATION OF SOLAR RADIATION INTO THE ATMOSPHERE

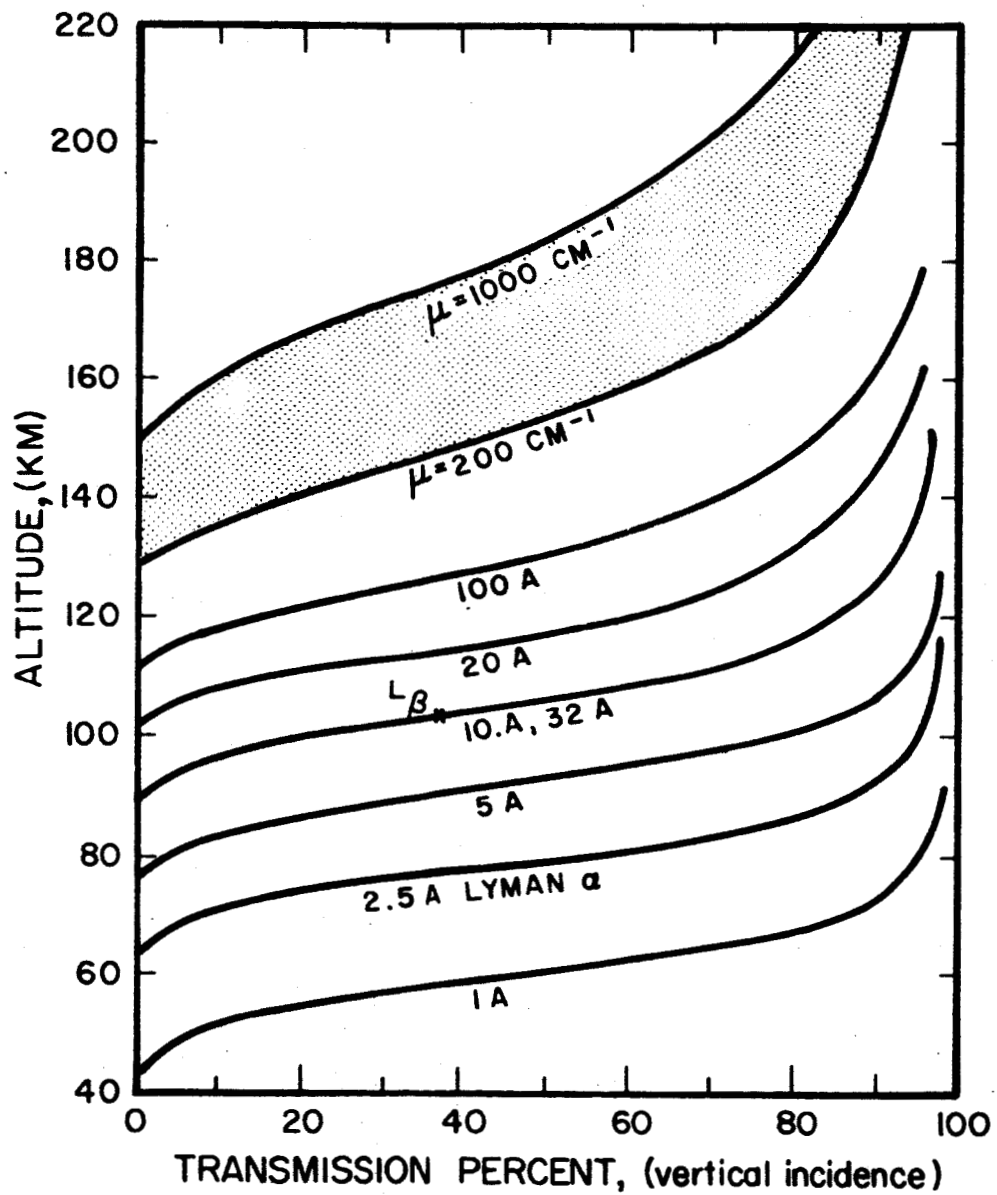


FIG. 20 ATMOSPHERIC TRANSMISSION IN X-RAY AND ULTRAVIOLET IONIZING WAVELENGTHS WHEN THE SUN IS OVERHEAD

TABLE III
OPTICAL SCALE HEIGHT AND NUMBER DENSITY

Geometric Altitude Z (km)	Optical Scale Height H _n (km)	Number Density (No./cm ³)
0	8.4	2.5×10^{25}
30	6.7	3.8×10^{23}
40	7.4	8.3×10^{22}
50	8.0	2.1×10^{22}
60	7.6	6.3×10^{21}
70	6.6	1.8×10^{21}
80	5.4	4.1×10^{20}
90	5.5	6.5×10^{19}
100	6.4	1.0×10^{19}
120	10.9	5.2×10^{17}
140	23.3	7.5×10^{16}
160	34.7	2.6×10^{16}

scale height (~ 8 km) up and down covers the interval from 40 to 56 km altitude. Referring to Fig. 19, the wavelength selected would be $\sim 2,000 \text{ \AA}$, or just where molecular oxygen O_2 starts to become the principal absorber. The detector should then be sensitive to energy from $2,000 \text{ \AA}$ down. No harm will be done by having a detector sensitive to the shorter wavelengths since Fig. 20 shows that they do not penetrate strongly to 56 km and below. The next range of approximately two scale heights is from 56 km to 78 km. Here a wavelength of $1,900 \text{ \AA}$ down is appropriate. The third range of $1,800 \text{ \AA}$ down takes the upper limit to 90 km. Above 90 km, a convenient radiation source is the solar Lyman α emission line at $1,215 \text{ \AA}$. This source has been used before (cf. page 165, Ref.34) in the range of 90 to 120 km. It is a nearly monochromatic source at a wavelength where oxygen is the only absorber. Above 120 km the solar x-ray flux is of sufficient intensity to be used as a source. The radiation reaching the detector is then only a function of air mass and is independent of particular absorbing species. This is an important advantage at higher altitudes where the ratio between molecular oxygen and the total air mass is not known accurately.

Table IV summarizes the wavelengths and absorbing species that should be used for various altitude intervals.

TABLE IV
WAVELENGTHS AND ABSORBING SPECIES

Altitude (km)	Wavelength (\AA)	Principal Absorbing Species
40 - 56	2000 down	O_2
56 - 78	1900 down	O_2
78 - 90	1800 down	O_2
90 - 120	1215 down	O_2
120 - 200	44 - 100	all gases

5.2.3 Optical Materials

5.2.3.1 Windows

The choice of window materials in the vacuum ultraviolet between 2,000 Å and 1,000 Å is fairly restricted. Referring to Table V it can be seen that the fluorides are the only useful materials for windows.

TABLE V
TRANSMISSION OF VARIOUS MATERIALS
IN THE VACUUM ULTRAVIOLET

<u>Material</u>	<u>Thickness (mm)</u>	<u>Short Wavelength Transmission Limit > 10% (Å)</u>	<u>Notes</u>
Lithium fluoride, LiF	0.4	1050	Moderate absorption to 1,300 Å
Calcium fluoride, CaF	3.0	1220	Sharp cutoff 1,215 Å
Sapphire	0.5	1425	Sharp cutoff 1,415 Å
Fuzed Quartz	1.0	1560	
Strontium fluoride, SrF ₂	0.88	1200	Sharp cutoff 1,270 Å
Sodium fluoride, NaF	1.37	1310	Sharp at 1,276 Å

In the case of 44 - 100 Å x rays, a thin window on a hydrocarbon material, such as Mylar or Glyptal, is satisfactory. Such materials do not have absorption bands in this range. Metal windows in this range have absorption edges which complicate detector calibration and lower the sensitivity.

Because of the large range of wavelengths to be monitored with the inclusion of the 1215 Å Lyman α line, lithium fluoride is recommended as a window material and also as a substrate for filter elements for the vacuum ultraviolet portion of the spectrum.

5.2.3.2 Filter Materials

As was the case with windows, very few types of filters are available in the vacuum ultraviolet. Interference filters cannot be fabricated at these short wavelengths due to lack of

suitable optical materials; therefore one is restricted to absorption filters. These filters do not have a sharp longwave cutoff but, rather, an attenuation that follows the relation:

$$T = \exp(-4kx/\lambda_0)$$

T is the transmission of light of wavelength λ_0 through a film having an extinction coefficient k and thickness x.

Several metals are suitable for such a film; for instance, aluminum, chromium, gold or rhodium. As an example, the values for which aluminum absorbs 99.5 percent of the incident radiation are shown in Table VI which was taken from Ref. 35.

TABLE VI
THICKNESS OF ALUMINUM FILMS FOR WHICH
THE TRANSMISSION IS 0.5 PERCENT

<u>Wavelength (Å)</u>	<u>Film Thickness (Å)</u>
3,000	390
2,200	450
1,216	700

The extinction coefficient of several suitable metals is tabulated below from Ref. 35.

TABLE VII
EXTINCTION COEFFICIENTS OF FILTER MATERIALS

<u>Metal Film</u>	<u>Wavelength, λ_0 (Å)</u>	<u>Extinction Coefficient, k</u>
aluminum	2200	2.35
chromium	1930	1.17
gold	2000	0.92
rhodium	2536	0.056

Since gold is easily evaporated and has a low extinction coefficient, it is recommended as the filter metal. The low extinction coefficient permits the density of the filter to be controlled with a high degree of precision; it also allows a longer deposition time, which ensures a more homogenous film.

5.2.4 Incident Energy

Three independent data: solar flux, atmospheric transmission, and detector response, must be compared in order to arrive at an estimate of the signal output from the detector. The solar spectral radiant intensity in the 60 Å to 2,100 Å range at the top of the atmosphere was taken during 1961 through 1963 by rockets with apogees greater than 300 km and is published in part in Refs. 36 and 37. Using these data, the flux averaged over the band 2,000 Å to 1,300 Å is approximately $0.5 \text{ erg/cm}^2\text{-sec-Å}$. At unit optical depth, that is where the intensity is $1/e$ of the unattenuated value, the average solar flux is roughly $0.18 \text{ erg/cm}^2\text{-sec-Å}$. This is the amount of energy incident upon the detector.

The Lyman α energy is roughly $5 \text{ erg/cm}^2\text{-sec}$ at 1,215 Å as measured at the top of the atmosphere, or $1.8 \text{ erg/cm}^2\text{-sec}$ at a detector placed at unit optical depth, i.e., about 100 km altitude. The total x-ray flux is approximately $0.1 \text{ erg/cm}^2\text{-sec}$ between 60 Å and 100 Å, as measured on high-altitude rocket probes.

5.2.5 Detector Selection

When choosing a detector the spectral response and spectral sensitivity is of first importance. Another important criteria, as far as rocket instrumentation is concerned, is mechanical ruggedness and the support equipment needed. Simplicity of the detector also should weigh heavily in the selection.

Typically, an ultraviolet radiation detector operates by means of photoionization and photoelectron production, depending on the wavelength of the incident radiation. The detector usually

consists of a conducting cavity which may be filled with a gas. Inside the cavity an electrode is introduced, making the detector a two-terminal device. The incident radiation passes through a window and interacts with the gas and the chamber walls. From about 1,000 Å to 1,500 Å the ultraviolet photon has sufficient energy to ionize the filling gas. The ion and the electrons are collected and indicate the presence of the photon. By the proper selection of gases, the response may be enhanced at certain wavelengths, depending on the ionization potential of the gas. Above 1,500 Å the response is almost entirely due to photoelectron production, as in an ordinary phototube. This response may be suppressed by proper tube geometry and quenching gases, which recombine with the photoelectron before it is collected.

Either the photoionization or photoelectron mechanisms may be separated in a particular detector. A phototube employs photoelectron production, while an ion chamber employs photoionization. When both photoelectron production and ionization take place the detector is called a photon counter. As indicated in Table IV, for our purposes it is necessary to have a detector sensitive from 2,000 Å to below 1,500 Å. A separate detector will be used for the Lyman α and the x-ray detector range above 120 km.

In the long wavelength range, $\sim 1,500$ Å to 2,000 Å a photomultiplier tube offers the best solution due to its high sensitivity, higher signal-to-noise ratio, and ready availability. Two types are usable in the vacuum ultraviolet: photomultipliers with alkali cathodes, such as SbCs0 and "nude" photomultiplier structures with AgOCs cathodes. The disadvantage of the SbCs0 cathodes is their longwave response in the visible solar spectrum. The AgOCs cathodes are insensitive above $\sim 2,200$ Å and thus are blind to visible solar radiation. This is the type of detector that is recommended for the longwave region, 2,000 Å to 1,200 Å between the altitudes of 40 and 120 km. A representative tube is the EMI 9603. It is possible to procure this tube with a lithium fluoride window and thus maintain

a vacuum at lower altitudes. The quantum efficiency of the cathode is roughly $0.5 \text{ ergs/cm}^2\text{-sec-}\text{\AA}$, and the total radiation is simply the flux ϕ times the bandwidth $\Delta\lambda$.

$$P = \phi\Delta\lambda = 3.5 \times 10^2 \text{ ergs/cm}^2\text{-sec}$$

The sensitivity, S, of the tube is around 50 mamp/watt or $50 \times 10^{-7} \text{ mamp/erg/sec}$. Thus, the anode current density is

$$J = SP = 175 \times 10^{-5} \text{ mamp} = 1.75 \times \mu\text{amp/cm}^2$$

This means for each square centimeter of collecting area a $1.75 \mu\text{amp}$ signal is developed at unit optical depth. This signal level is quite high and is at least 1,000 times the dark current due to thermionic emission.

The Lyman α detector will consist of an ion chamber of 1 cm^2 aperture and 5 cm^3 volume. The window is of lithium fluoride, 0.5 mm thick. The filling gas is nitrogen dioxide (NO_2) with a partial pressure of 15 torr. This detector produces about 10^{-8} amp of ion current for a Lyman α flux of $1 \text{ erg/cm}^2\text{-sec}$. This current is easily measured. The noise is less than 10^{-16} amp.

The x-ray detector will consist of a Glyptal window photon counter filled with 6.4 torr ethyl formate and 750 torr helium gas. The window density will be 0.2 mg/cm^2 . The aperture will be 0.1 cm^2 with an detector length of 2.0 cm, after Ref. 34. This detector supplies pulses in excess of 10^{-8} amp for the x-ray solar intensity at heights above 120 km. The number of counts per second will be on the order of several thousand above background of < 100 counts/sec due to cosmic rays and hard x rays.

5.2.6 Background Radiation

As mentioned in an earlier section, the detectors have been selected to be insensitive beyond the wavelength of interest. The photomultiplier has a longwave cutoff of $2,200 \text{ \AA}$ and a short wavelength cutoff of $1,050 \text{ \AA}$ due to the lithium fluoride

window. The metal filter will keep the background above its cutoff frequency at a low level, down at least a factor of 50 at 2,200 Å from the 2,000 Å response. The Lyman α detector is sensitive only between 1300 and 1050 Å. The energy in the Lyman α line is 94 percent of the radiant energy in the 1050 Å to 1300 Å band at unit optical depth. Of the 6-percent energy "leaking" around the Lyman α line, virtually all of it is due to solar emission and is absorbed by molecular oxygen in the same manner as the Lyman α energy, and therefore does not qualify as noise.

The noise contribution due to cosmic rays in the x-ray detector is at least ten times less than the signal level due to direct solar radiation. Additional signal processing of the pulses from the photon counter could enhance the effective signal-to-noise ratio because of the random nature of the noise pulses and the more or less uniform nature of the signal. It is doubtful if such a technique would be worthwhile when we are dealing with a relatively high signal-to-noise ratio in excess of 100.

5.2.7 Errors

The measurement of density at high altitude is subject to many inaccuracies. Those of greatest significance to the filter photometric technique are discussed here. When compared to current high-altitude density gages this technique promises to be very accurate.

5.2.7.1 Outgassing

A major advantage of the absorption technique for the measurement of density is that it is less vulnerable to error caused by outgassing. The error caused by the artificial atmosphere created around a rocket by outgassing and exhaust entrainment has troubled all experimenters. In the case of very large rockets that are venting fuel, staging, or still under power, the outgassing problems are compounded. The differential absorption technique largely avoids these problems, particularly at high altitudes where outgassing is the most severe.

The pressure at 160 km is roughly 0.038 torr. The total solar absorption is the sum of the absorption of each molecule between the measuring instrument and the sun. The number at 160 km, for example, can be estimated by multiplying the total number of molecules at the surface of the earth by the atmospheric pressure at 160 km in atmospheres, from Table II, namely:

$$\frac{76 \times 13.6}{29} \times 6.02 \times 10^{23} \times \frac{38 \times 10^{-6}}{760} = 1.08 \times 10^{20} \text{ molecules}$$

In order to affect the absorption data by 1 percent, 1.08×10^{18} molecules would have to appear as a contaminant between the sun and the sensor. Considering a 1 cm^2 aperture, 1.08×10^{18} molecules of air amounts to 3.6×10^{-5} standard cc. While this appears as a small amount of contamination, consider the fact that this is the amount per square centimeter.

The nose cone area of a rocket may amount to 5 m^2 which would have to evolve about 1.5 standard cc on the order of a response time, say 10^{-3} sec for a one percent error. Thus, to summarize, 1500 standard cc of contaminating gas would have to be evolved per second to affect the data 1 percent at an altitude of 160 km. This is an unlikely high amount. Thus, the absorption technique appears to offer a straightforward way to measure free air density.

5.2.7.2 Detector Drift

By proper aging of the detector, drift can be held to less than 1 percent per day after 24-hour warmup in the case of the photomultiplier. The ion chamber for Lyman α has negligible drift. The x-ray detector experiences drift in the order of 10 percent over several hours operation; however, during the flight the drift would be quite small.

5.2.7.3 Absolute Energy Calibration

The absolute energy calibration of the instrument will be carried out in the laboratory using gas discharge lamps and soft x-rays. At present, only an estimate can be made of the stability of this calibration on the basis of detector and electronics drift. By use of chopper stabilization and feedback, the electronics can be made essentially drift free. Thus, the only contribution to instability in absolute calibration would be the detector drifts mentioned earlier. On this basis, an overall system accuracy in reporting the absolute solar ultraviolet intensity would be ± 5 percent of the value for 50-percent signal output.

5.2.7.4 Atmospheric Dust

Recently high-altitude laser beam scattering research has suggested a thin, striated dust belt around the earth in the 80 to 150 km region. At present, the scattering from these particles cannot be evaluated without a more detailed knowledge of their size and density. As far as density measurements by ultraviolet absorption are concerned, the aberrations in the instrument calibration due to dust layers should be apparent upon reducing the data to the graphical form of intensity versus altitude. The dust bands would show up as steep variations in intensity. These then can be subtracted out from the smooth curve in the dust-free regions and both the dust density and the molecular oxygen density estimated.

5.2.8 Electronics

The support electronics for the assembly of detectors will be completely solid state and employ interchangeable modules for ease in servicing. Each detector will feed into an independent data system. This approach is simpler than switching the output of the detectors at the proper altitude and is more reliable, since the loss of one data system does not cause a complete failure. It is also believed that the additional data collected will be of help in planning possible modifications to future instruments. A block diagram of the electronic system is shown in Fig. 21.

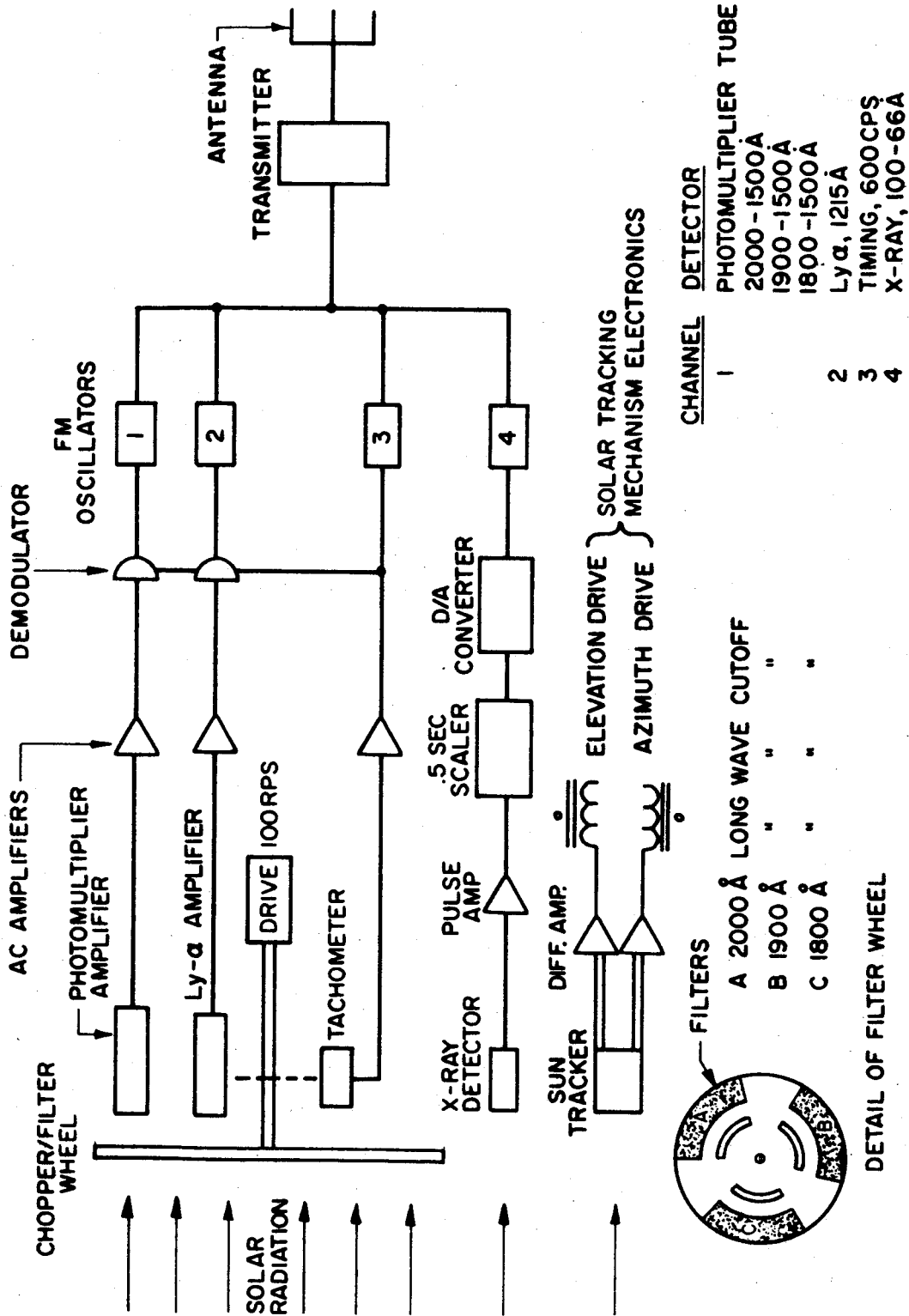


FIG. 21 PHOTOMETER DENSITY GAGE ELECTRONICS

The tachometer is used to provide a signal for synchronous demodulation and also to provide a timing pulse for data reduction. Both the photomultiplier (P-M) amplifier and Lyman α amplifier (Ly- α in Fig. 21) are ac-coupled with a large amount of feedback for stability. The P-M amplifier has a voltage gain of 100 and the Lyman α amplifier has a voltage gain of 10^4 . The input impedance of both amplifiers is taken as 10 megohms. The pulse amplifier used for the x-ray detector has a voltage gain of 1000 and an input impedance of 1 megohm. The capacity of the scaler need be no more than 10^4 counts, while the d-to-a converter need be only a simple integrating dc amplifier.

All the basic parts of signal processing electronics, up to the FM oscillators, have been developed and used on other instruments built by EOS. The FM oscillators and transmitter is a standard piece of flight instrumentation, such as Vector B56A subcarrier oscillators and Vector TRFT 250 transmitter.

The power supplier for the various electronic sections will have a common +28 volt dc feed voltage. The amplifiers all operate from a nominal 25.0 ± 1 volt line. This will be provided by a power conditioning regulator. Each channel will have its separate regulator to prevent cross modulation through power supply feedback. The high-voltage power supplies will be independent for each channel and operate from the $+25.0 \pm 1$ volt preregulated line.

5.2.9 Data Processing

The signals from the detectors will have the form shown in Fig. 22. After signal processing the form at the input of the FM oscillators is shown in Fig. 23. The structure of the photomultiplier signal is the same as shown in Fig. 22, except for the compressed time scale. The Lyman α detector output has been integrated, as has the scaled (0.5 sec) x-ray detector output. The photomultiplier channels can be separated on the ground by means of synchronous demodulation using the tachometer TM output as the demodulating signal. The bandwidth needed for the channels is shown in Table VIII.

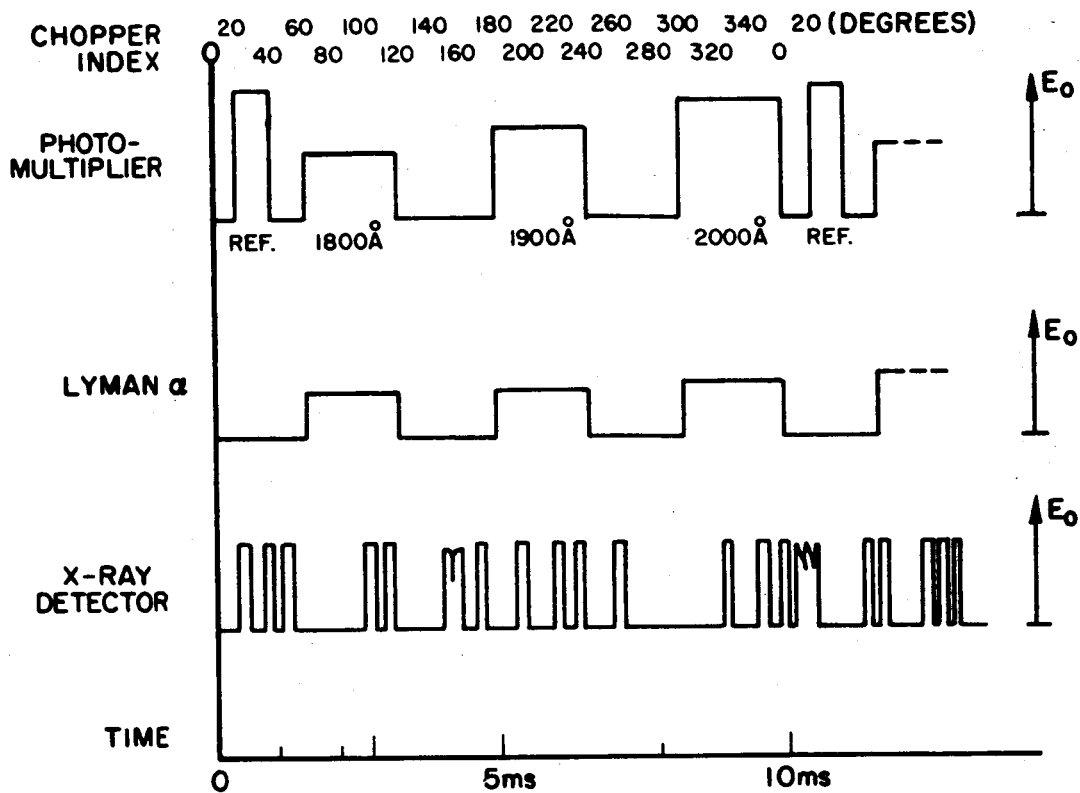


FIG. 22 TYPICAL DETECTOR OUTPUT

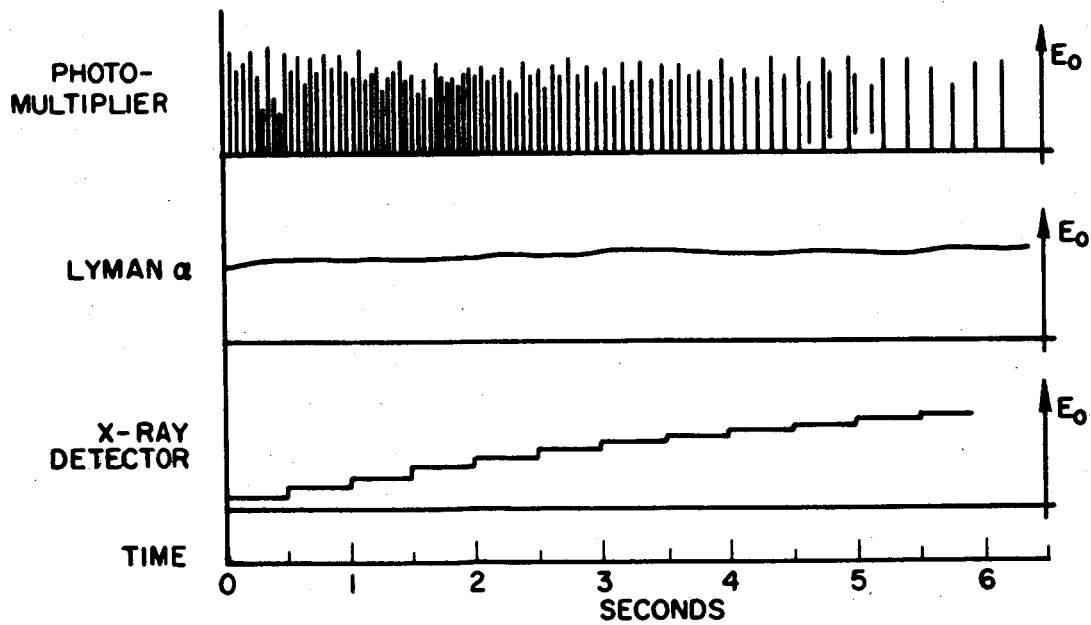


FIG. 23 SIGNAL INPUT TO FM OSCILLATORS

TABLE VIII
BANDWIDTH REQUIREMENTS

<u>Channel</u>	<u>Bandwidth</u>
Photomultiplier	900 cps
Lyman α	300 cps
X-ray detector	100 cps
Tachometer	300 cps

5.2.10 Instrument Calibration

The calibration of the instrument is to be carried out in the laboratory, using a carbon arc ultraviolet source and a vacuum ultraviolet spectrograph. The carbon arc will be differentially pumped in order to preserve the high vacuum needed in the spectrograph. The spectral response of the photometers will be determined for the photomultiplier and Lyman α detector.

The x-ray detectors will be calibrated against a standard ionization chamber using an x-ray tube as a source. The spectral response can be approximately determined by using filters on the x-ray tube and adjustments of the tube voltage.

Conversion of the photometer output will be made by normalizing the data for variations in spectral response and comparing the energy received with laboratory data on oxygen absorption cross sections. The absorption can then be converted into standard slant air mass by Lambert's law, cited in Section 5.2.2.

The problem of converting slant air mass into vertical air mass is treated in the appendix. It is suggested that a useful method of calibration would be to compare the density readings from the filterphotometer with those obtained simultaneously from an independent method. This other method could be the ultraviolet density gage discussed in Section 5.1 or the falling sphere technique discussed in Ref. 6, 16, and 26.

5.2.11 Instrument Configuration

In order to realize the full potential of the instrument, it must be orientated toward the sun. Since the flight path angle with the vertical varies from about 35 degrees at 40 km to 90 degrees at 150 km, a solar tracker must have this angular field of acquisition. A very simple x-y coordinate tracker developed by EOS, the Radiation Tracking Transducer (RTT), can perform the function of solar tracking using only pinhole optics. The instrument should be located in the nose tip or the first interstage of the launch vehicle, in order to have the best view of the sun at all times. The locations could be the same as shown for the ultraviolet density gage in Fig. 11. The instrument view port should be on the side of the vehicle that will face the sun during launch. The port is covered during the early part of the trajectory and is opened above 30 km.

The instrument and solar tracking mounting is depicted in Fig. 24. It consists of a fork-mounted detector and solar tracking sensor which is free to move through 60 degrees of elevation and 90 degrees of azimuth. The slit cut in the vehicle fairing must be wide enough to take in the 60 x 90 degree field of view. If the slit interferes with the aerodynamic performance of the missile, a lithium fluoride window may be used; however, the x-ray detector must be mounted such that its protective window can be removed when the detector begins operation.

The detector and sun sensor assembly is shown in Fig. 25. The x-ray detector is mounted in front of the chopper motor and has an unobstructed view of the sun. In the rear of the x-ray photon counter is the RTT sun tracker; the thin Glyptal window acts as a pinhole for forming a solar image on the RTT.

The chopper wheel contains filters in those openings which pass in front of the photomultiplier. A clear reference notch for data identification is also located in the chopper disk. As the wheel rotates, each filter in turn is placed in front of the photomultiplier, as well as a reference signal which may be identified by its

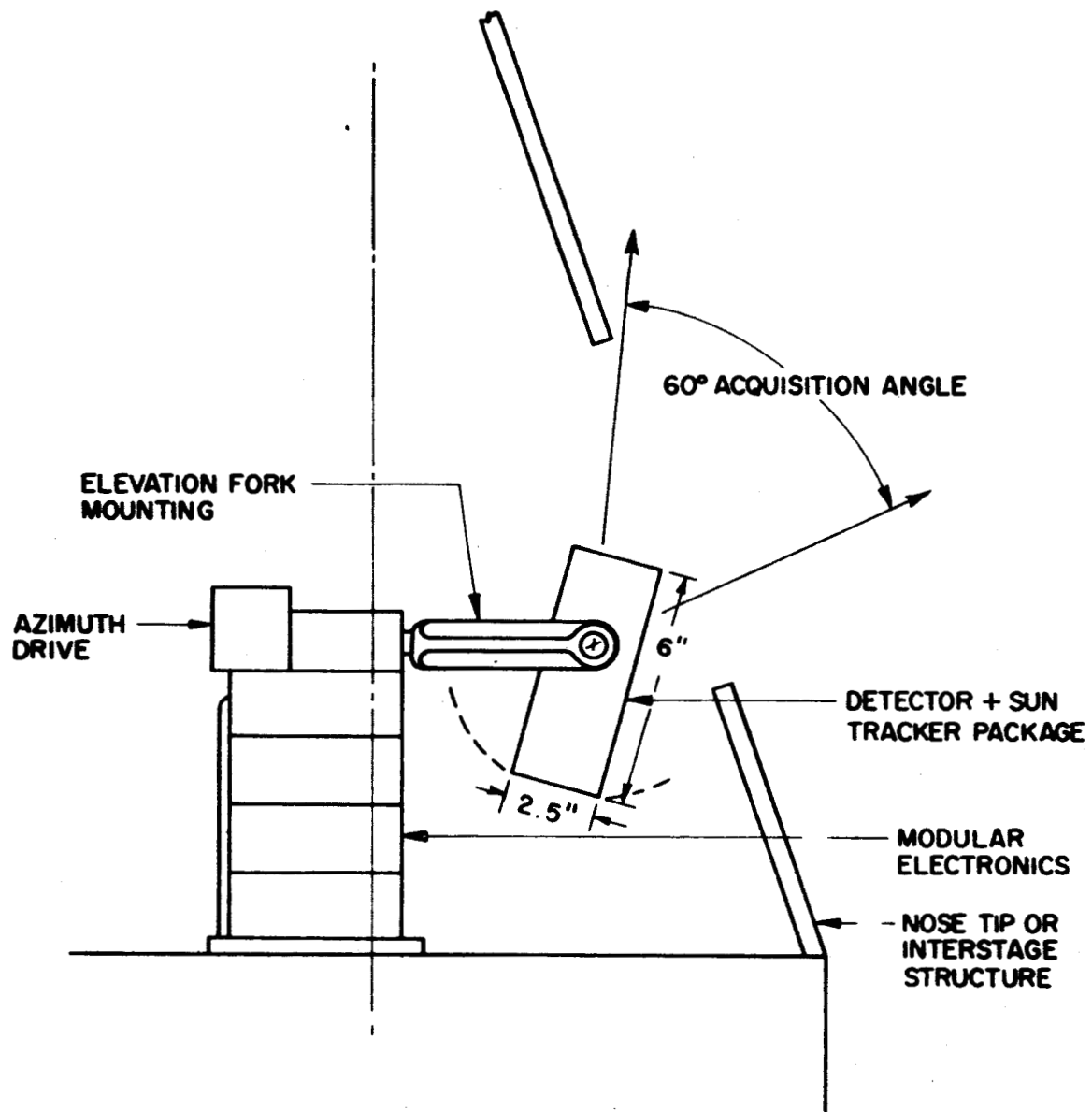


FIG. 24 INSTRUMENT AND SOLAR TRACKING MOUNTING

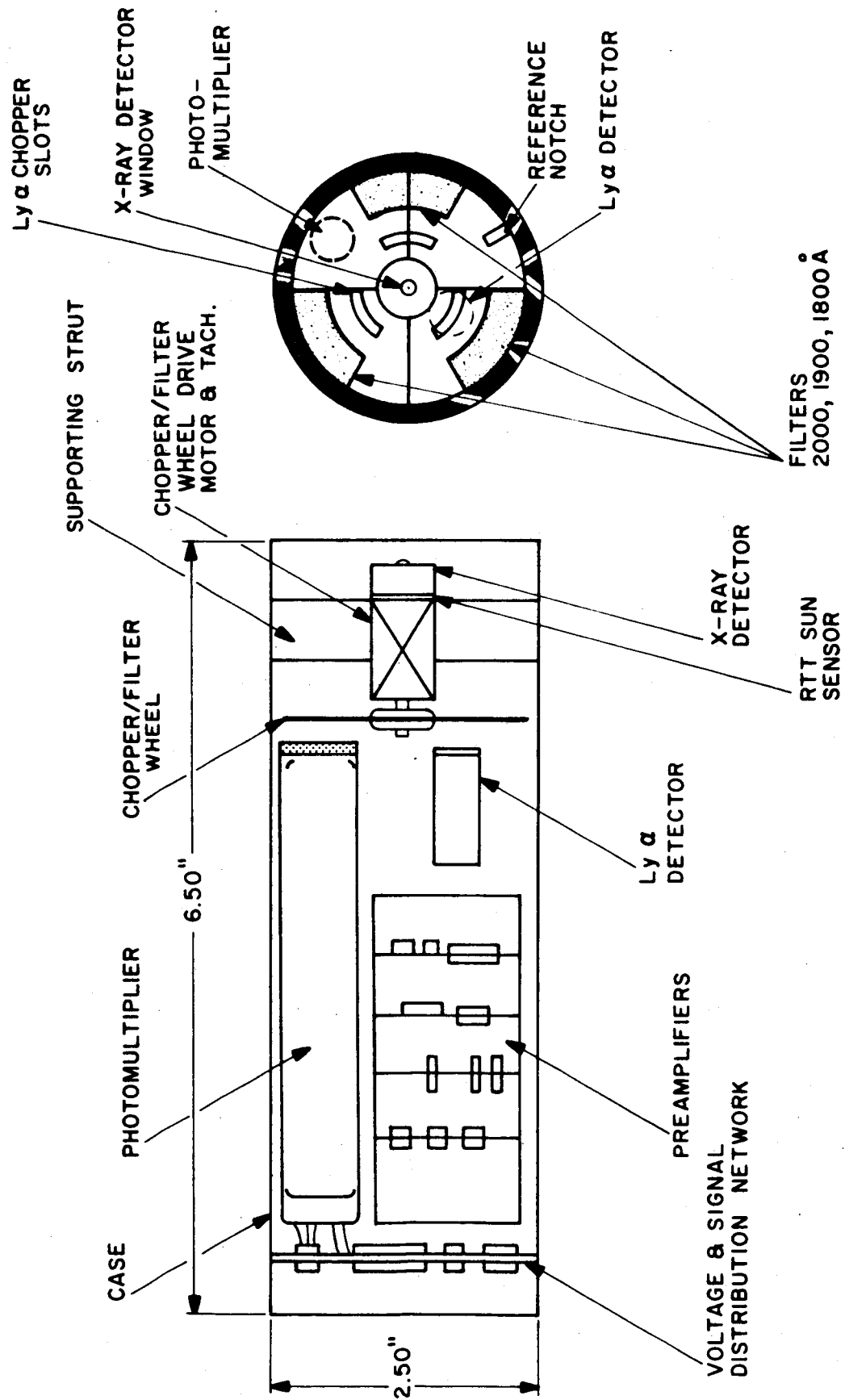


FIG. 25 DETECTOR AND SUN SENSOR ASSEMBLY

shorter duration. The Lyman α detector is also chopped at the same rate as the photomultiplier. As mentioned earlier, the amplifiers are high-stability ac-coupled in order to minimize zero drift due to the electronics. Also contained within the sensor assembly are the pre-amplifiers for each detector.

The estimated size of the detector package is 2.5 inches diameter by 6 1/2 inches long. Each moving part is statically balanced so that a couple acts on each axis of rotation during launch vehicle acceleration and, thus, no extra torque need be provided by the drive motors other than that necessary for positioning the instrument. Assuming a data acquisition time on the order of 100 sec, the elevation motor must drive at a rate of approximately $0.6^\circ/\text{sec}$, certainly a moderate figure and easily in reach of the simplest servo systems. The azimuth drive would drive through even a smaller angle during the flight. It is only necessary that the sun be in the open quadrant of the instrument compartment.

5.3 Electron Beam Density Gage

We were led to consider an electron beam densitometer initially by the requirement of a penetration distance of 10 to 20 meters. If this penetration could be achieved, it would be possible to locate the instrument in the uppermost interstage section of a launch vehicle.

Particle backscatter techniques using alpha, beta, or gamma sources were first investigated. They were unsatisfactory because in order to get a sufficiently high count rate for accurate measurement at high altitudes where the density is low, too large a radioactive source was required. Put another way, the effective backscatter cross section was too low.

A higher effective backscatter cross section could be obtained with an electron beam as the illuminator. Since electron guns are readily available, this method was studied next. The geometry of the device is similar to that of the ultraviolet density gage portrayed in Fig. 26. The source of the electron beam is an electron gun and the

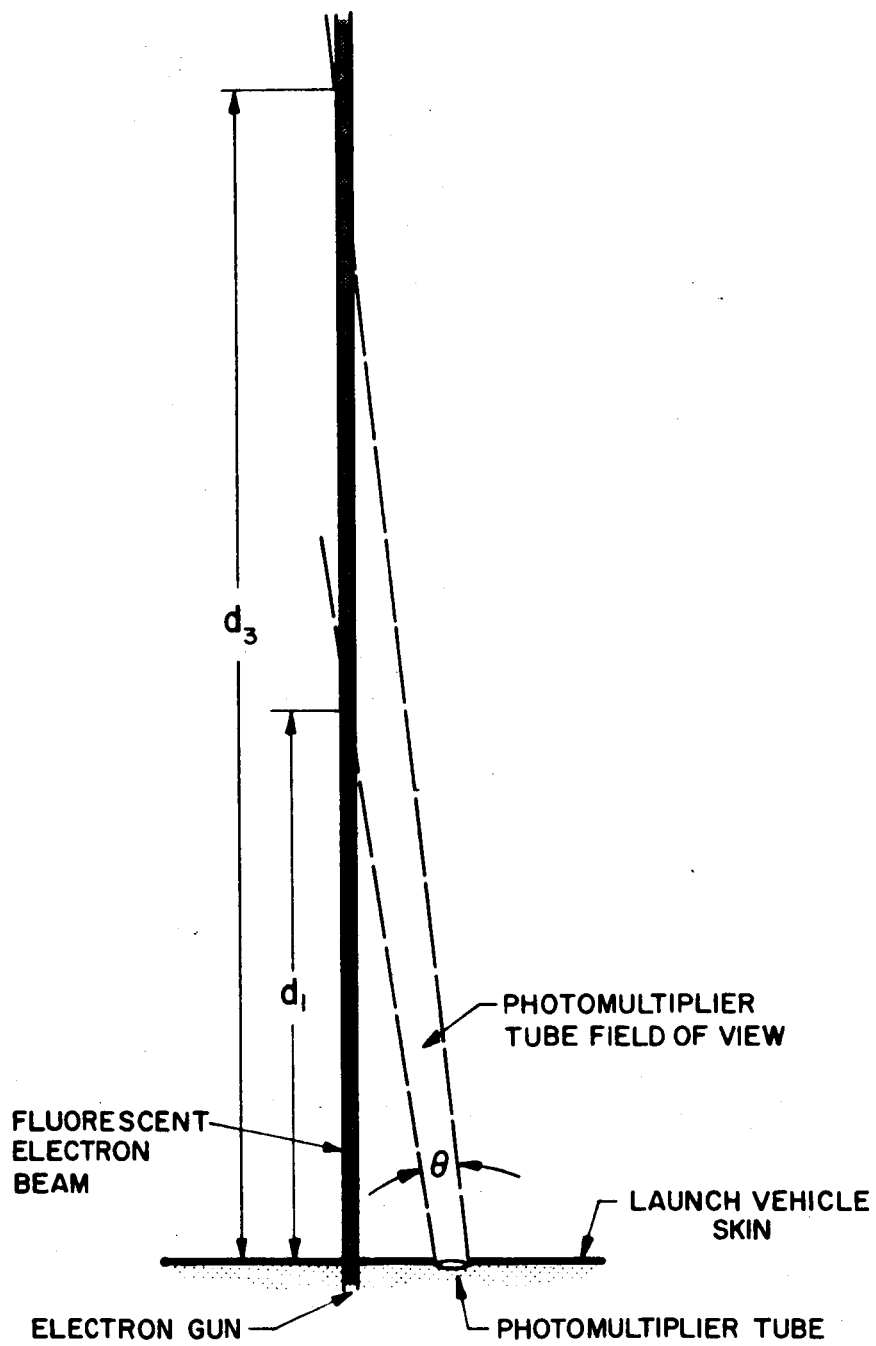


FIG. 26 ELECTRON BEAM DENSITOMETER GEOMETRY

detector is a photomultiplier tube which senses the fluorescence of the air. The field of view of the detector intersects the electron beam between d_1 and d_3 .

Although initially the electron beam densitometer appeared very promising, our ultimate conclusion is that the electron beam technique is not practicable below an altitude of 75 km. Its ceiling is about 130 km. The reasons are that at the lower altitudes the divergence of the beam is too great, and that the gun must be operated in a vacuum that requires bulky differential pumping machinery. The balance of this section discusses our analysis that led to this conclusion.

5.3.1 Penetration Distance

The important consideration in whether or not the beam can reach the regions of undisturbed flow beyond the shock layer is the distance to which the beam can penetrate the air. For a given level of beam energy this distance is inversely proportional to the air density, as is illustrated in Fig. 27. The distance also is directly proportional to the accelerating potential. As the figure shows, in order to achieve any reasonable penetration range the accelerating potential or beam energy must be at least 10 kev. Beam dispersion due to multiple scattering of the electrons, which is discussed in Section 5.3.4 is neglected here.

5.3.2 Signal Strength

Inasmuch as lack of signal strength at the higher altitudes has caused the other backscatter techniques to be unsatisfactory, we first investigated the signal strength at 100 km.

The amount of light in watts/cm of electron path length that is isotropically emitted by the ionized air through which the electron beam passes is given by

$$I = KN \left(\frac{dE}{dx} \right) \frac{\rho}{1 + 5.49 \times 10^4 \rho} \text{ watts/cm} \quad (34)$$

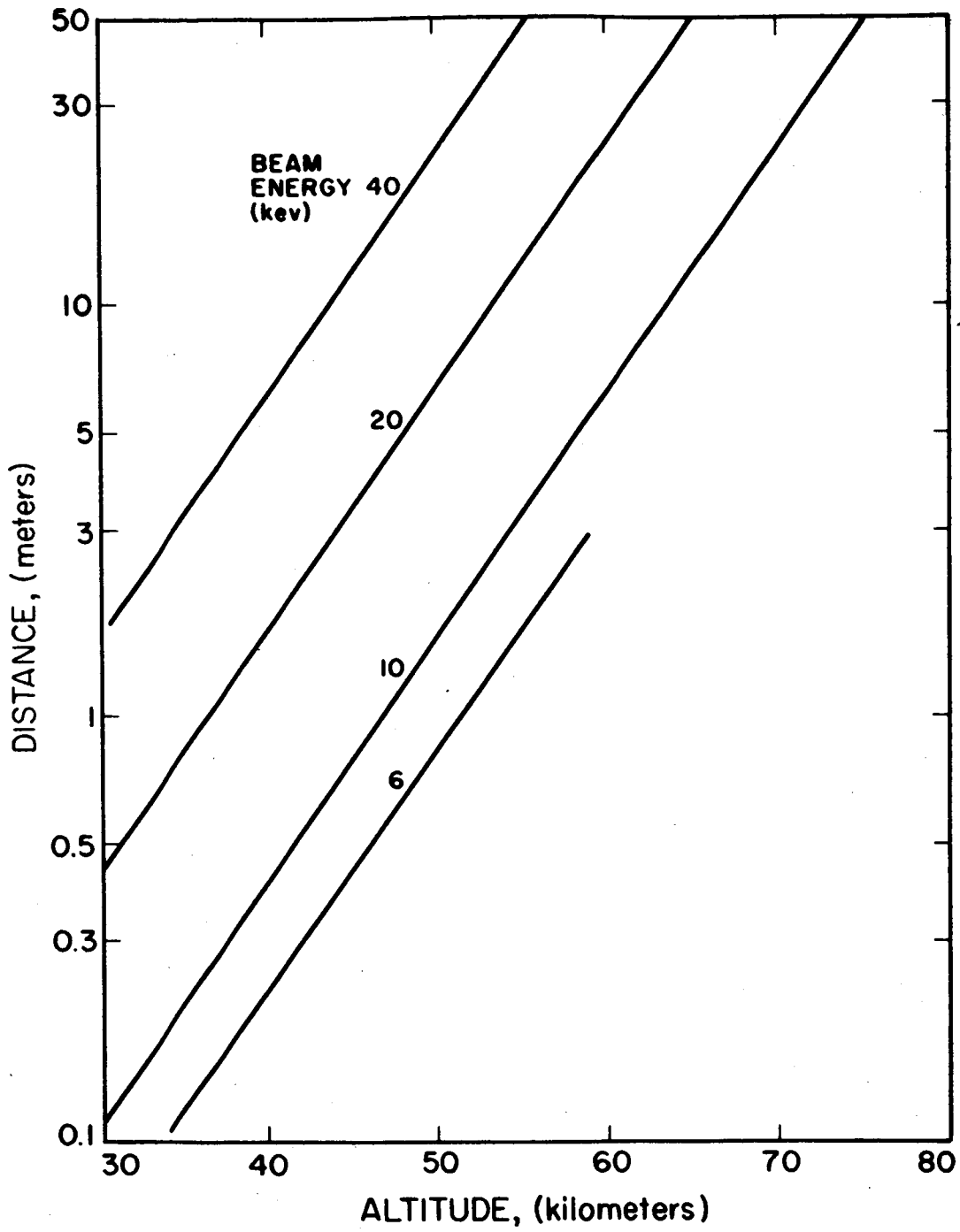


FIG. 27 PENETRATION RANGE OF ELECTRON BEAM

where ρ is the air density in gm/cm^3 ; dE/dx is the energy lost per electron per centimeter in $\text{joules - cm}^2/\text{gm}$; N is the number of electrons per second; and K is the fraction of energy lost that goes into light.

The amount of light emitted by the fluorescing air and actually received by a photomultiplier tube is represented by the relation

$$I_r = fI \quad (35)$$

where f is the fraction of the light emitted by the gas that is collected by the photocathode of the photomultiplier tube.

The amount of light that would be received by a 1.5 cm^2 photocathode at an altitude of 100 km was calculated. It was assumed that the light was emitted by a 1-centimeter long column of air located 10 meters from the photomultiplier. The following values were assigned to the terms of Eqs. 34 and 35.

$$\begin{aligned} \rho &= 6 \times 10^{-10} \text{ gr/cm}^3 \\ K &= 0.1 \\ N &= 2 \times 10^{17} \text{ electrons/sec} \\ &\quad (\text{or, } 32 \times 10^{-3} \text{ amp}) \\ dE/dx &= 9.6 \times 10^{-13} \text{ joules-cm}^2/\text{gm} \\ f &= 8 \times 10^{-8} \end{aligned}$$

The amount of light that would be received by the photocathode under these conditions is 10^{-12} watts/cm of path length. If the field of view of the photocathode encompassed a 1-meter long column rather than a 1-centimeter column, at 10 meters range, the amount of light received would increase to 10^{-10} watts.

5.3.3 Background

5.3.3.1 Photomultiplier Tube Noise

A 1P28 photomultiplier tube has an equivalent noise power at the photocathode, when measured through a 100 cps bandpass

filter, of approximately 10^{-10} watts. Since this is the same order as the signal received from a 1-meter long column of ionized air, the electron beam must be modulated to detect the signal at high altitudes.

5.3.3.2 Light from the Day Sky

If we exclude the quadrant of the sky that actually includes the sun, it is indicated that the incident radiation in the visible wavelengths at 100 km is about 10^{-4} watts/cm²-steradians (Ref. 15). Considering a detection apparatus with an aperture of 10^{-6} steradians, the background signal would be 10^{-10} watt/cm². This again is of the order of the signal, and modulation must be used. Thus, there appears to be an adequate signal if modulation techniques are used.

5.3.4 Scattering

The main problem associated with producing a collimated electron beam is the multiple scattering of the electrons by the air molecules. The projected mean angle through which the beam would be scattered by the air molecules is given by

$$\bar{\theta} = \frac{15}{P} \sqrt{\frac{L}{L_R}} \text{ radians} \quad (36)$$

where P is the momentum of the electrons in Mev, L the path length in gm/cm², and L_R is the radiation length of the gas also in gm/cm².

The scattering is most serious at the lower altitudes so the magnitude of the scattering angle was calculated for an altitude of 30 km. We find for a penetration distance of 10 meters through air of 10^{-5} gm/cm³ density (30 km) that the mean scattering angle for 0.15 Mev electrons is 2.6 radians. In other words, the electrons do not form a beam, they diffuse.

Rewriting Eq. 36 to put in the dependence of range on momentum, the equation becomes

$$\bar{\theta} = \frac{2.44(\ell\rho)^{0.2}}{L_R} \quad (37)$$

where l is the penetration distance or range in centimeters and ρ is the gas density in gm/cm^3 . For a given range the projected mean scattering angle goes as the fifth root of the density. This means that even at an altitude of 75 km, where the density has decreased from 10^{-5} to 10^{-8} gm/cm^3 , the scattering angle is about seven-tenths of a radian (40 degrees) and the electrons would not form a well-defined beam. If a higher beam energy were used, the beams would be better defined.

5.3.5 Effect of Electron Beam Energy

To confirm the findings of the preceding analysis, a second analysis was undertaken concurrently. The other analysis approaches the problem from a somewhat different angle as is apparent from a comparison of Eqs. 36 and 37 with Eqs. 38 and 39.

The scattering mechanism considered is the interaction of the electrons with the Coulomb field of a nucleus. It is assumed that the scattering angles are small and that the net angle of deflection, θ , has a gaussian distribution about $\theta = 0$. It is also assumed that the electron beam extends well beyond the portion being considered.

Under these assumptions, the mean square of the linear deviation normal to the direction of the incident electron beam, i.e., the radius of the dispersed beam, can be expressed as

$$\bar{r}^2 = \frac{1}{3} \bar{\theta}^2 L^2 \quad (38)$$

where \bar{r}^2 = mean square of the dispersion radius
 $\bar{\theta}^2$ = mean square of the net angle of deflection
 L = distance to beam element being viewed

The net angle of deflection can be expressed as

$$\bar{\theta}^2 = \frac{8\pi n L z^2 Z^2 e^4}{(PV)^2} \ln \left(\frac{a_o PV}{2Z^{4/3} z^2} \right) \quad (39)$$

where z = charge of incident particles
 Z = charge of scattering nucleus
 n = number of atoms per cm^3

V = velocity of incident particles
 P = relativistic momentum of incident particle
 a_o = Bohr radius = 5.29×10^{-9} cm
 e = electron charge

Since we are considering an incident beam of electron particles passing through air, the mean square of the linear deviation in centimeters squared can be evaluated as follows:

$$\bar{r}^2 = 9.12 \times 10^{-18} \left[\frac{0.27 + \ln(PV)}{(PV)^2} \right] NL^3 \quad (40)$$

where $z = 1$

Z = average atomic number of air = 7.27
 a_o = 5.29×10^{-9} cm
 e = 4.8×10^{-10} esu

Using Eq. 40 the effect of beam kinetic energy ($P \times V$) on beam radius was calculated. A higher beam energy will reduce beam divergence. Beam energy levels of 100 and 200 kev were investigated at a range of altitudes from 30 to 100 km. An energy of 200 kev is the highest practical energy that could be used. Our findings are plotted in Fig. 28. The maximum penetration distance for an electron beam of given energy at each altitude also is shown in the figure.

In interpreting these plots, it must be remembered that the equations actually are valid only for the case where the beam length is much greater than the distance to the element being viewed, where ($P \times V$) is approximately constant. It is immediately seen that at the lower altitudes the distance from the beam source to the element being viewed actually is about equal to the total beam length and this requirement is not met. However, we believe that this analysis gives a useful first cut picture of the situation.

Qualitatively it is seen that for the case where the detector must look out several meters to get beyond the shock layer the electron beam technique will be reasonably effective at an altitude of

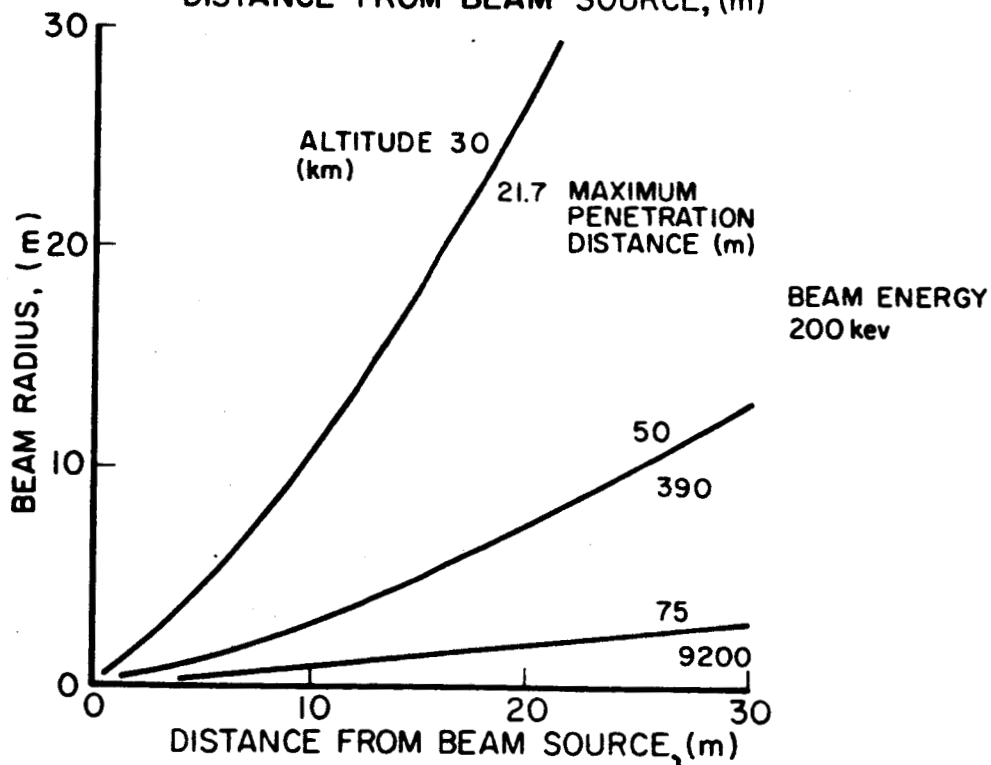
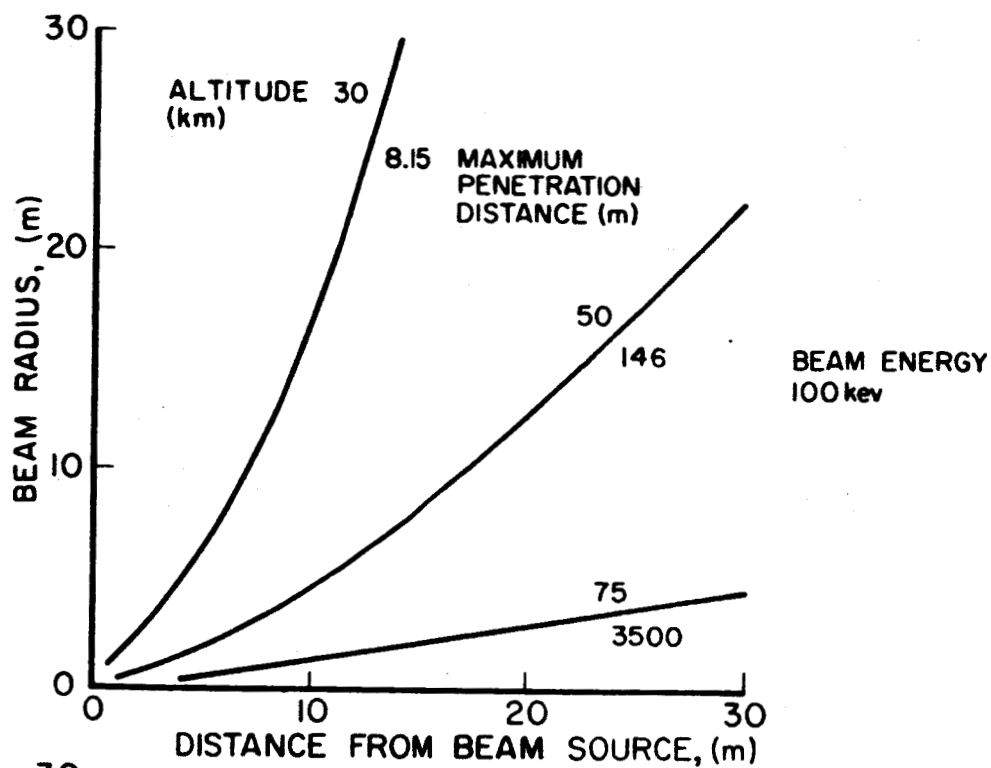


FIG. 28 RADIUS OF ELECTRON BEAM

75 km and above. At 30 km the technique has a reasonable beam dispersion radius of less than 1 meter only for look distances of 1 meter or less.

5.3.6 Electron Gun

Beam scattering could be avoided if the instrument were placed on the nose tip. Here a penetration range of only a few centimeters is required, and the scattering at this short range would be only a fraction of that at 10 meters. However, study of electron gun technology revealed that the gun itself would cause further difficulties.

For an electron gun to operate, it must be in a vacuum where the density is less than 10^{-7} gm/cm³. At higher densities, the filament suffers severe contamination. To achieve this, a differential pumping technique must be used wherein the gun filament is located within a series of chambers that are at progressively lower densities. To achieve the required density drop when the vehicle is flying through air having a density equivalent to that found at 30 to 50 km, the vacuum unit alone must be a cube about one-half meter on a side. Such a bulky instrument would be impractical for mounting on the nose tip.

5.3.7 Conclusions

In summary, we have found that at the lower altitudes an electron beam density gage cannot be located in the forward inter-stage because the penetration scattering is so severe that the beam cannot reach beyond the shock layer. It cannot be located in the nose tip, where the required penetration distance is short, because a bulky vacuum system must be carried. Thus, it appears that an electron beam device is usable only from about 75 km up to 130 km.

5.4 Backscatter Density Gage

Another method of avoiding the disturbed flow field near the launch vehicle is to use the backscatter of nuclear radiations to measure

density. The radiation coming from a nuclear source propagates through the medium to be measured and interacts in a manner which causes some of the radiation to scatter back to a detector. The amount of interaction or scattering is primarily a function of the density of the scattering medium, in our case air, and thus, the amount of radiation detected is a good measure of the density of the air.

Commonly beta particles or gamma radiations are utilized as the backscattered agent. Beta particles are electrons which have been ejected from a nucleus. As these beta particles or electrons pass through the air, they are scattered as a result of their interaction with the electric fields of the nucleus and orbital electrons. Gamma radiation is electromagnetic radiation of short wavelength emitted by nuclei in the course of radioactive decay. Scattering of gamma radiation by a medium is the result of interaction between the incident radiation and the electrons of the medium. The Rutherford law of single scattering in the case of betas and the Thompson theory (concerning the fraction of radiation scattered by an electron) in the case of gammas can be related to the density of the air. When the resulting relation is integrated over the thickness of the air layer and the angle of deflection, the air density as a function of the amount of radiation received by the detector can be determined. Absorption and multiple scattering are assumed to be negligible.

Density has been measured in the past with low-energy beta particles up to an altitude of about 18 km, where the count rate was about 300 per second. The point where the particles are backscattered, and consequently at which the density measurement is made, is calculated to be roughly 1 cm out from the instrument. The source used was 4 mC Pm^{147} . In order to obtain the same count rate at 70 km altitude the radiation source would have to be 10^5 times as intense, or a 400 curie source. A source of this strength is, of course, too difficult to handle in the present application. At 70 km the effective range would

still be about 1 centimeter. The reason for this small range is that the events decrease going away from the source by the reciprocal of the square of the range, as does the solid angle back to the detector. However, the amount of air causing the scattering increases as the range so that the effective penetration of the system as a density measuring instrument actually falls off as (range)⁻³, and the effective range is estimated to be about one centimeter.

Figure 29 is a graph of count rate versus density and altitude for two source intensities, one 4 millicurie and the other 40 millicuries. To show the extremes of count rate that might be encountered, data are presented for the free air density and the stagnation density. If the backscatter occurred in the free air the solid curve would apply. If the backscatter instrument were placed inside a pitot tube the dashed curve would apply.

The smallest count rate that can be monitored and still give the desired resolution in an operational situation is deemed to be 100 per second. Thus, this technique appears to be limited to altitudes below 45 to 65 km.

An alpha source will yield a backscatter count rate 1.48 times those shown in Fig. 29. With this source the maximum altitude would be increased to from 57 to 90 km.

To verify the results of this general analysis another analysis was made of a specific gamma ray device being developed under the sponsorship of NASA, Langley Field. It is discussed in Ref. 39.

In order to achieve sufficient statistical accuracy with a backscatter device the total counts must exceed the quantity:

$$\left[\frac{C_o}{C_h - C_o} \right]^2$$

where C_o = count rate at zero density

C_h = count rate at altitude

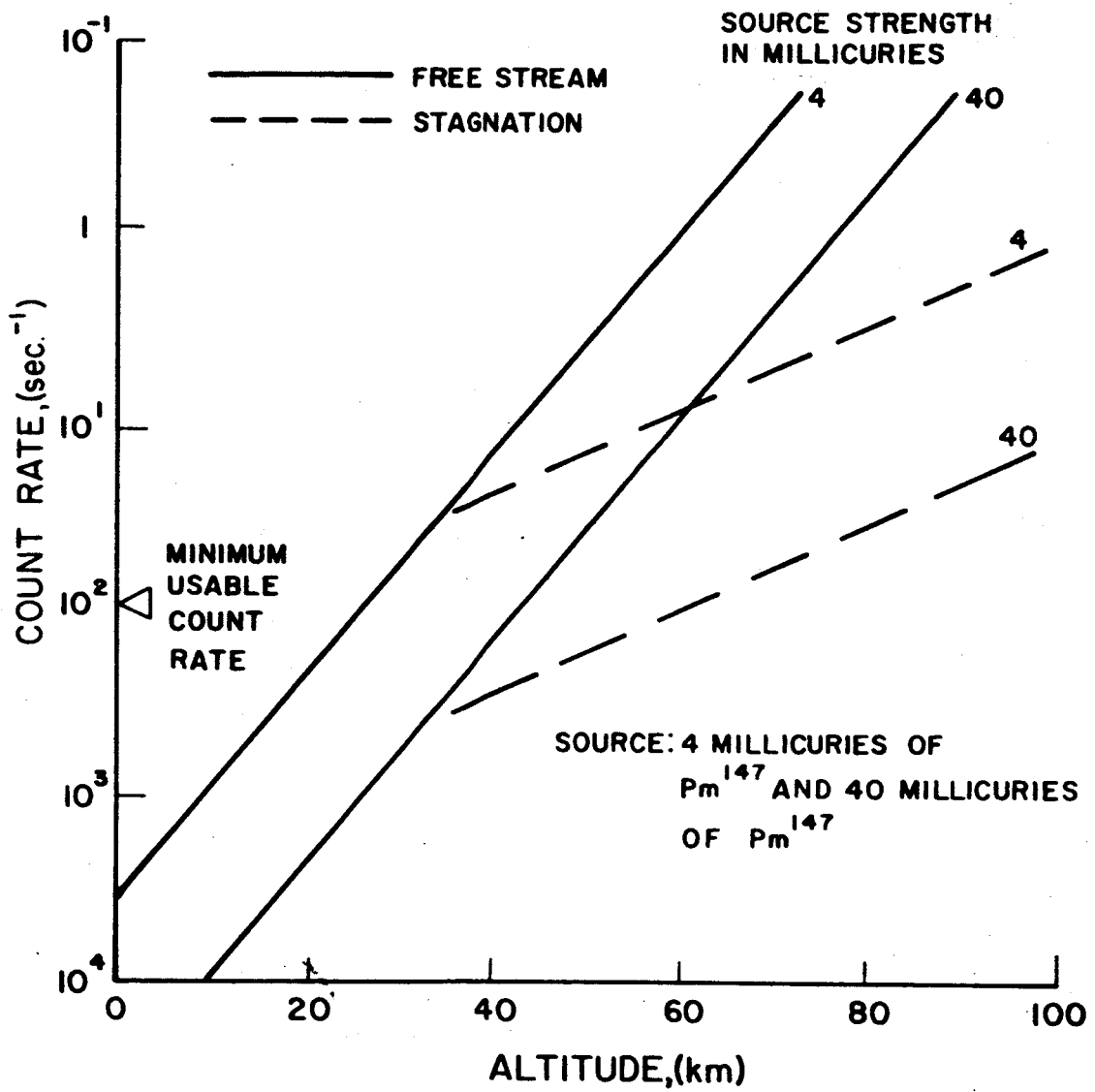


FIG. 29 BACKSCATTER COUNT RATE

The residual count rate at zero density was reported to be 50,000 cpm. According to data presented in Ref. 39, at an altitude of 30 km, the count rate would be 51,200 cpm; therefore, to achieve statistical accuracy the total number of counts must exceed 1600 and the counting duration must be 1.8 sec. During this interval a launch vehicle would rise around two kilometers. At an altitude of 40 km the minimum number of counts must be 2×10^4 , which requires a 24-second counting duration. This would give an average density over an altitude interval of 32 km. Such gross resolution would not be satisfactory. In this case the ceiling appears to be 30 to 40 km. Our conclusion is that backscatter techniques that employ a radioactive source are not applicable to the altitude regime under consideration, and that techniques that exploit larger backscatter cross sections are required for these altitudes.

5.5 X-Ray Density Gage

A larger backscatter cross section can be obtained by using an x-ray source rather than a beta or gamma source. Consequently, the x-ray air density gage which is being developed by NASA-Langley was investigated. Mr. Henry G. Reichle, Jr., Cognizant Engineer, IRD Instrument Physics Research Section, was contacted. He advised us that this device is being developed for use aboard an entry vehicle. It relies on the large angle Compton-scattering of low energy x-rays. For the initial test they are using a 40 to 50 curie radioisotope source, and in the future they will shift to an x-ray tube. The penetration distance is 1 to 1.5 feet.

It is the opinion of Mr. Reichle that in its present form, the instrument is not suitable for the current application. This is in line with our experience when studying backscatter techniques that if a penetration distance great enough to reach outside the shock layer is required they all lack sufficient altitude capability. However, the development of backscatter techniques should be followed carefully, for in general they possess the qualities of accuracy and compactness.

5.6 Ionization Gage

In the continuum flow region density is not usually measured. The gages are calibrated in terms of pressure and density is calculated. In the slip and free molecule regime density is measured directly by one of the ionization gages listed in the Pressure Transducers sheet of the table in Section 4. Actually these gages can be calibrated either in pressure or density.

Ambient density could be measured by means of static pressure ports located in a cylindrical probe or pitot tube as depicted in Fig. 30. The exact distance of the ports from the probe tip is determined by careful wind tunnel tests to find the point on the probe where the surface pressure/density has relaxed to the ambient pressure/density. An alternative location, and one that avoids the problem of a heated boundary layer, is to locate an ionization gage calibrated in terms of density behind the impact pressure port of Fig. 30. This location takes advantage of the ram effect and allows a given gage to be used to higher altitudes.

There is no point in going into the design details of density ionization gages here. They have been extensively used aboard aeronomical rockets and widely reported in the literature the reader is referred to (Refs. 13, 40, and 41)

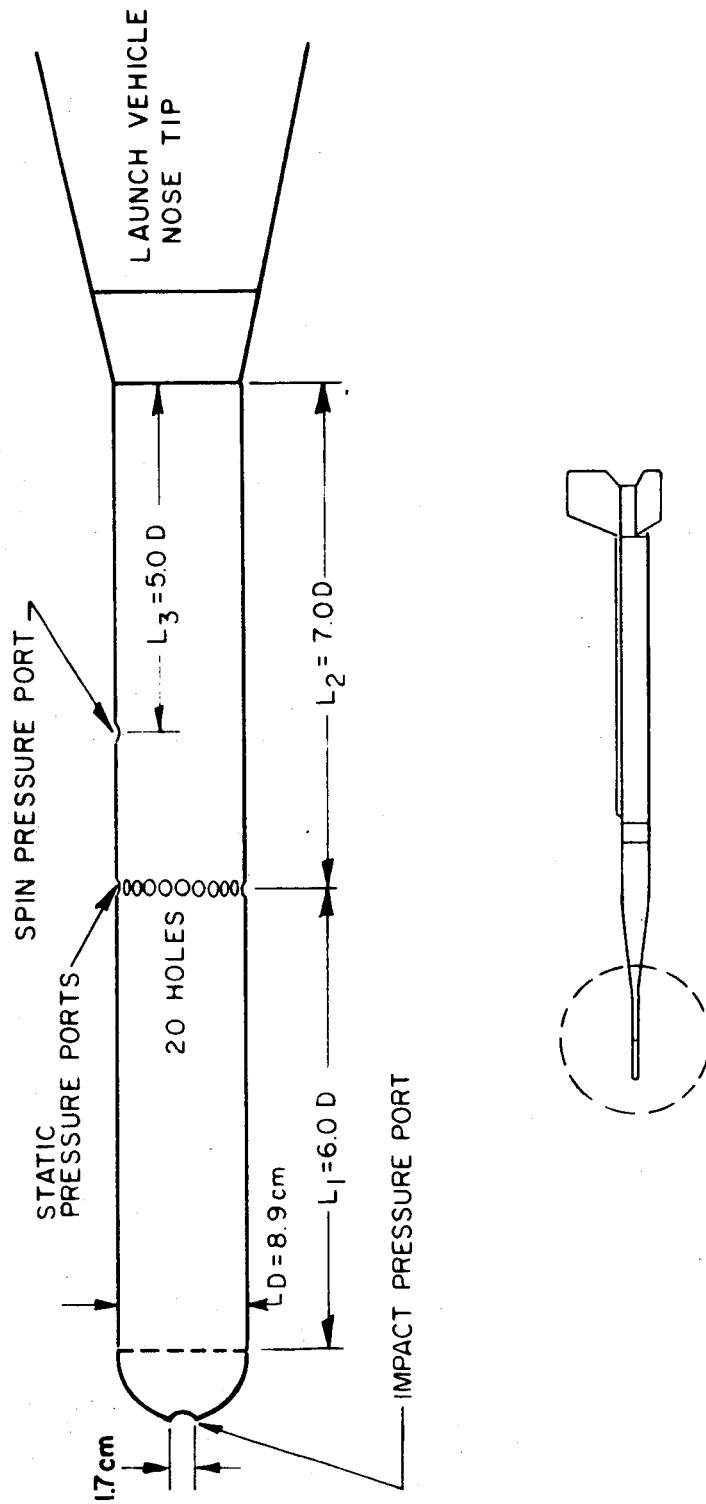


FIG. 30 CONFIGURATION OF A PITOT-STATIC TUBE

6. PRESSURE

There appears to be no practicable device or technique which can measure the pressure of the atmosphere at a remote point.

The best method to determine the pressure of the free atmosphere directly is deemed to calculate it from a measurement of the density profile or to measure it directly with a pitot static tube mounted on the nose tip.

6.1 Pitot-Static Probe

The pitot-static instruments have been used in several forms to secure data in the mesosphere and thermosphere. The configuration can be a cone such as discussed by La Gow, et al, in Ref. 42 or a cylinder such as discussed by Ainsworth, et al., in Ref. 23. There has been some controversy whether a conventional pitot-static device would be accurate in slip and free molecule flow. Recent extensions by Liu of his original work on an approximate theory (Ref. 43 and 44) have increased confidence in the use of the pitot-static probe at free molecule flow altitudes.

There is no need to go into detail on the principle of operation of pitot tube here. For details the reader is referred to Ref. 23 for cylindrical pitot tubes and to Refs. 9 and 45 for cones. The cylindrical configuration similar to the one depicted in Fig. 30 is most commonly used and this type is recommended.

Both diaphragm and ionization gages have been used with pitot-static tubes to measure pressure. Ionization gages, such as the Alphatron which employs a radioactive source, are capable of precise measurements between 30 and 100 km. However, the type of ionization gage best suited to this interval (Ref. 9) are very sensitive to the chemical composition of the air. Outgassing, upper stage fuel tank

venting or exhaust plume entrainment could contaminate the air and require the use of a mass spectrometer to determine the molecular weight of the air. On the other hand, diaphragm gages are insensitive to the chemical composition of the gas being measured. Two or three separate diaphragm gages would be required in order to get the desired response over the dynamic range that would be encountered. Diaphragm gages are the more widely used and are recommended for this application.

The Range Development Support Directorate at the Pacific Missile Range currently is sponsoring the development of a pitot-static tube for use aboard the boosted Arcas to about 110 km. J. Masterson of PMR has indicated in private communications with the author that the pitot tube is of conventional supersonic design and uses diaphragm-type pressure sensors. This development program should be watched with interest, because this device would be directly applicable to the present case.

6.2 Hypsometer

For the altitudes below 60 km, pressure best can be measured with a descent-type hypsometer. Hypsometers have been used for years with balloons and recently Bendix has reported success with a version for use with the AN/DMQ-6 rocketsonde and the Arcas sounding rocket. This device is discussed in Ref. 6.

The hypsometer is a widely known device and therefore it is not necessary to discuss it in detail here. It operates on the basis that the temperature of a boiling liquid, such as Safrole, is dependent upon the pressure on the surface of the liquid. The relation between the boiling point and the pressure is given by the Clapeyron-Clausius equation:

$$\frac{d \ln P}{d T} = \frac{\Lambda}{R_G^2}$$

The pressure measurement becomes increasingly accurate with altitude and the temperature measurement is readily compatible with standard radiosonde transmitters and receivers.

Reference 6 quotes estimates of error by the manufacturer as ± 5 percent at an altitude of 60 km or so and ± 1 percent at 45 km. Problem areas are the necessity of carefully controlling the amount of heat added to boil the liquid as it descends, to prevent superheating the liquid, and the proper venting of the sensor as the parachute oscillates. The first hypsometer flights were made in 1962 and the device appeared to survive the launch and deployment accelerations and to function satisfactorily. For more information, the reader is referred also to Ref. 4.

Thus, the descent hypsometer appears to be satisfactory for use aboard a large launch vehicle if dropsonde-type instrumentation is contemplated.

6.3 Risesonde

A technique that appears to have considerable promise is one wherein an instrument package is jettisoned from the vehicle and rises with it. The package would have sufficient momentum that it would rise roughly parallel to the flight path of the launch vehicle for some distance before falling back. If a number of these risesondes were jettisoned along the flight path a rather complete picture of the nearby atmosphere could be obtained. On the other hand, dropping a single instrument as is usually done would provide a sounding which, except for the first kilometer, is a considerable distance from the actual flight path.

The risesonde for the region above 85 km could be similar to the one developed by the University of Michigan and described in Ref. 46.

The University currently is testing a dropsonde which is cylindrical, 6 inches in diameter and about 2 feet long. It weighs 20 to 35 pounds and contains instruments such as an ionization gage, an

omegatron, and a plasma probe. The cost is around \$30,000: \$10,000 each for hardware, electronics, and labor. They have had three successful flights recently.

The pressure sensor is a WX-4520 Bayard-Alpert ionization gage. It is a small ruggedized gage especially designed for rocket and satellite use. A fluctuating pressure is provided by spinning the package so the pressure gage is alternately exposed to stagnation pressure and base pressure. Free air ambient pressure is the pressure measured 90 degrees from the peak (stagnation) pressure. A second pressure gage is located 90 degrees from the first to determine the attitude of the sensor package. A transistorized multirange electrometer amplifier and a Vector TRPT-250-R, 1/3 watt, all transistorized FM-FM telemetry transmitter also are proposed for the payload package. Free stream density is calculated from the expression

$$\rho_{\infty} = \frac{\Delta p_i}{U_i \sqrt{\pi} \vec{w} \cdot \vec{x}}$$

where \vec{x} is the unit vector normal to the plane of the orifice and Δp_i is the change in measured pressure due to package rotation.

The one fatal drawback with this technique in the present instance is that an unstabilized instrument can be used only in free molecule flow. This limits its usefulness to altitudes above 85 km. In the altitude interval between 30 and 85 km the package would have to be stabilized so the sensor ports would be at a known and constant angle of attack. This requirement would necessitate a much too complex and expensive package.

Thus, the risesonde concept appears to be inapplicable to the altitude range under consideration.

6.4 Radioactive Gas Puffs

One technique that was investigated briefly was to eject puffs of radioactive gas into the free stream ahead of the vehicle nose tip. The pressure and density the gas cloud would accommodate itself

to the pressure of the free air. Monitors could be located aft on the vehicle to measure the concentration of the radioactive cloud after it had come into equilibrium with the atmosphere. The concentration of the cloud would be a measure of the pressure. This technique was deemed unfeasible, however, because of uncertainty of the accommodation characteristics of the gas cloud and the high level of radio activity that would be required.

6.5 Calculation

As is discussed in Section 7.5 temperature can be calculated from a density profile by means of the following expression:

$$T_2 = \frac{\rho_1 \bar{M}_2}{\rho_2 \bar{M}_1} T_1 - \frac{\bar{M}_1}{\rho_1 R} \int_{h_1}^{h_2} \rho g dh \quad (41)$$

Pressure then can be calculated from the temperature profile by means of the perfect gas law.

$$P = \frac{\rho RT}{M} \quad (42)$$

Above 90 km the mean molecular weight no longer is constant and the significant parameter becomes the molecular scale temperature which is defined as $T_M = T(\bar{M}_0/\bar{M})$. (Ref. 1). In this interval the molecular scale temperature can be calculated from the density by means of the following expressions (Ref. 5).

$$\frac{d \ln \rho}{dH} = \frac{-1}{T_M} \left[F + \frac{dT_M}{dH} \right] \quad (43)$$

$$\frac{d^2 \ln \rho}{dH^2} = \frac{1}{T_M^2} \frac{dT_M}{dH} \left[F + \frac{dT_M}{dH} \right] - \frac{1}{T_M} \frac{d^2 T_M}{dH^2} \quad (44)$$

where $H = \frac{RT}{\bar{M}g}$ (45)

Neither of these equations can be solved explicitly for T_m or dT_m/dH and numerical methods, such as those described on p. 11 of Ref. 5, must be employed. Pressure can be calculated from the following expression and its derivative:

$$\frac{d \ln P}{d H} = - \frac{F}{T_M} \quad (46)$$

To carry out the calculation the equation is integrated upward from the reference level at 30 km with a known initial value of pressure. It will be necessary to obtain an initial value of P_0 at 30 km from overlapping radiosonde data, or, lacking this, from the best available estimate from the synoptic upper air data.

Pressure usually is calculated from temperature measurements, since temperature is most readily measured with rocketsondes. However, the calculation technique and the sources of error are the same regardless of whether temperature or density is measured. The following discussion of calculation error has been abstracted from Ref. 6 to point up the problems that will be encountered. This discussion actually concerns the calculation of pressure from temperature rather than density, but it is illuminating nonetheless. Errors from a constant value of R are unimportant at altitudes below about 200,000 feet where dissociation begins, as long as the presence of water vapor is corrected by converting the temperature to virtual temperature according to Ref. 47. Virtual temperature is a familiar meteorological parameter and is defined as the temperature of dry air having the same density and pressure as the moist air. Mathematically, virtual temperature T_v is approximated by

$$T_v = (1 + 0.61 q)T \quad (47)$$

where T is ambient temperature and q is ambient specific humidity.

Reference 47 also shows that the assumption of a constant value for the gravitational constant, g , can cause errors of 1 to 2 percent between 30 and 60 km, but he points out that corrections for this error are readily made.

For rocketsonde calculations Ref. 47 shows that errors in temperature and base level pressure can be combined into a resulting total pressure error at a height Z_1 in the following expression:

$$\frac{P_\epsilon}{P_1} = \frac{P_*}{P_0} \left(\frac{P_*}{P_2} \right)^{\frac{\bar{T}}{\bar{T}}} - 1 \quad (48)$$

A typical example can show the magnitude of these errors. If it is assumed (1) that the base level pressure at 25 km is 30 mb, (2) that this may have a 0.5 mb error, (3) that the mean temperature error is 2 percent, and (4) that the pressure error is wanted when the calculated pressure is 1 mb, the equation becomes

$$\frac{P_\epsilon}{P} = \frac{30.5}{30} \frac{30.5}{1}^{0.02} - 1 = 0.09$$

or a 9 percent error in pressure. Putting this 9 percent pressure error and the 2 percent temperature error into the density calculation results in a 7 percent error in the calculated density at the 1 mb level.

It can be seen from Eq. 48 that the error resulting from an erroneous initial pressure value increases with distance away from the level. Thus, the calculation of accurate pressure and temperature data from an accurate density profile appears to be feasible.

7. TEMPERATURE

A number of measurement techniques have been suggested for use aboard sounding rockets, but temperature rarely has been measured directly except with a dropsonde. Several of these techniques which show the greatest promise of meeting the requirements of a large launch vehicle are evaluated here.

The total temperature tube discussed in Section 7.1 is deemed the best choice for direct measurement. It must be located on the nose tip and can be used with confidence only in continuum flow. However, all temperature techniques except calculation from the density profile, have these same shortcomings. The total temperature tube at least has the advantage of being a commonly used instrument.

7.1 Total Temperature Tube

Total temperature tubes have been used with success on airplanes and in wind tunnels. Reference 48 reports that two were successfully flown on Saturn SA-4. The problem with the use of this technique is that in rarefied air it is difficult to achieve a constant value of the recovery factor. Not only are the air molecules brought to rest and their energy absorbed in heating the sensor, but additional high-energy, high-speed molecules strike the sensor. If a sufficient number do this the recovery factor becomes uncertain and has been known to rise as high as 1.2.

In spite of these difficulties, a well-designed total temperature tube is deemed to be the most promising instrument for the onboard measurement of temperature.

7.2 Acoustic Meter

It is possible to utilize a measurement of the speed of sound waves to determine the ambient air temperature. This is due to

the well-known proportionality of the speed of sound to the square root of the absolute temperature of a gaseous medium, when the ratio of specific heats and the molecular weight are constant. However, because of the high speed of the vehicle in the present case, the measurement of the speed of sound must be made in such a way that either the air velocity is known or it does not enter into the equations used for reducing the data.

The most practical technique is to use an emitter and a receiver that are separated from each other as in Fig. 31. The two components would have to be far enough apart that the thickness of the hot boundary layer is small compared to the separation distance, L . However, the distance by which the two may be separated will be limited by the increasing effect of the forward speed of the vehicle upon the resultant direction of the sound waves.

Reference 49 describes an aircraft device which involves the use of two booms placed several inches apart and projecting ahead of the vehicle. These booms are in the form of slender half-wedges with the inside surfaces aligned parallel to the oncoming stream in order to achieve a very weak shock and a minimum of rotational flow between the transmitter and receiver booms. As is illustrated in Fig. 31, the longer boom would carry the emitter and the shorter the receiver.

In one configuration the emitter boom can be extended or retracted and the receiver is fixed. Temperature would be determined by the transit time required for the sound wave to travel the distance from the emitter boom to the receiver boom.

$$\sqrt{\gamma RT} = a = L/t \quad (49)$$

t is the time required for the sound to go from the emitter to the receiver booms. Another version of the configuration shown in Fig. 31 has multiple emitters along the longer boom. Some portion of the sound-wave envelope will encounter the receiver regardless of the forward velocity.

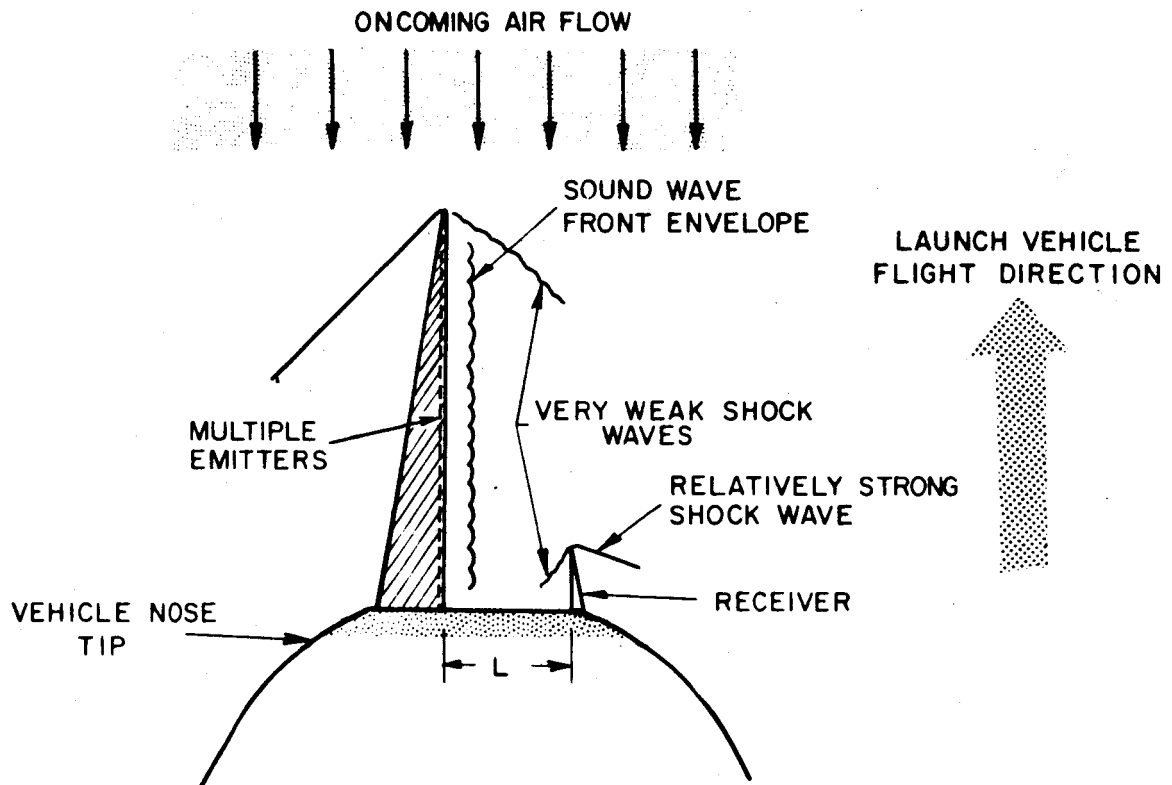


FIG. 31 ACOUSTIC METER MOUNTING CONFIGURATION

Multiple emitters on a single boom are a rather formidable problem. A type of continuous emitter would be highly desirable. A suggested alternative is a series of holes along the length of the boom. Weak shock waves emitted simultaneously from all of these holes would form a wave front traveling at the speed of sound, under proper conditions.

The time-measuring circuit could be so constructed as to be active only between the emission of a signal and the arrival of the envelope front at the receiver. Thus, any secondary sound waves due to extraneous noise will not affect the time circuit. For a one-foot separation between the two booms, an average traversing time of approximately 1×10^{-3} sec will be required. An estimate of the time response required for an allowable error of 0.5°C was made in Ref. 49, and it was found to be about one microsecond. This response time requirement does not in itself present any serious barrier.

For a launch vehicle flying between Mach three and five the booms would have to be rugged in order to withstand the buffeting of the impinging air stream and vehicle vibration. The leading edges must be sharp so that the shock wave on the side on which the emitter or receiver is placed is weak and causes no temperature jump. On the other hand, the thin boom tip material must be able to withstand a temperature which will approach 1200°C . If the strength or angle of the shock wave upstream of the transmitter and receiver cannot be reduced effectively to zero, or to a predictable magnitude, it will be very difficult to accurately convert local temperature measurements into free stream temperatures.

Techniques utilizing closely spaced resonators such as the Sonotherm discussed in Ref. 50 are not feasible, because at high altitudes the high power required heats the air in the confined space and the boundary layer thickness is on the order of the plate spacing. Thus, the boom mounted emitter-receiver technique appears to be the one which best meets the system requirements.

7.3 Resistance Thermometer

The University of Minnesota in their experimental work have made simulated thermistors by coating wires. Some of the older radiosondes used resistance wire elements. The Russian's Central Aeronautical Division has had repeated success up to 75 km, using tungsten wire resistance elements mounted on a MR-1 rocket (Ref. 10).

The temperature of the free atmosphere is calculated from the temperature measured by a thermometer placed longitudinally in the flow-around current of air by means of Izakov's formula. This formula relates ambient temperature to parameters such as rocket speed, density and heat conductivity of the thermometer material; heat exchange factor; thermal recovery coefficient; etc. The tungsten filament has a diameter of 40 microns and length of 30 centimeters, thanks to which the thermal inertia is lowered. The heat exchange through the thermometer supports and the radiation heat input from sources external to the rocket are also deemed to be low by the Russians.

Error in the measurement of atmospheric temperature by the method described increases with altitude. The mean-square error on a separate measurement at an altitude of 40 km is not more than 5 degrees; at 50 km it amounts to 10 degrees and at 70 to 80 km it is 20 degrees (Ref. 10). A certain increase in accuracy can be achieved by breaking up the measurements (over small altitude intervals) and by the exclusion of extreme values.

Further studies are in order on the uses of resistance wire elements. They are versatile in that they can be mounted or wound into many configurations. The dissipation constant of these elements could be high, time constants low, and excellent radiation characteristics also could be achieved by the proper selection of wire or suitable coatings. The reproducibility of one element to another could be better, both from an electrical and physical viewpoint, than thermistors; probably making the use of individual calibration curves unnecessary.

7.4 Vortex Thermometer

The use of the Hilsch effect resulted in the development of the axial flow vortex thermometer which is currently employed on meteorological aircraft. This thermometer has an effective recovery factor of zero, and, therefore, indicates the free air temperature. However, this recovery factor does begin to increase from zero at relatively low altitudes, e.g. 15 km, and it currently has a time constant of 10 seconds. Its Mach number limitation does not currently permit its use in rockets on ascent. In addition to the current NRL developments (first reported in Ref. 51), Armour-Research and Cornell Aeronautical worked on tangential flow vortex thermometers (Ref. 5).

Cornell Aeronautical did a considerable amount of work on the development of a sonic whistle, another outgrowth of development on the Hilsch effort. The resonant output frequency was a measurement of ambient free-air temperature. Again, low densities and other instrumentation problems limit the usefulness of this device to altitudes below those presently being considered.

7.5 Calculation

The one method of determining free air temperature which appears to work at all altitudes is to calculate it from some parameter which is amenable to direct measurement. Density is one such parameter. Calculation is further discussed in Section 6.5.

If the temperature, gravitational field, and the mean molecular weight of the atmosphere are assumed to be constant over the small height interval from h_1 to h_2 then temperature can be calculated from the following well known equation

$$T_2 = \frac{\rho_1 \bar{M}_2}{\rho_2 \bar{M}_1} \left[T_1 - \frac{\bar{M}_1}{\rho_1 R} \int_{h_1}^{h_2} \rho g dh \right] \quad (50)$$

An initial temperature must be available for the 30 km level in order to start the integration. This could come from a recent balloon sounding or a 10 millibar upper air chart. The value of T_2 would be sensitive to errors in the initial values of temperature, density and density profile. As the step-by-step integration proceeds upward it becomes relatively insensitive to error in the local density profile. (Ref. 23). The altitude should be available from radar track of the launch vehicle. The acceleration of gravity and the molecular weight of air as a function of altitude are readily available from Ref. 1.

Theoretically, temperature also could be calculated from pressure measurements made with the F-16 Q-Ball. A stagnation pressure port would be required. Temperature would be calculated from the relation:

$$T = \frac{\bar{M}}{\gamma R} \left[\frac{V}{M} \right]^2$$

However, since the Q-Ball is a blunt rather than a pointed cone, this relationship must be corrected for the detached and curved shock that actually will exist. This correction probably would require a wind tunnel research program.

7.6 Natural Radiation

The only method for measuring the free-air temperature remotely that appeared to be worth investigating was the infrared radiation intensity method. In certain bands where a gas is strongly absorbent, the emission of the gas will be equal to that of a blackbody at the same temperature as the gas. Since the blackbody radiation can be directly related to a specific temperature, the gas temperature can be ascertained by measuring the thermal emission in an absorption band.

The range of air temperature of interest is 200°K to 300°K, where blackbodies emit primarily in the spectral region between 5 and 30 microns. The constituents of the atmosphere which have absorption bands in this region are primarily water vapor, carbon dioxide and ozone.

Of these, carbon dioxide is most suitable because of its uniform distribution throughout the atmosphere both vertically and horizontally. Within the spectral range of interest, carbon dioxide absorption bands occur at 4.3 and 15 microns. The 15 micron band is preferable because it is closer than the 4.5 micron band to the peak of the blackbody curve.

If the total radiant energy from a given volume of space is measured with an infrared radiometer the average temperature of that volume can be determined. The actual amount of energy that will be detected by the radiometer is expressed, for essentially monochromatic radiation, by the following functional relationship which is derived on p. 12 of Ref. 52.

$$I(\nu, d, \beta) = \frac{3}{8} \left(\frac{D \cos \beta}{R} \right)^2 \sec \beta \left[(h\nu^3/c^2) (\rho dV/e^{h\nu/kT} - 1) \right] \exp \left(-k \int_0^d \rho dz \right) \quad (51)$$

The total radiant energy which impinges at the collector will be obtained upon integrating Eq. 51 over all the volume within the field of view.

If the composition of the atmosphere, the density, and the absorption coefficient are known, then Eq. 51 relates the dependence of the measured radiant energy to the static temperature of the gas within the field of view. If the temperature gradients within that portion of the field of view which contributes significantly to the measured energy are small, then the intensity of radiant energy can be used as an indirect measurement of the local static temperature in the forward field of view. A radiation-sensitive instrument such as a photometer, therefore, could be calibrated as a temperature-measuring device. In practice, however, the dependence of the radiation strength at the collector on the density field in the direction of view is a complicating factor. Fortunately, however, a temperature-measuring device can be constructed which effectively cancels out the density dependence through utilization of a null measuring technique involving the measurement of the difference between the energy direct from the atmosphere and the energy modified by transmission through a temperature-controlled gas cell.

In Ref. 52 Astheimer investigated the path lengths using a method of treating this type of band absorption developed by W. M. Elsasser. The spectral absorption is given by the error function of the square root of the product of the spectral absorption coefficient and the total amount of absorber in the path. It was found that in order to achieve 90 percent absorption at an altitude of only 13 km, a path length of 250 meters was required. For 99 percent absorption the path length increased to 10,000 meters. This means in effect that the temperature calculated from Eq. 51 is the average over a column 10 kilometers long. Whether or not this temperature is sufficiently representative of the free-air temperature near the launch vehicle requires some thought. One way in which the required path length could be reduced is to use filters with narrower band passes.

A major problem with this technique will be temperature gradients in the boundary layer and shock waves. The boundary layer problem could be circumvented by placing the aperture near the nose tip, but this would necessitate looking through strong, hot shock waves. The discussion of this technique in Ref. 52 indicated that they would investigate this problem for their final report. We tried to obtain a copy of this final report to examine their findings before we undertook an investigation on our own, but to date we have been unsuccessful.

A problem that is unique to the present application is contamination of the atmosphere by entrainment of the rocket engine exhaust products. Carbon dioxide from the exhaust probably will not be in equilibrium with the atmosphere. Of course, if it is and the density can be measured, the increased amount of CO₂ present will greatly reduce the required path lengths. Another problem is scattering from dust and exhaust particles.

We are unable at this time to render a judgment on this technique. The progress made by Barnes Engineering Co. should be watched for possible application to large launch vehicles.

8. WIND

The only feasible location for a wind instrument is on the escape rocket tip, or the vehicle nose tip if no escape rocket is used. Since wind-induced angle of attack is the most critical flight parameter, considerable time and effort were given to wind measurement techniques.

Our research led us to the conclusion that the two best ways of measuring the wind were either with a fixed conical pitot-static tube or the modified spin-pressure modulation technique. The methods are discussed in Sections 8.1 and 8.3.

Actually, the conical pitot-static tube, in the form of the F-16 Q-Ball, presently is being used to measure angle of attack by NASA. NASA-Marshall has collected a large quantity of wind tunnel calibration data on the Q-Ball, and the most expedient course would be to use it for both high-altitude angle-of-attack and wind measurements. Consequently, we turned our attention to the possibility of using an electro-optical technique to precisely sense the minute movements of a differential pressure diaphragm of the type that the F-16 Q-Ball could carry. (See Section 8.2).

8.1 Fixed Cone

The requirement of being able to operate during a severe vibration environment as well as one of very light wind force suggests the use of a fixed device. In this way the problem of damping and pivot friction is eliminated. With a fixed device the most practical way to sense wind is to measure the pressure difference between static pressure ports. The flow angularity is determined by measuring the difference between the pressure coefficients of diametrically opposed orifices.

8.1.1 Theory

Recent experimental work done by F. Swalley of NASA-Langley indicates that a conical probe is capable of measuring flow angularity at high Reynolds numbers and speeds where the shock is attached to within one-third of a degree (Ref. 29). The tests were conducted in a 3-inch diameter helium blowdown tunnel at Langley Research Center. The model was a cone-cylinder combination with the included angle cone being 80° . Four orifices, 0.020 inch in diameter, were spaced equally around the model in a plane 0.071 inch from the nose.

The difference in pressure coefficient for diametrically opposed orifices, as given in Ref. 30 to a second order approximation, is

$$\Delta C_p = 2 \sin^2 \tau \left[4\xi \cos \tau \cos \phi - \frac{2\xi \cos \phi}{\cos \tau} \left(\frac{\sin^2 \tau}{2} - \frac{4}{15} \right) \right] \quad (52)$$

The cone and flow field geometry is shown in Fig. 32.

A comparison of corrected wind tunnel data with values calculated with the use of Newtonian theory and the theory of Ref. 30 showed excellent agreement at small yaw (or pitch) angles. The error increased with yaw or pitch angle for each theory. Cheng's theory always gave the best agreement and in most cases underpredicted by less

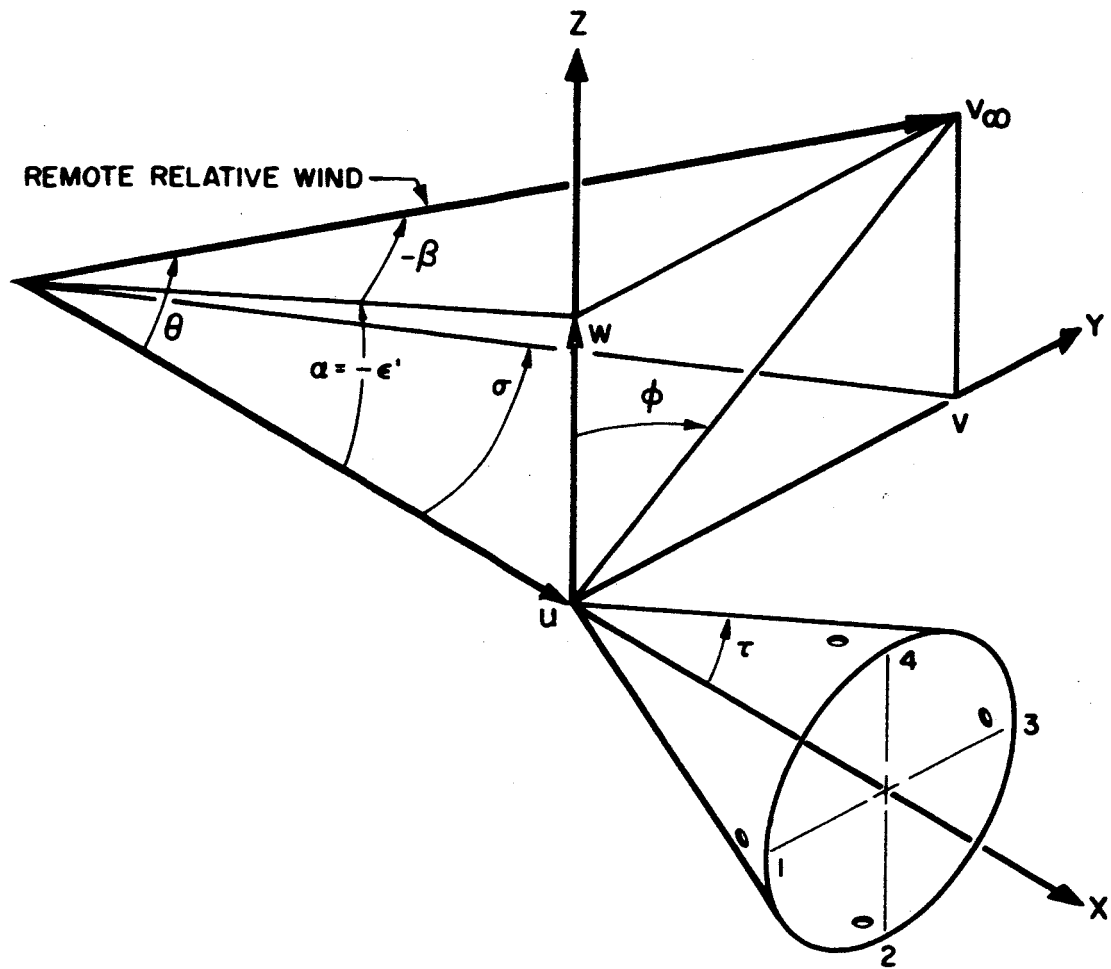


FIG. 32 FIXED-CONE WIND GAGE FLOW-ANGLE NOTATION

than 2 percent (which is within the experimental accuracy) with a few instances of 13-percent error. Newtonian theory is not quite as good, usually giving an error of 3 percent at $\theta = 5^\circ$ and occasionally an error of 15 percent.

It was concluded that Mach number had only a small or negligible effect on the difference in pressure coefficient between diametrically opposed orifices and, consequently, on flow angularity. Therefore, the indications are that at higher Reynolds numbers and at speeds greater than that necessary for shock attachment the difference in pressure coefficient is nearly independent of Mach number and test medium for the case of air and helium.

For convenience in obtaining the air stream component in the pitch and yaw planes directly, curves are presented in Ref. 29 for positive values of pressure coefficient differences from which these angles can be determined without recourse to equations.

8.1.2 Use of F-16 Q-Ball

The Q-Ball does not meet the pointed cone and attached shock requirements of the foregoing theory. However, through utilizing aerodynamic calibration factors determined from extensive wind tunnel tests an empirical relation between differential dynamic pressure difference and angle of pitch and yaw histories has been established. (Refs. 48 and 53). Knowing these angles and the vector velocity of the launch vehicle it is possible to calculate the speed and direction of the wind causing the pitch and yaw. This computation method is discussed in Section 8.2.5. In actual practice the computation will be rather complex since the vehicle constantly is pitching and yawing in response to the wind and steering orders. However, it should be possible to devise a computer program which can take each of these factors into account while it is processing the differential dynamic pressure data.

8.2 Electro-Optical Data Pickoff

During the analysis of the wind sphere an electro-optical data pickoff was suggested as a means to precisely sense minute movements of the pressure diaphragm without attaching any additional mass to it. The NASA technical monitors expressed interest in this technique for use with the F-16 Q-Ball angle-of-attack meter. It was hoped that an electro-optical data pickoff would make possible the use of multiple pressure sensors and, thus, increase the operational ceiling of the device. Consequently, this data pickoff technique was given considerable attention. It shows great promise of providing a means of detecting very small diaphragm deflections with a device that has no moving parts and does not require that anything be attached to the diaphragm.

The Q-Ball presently used with the Saturn utilizes Rosemount Engineering differential pressure diaphragms with a capacitive data pickoff. These pressure sensors are effective only up to 45 km where the dynamic pressure of about 200 kg/m^3 is insufficient to cause them to respond. We believe that a logical course would be to place a sufficient number of more sensitive sensor sets within the Q-Ball so that the entire altitude range could be covered. The high-altitude sensors would be sealed off at low altitudes and opened at the bottom at the altitude interval over which they are effective. By using electro-optical data pickoffs it should be possible to widen the dynamic range over which each set of sensors is effective and, thus, to reduce the number required.

Calculations were made of the range of dynamic pressure difference across a set of pressure ports for an angle of attack of 0 to 10 degrees and a Mach number range of 1.5 to 5.3. It was found that the range of the dynamic pressure difference for an angle of 10 degrees is from 136 to 2300 kg/m^2 . For zero angle the difference is zero. To cover this range several separate sets of pressure diaphragms may be necessary. Getting all of the sensors, ducting, and data pickoffs into

the 4-inch diameter tip of the Q-Ball will be a difficult task. A major advantage of electro-optical pickoffs is that they can be compact and show promise of being compatible with the small space available.

8.2.1 Light Beam Deflection Technique

Several methods have been studied for optically measuring the deflection of a diaphragm due to a pressure difference on the two sides. These included interference fringes, Moiré patterns, Golay cell method, light intensity change, and angle of reflection change. At present, the last shows the greatest promise for use on a rocket.

In this technique one spot on the rim of the differential pressure diaphragm is coated with a reflective material. A light source is located outside the duct and shines on the reflecting spot through a window in the duct. This is illustrated in Fig. 33. The light beam is reflected from the diaphragm through a second window onto a lateral photocell. As the diaphragm deflects, the reflected beam will move across the lateral photocell. Because of its unique position-sensing abilities the voltage output of the cell will be a function of the position of the light spot in x-y coordinates. With the fixed geometry of the unit, the x-y position can be calibrated in terms of diaphragm deflection, which, in turn, can be calibrated in terms of the pressure differential across it. For a light beam of finite size the diaphragm might actually deflect in two dimensions, so a simple one-dimensional cell would not be completely adequate. Fortunately, a suitable lateral photocell is readily available. Electro-Optical Systems, Inc. markets a version called the Radiation Tracking Transducer (RTT[®]), which probably can be adapted to this use.

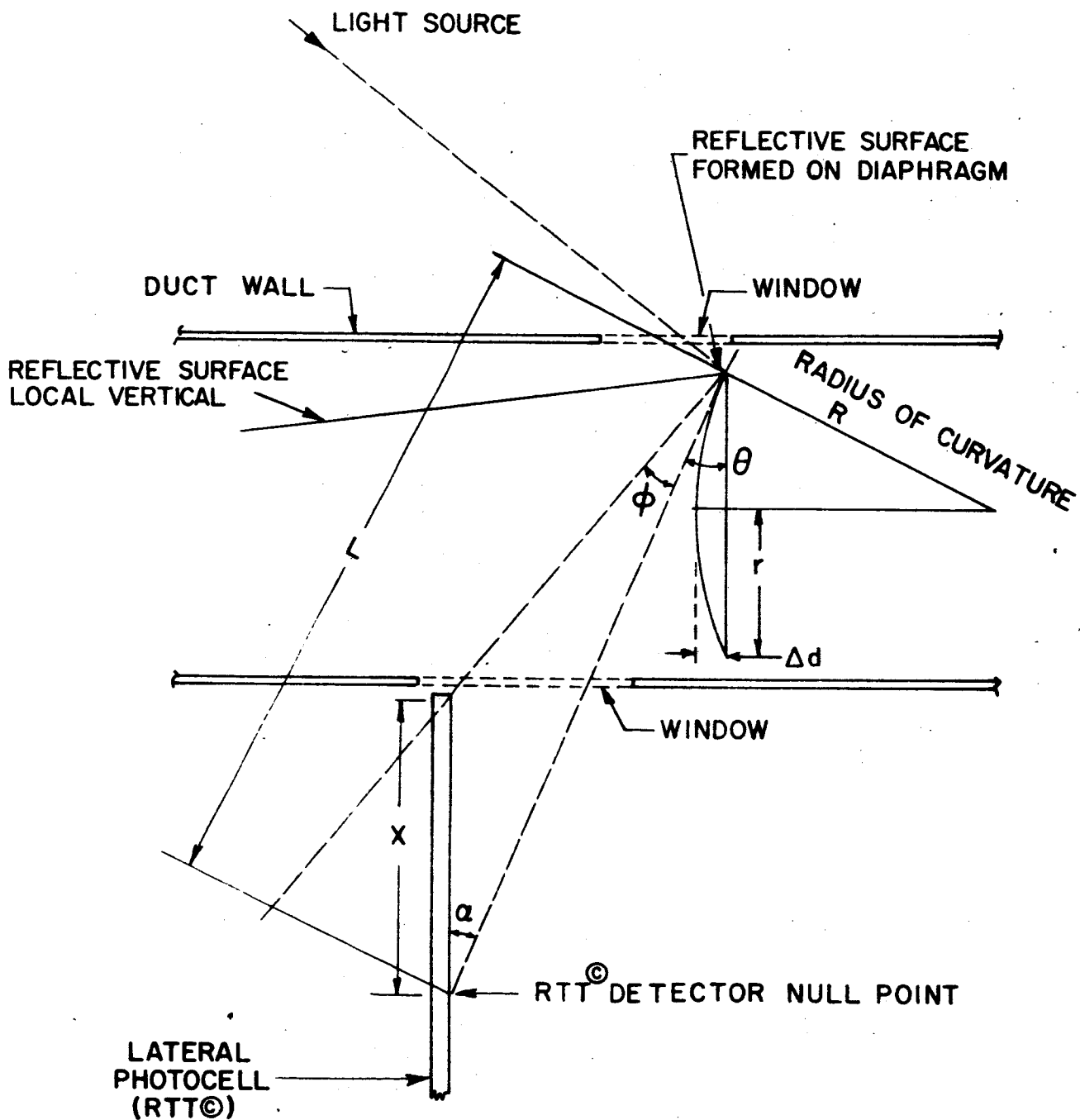


FIG. 33 ANGULAR DEFLECTION OF LIGHT METHOD OF SENSING DIAPHRAGM DEFLECTION USING LATERAL PHOTOCELL

8.2.1.1 Optical Geometry

The dimension D shown in Fig. 34 is the absolute value of the maximum movement of the reflected light beam from the null position. The detector must have a radius at least this large. Calculations have been made which indicated that the rim deflection angle θ may be as much as 12 degrees where θ is given by:

$$\theta = \sin \frac{-12\Delta d}{r} \approx \frac{2\Delta d}{r} \quad (54)$$

Therefore, the small angle approximations are not truly valid. As indicated in Fig. 34 the deflection of the light beam is due to both the movement of the diaphragm through the angle θ and the change in the point from which the reflection takes place from δ_1 to δ_2 . Thus, the total light beam deflection D is, from Fig. 34:

$$D = a + b \quad (55)$$

where the distances a and b are defined by

$$b = \delta \frac{\sin^2 \theta}{\tan \beta \sin (\alpha + \phi)}$$

$$a = L \frac{\sin \phi}{\sin (\alpha + \phi)}$$

The expression for the total beam deflection then is:

$$D = \frac{\sin \theta}{\sin (\alpha + 2\theta)} \left[2L \cos \theta + \frac{\delta \sin \theta}{2 \tan \beta} \right] \quad (56)$$

where, as depicted in Figs. 33 and 34,

δ : displacement of reflecting surface from diaphragm rim

L: distance of RTT center to reflecting surface

θ : diaphragm rim deflection angle

β : angle between light source and diaphragm

α : angle between RTT and light path from diaphragm

ϕ : change in angle of reflection = 2θ

8.2.1.2 Detector Size

Suitable pressure diaphragms appear to be available for the range of 70 to 2460 kg/m² (0.1 to 3.5 psi). This range of

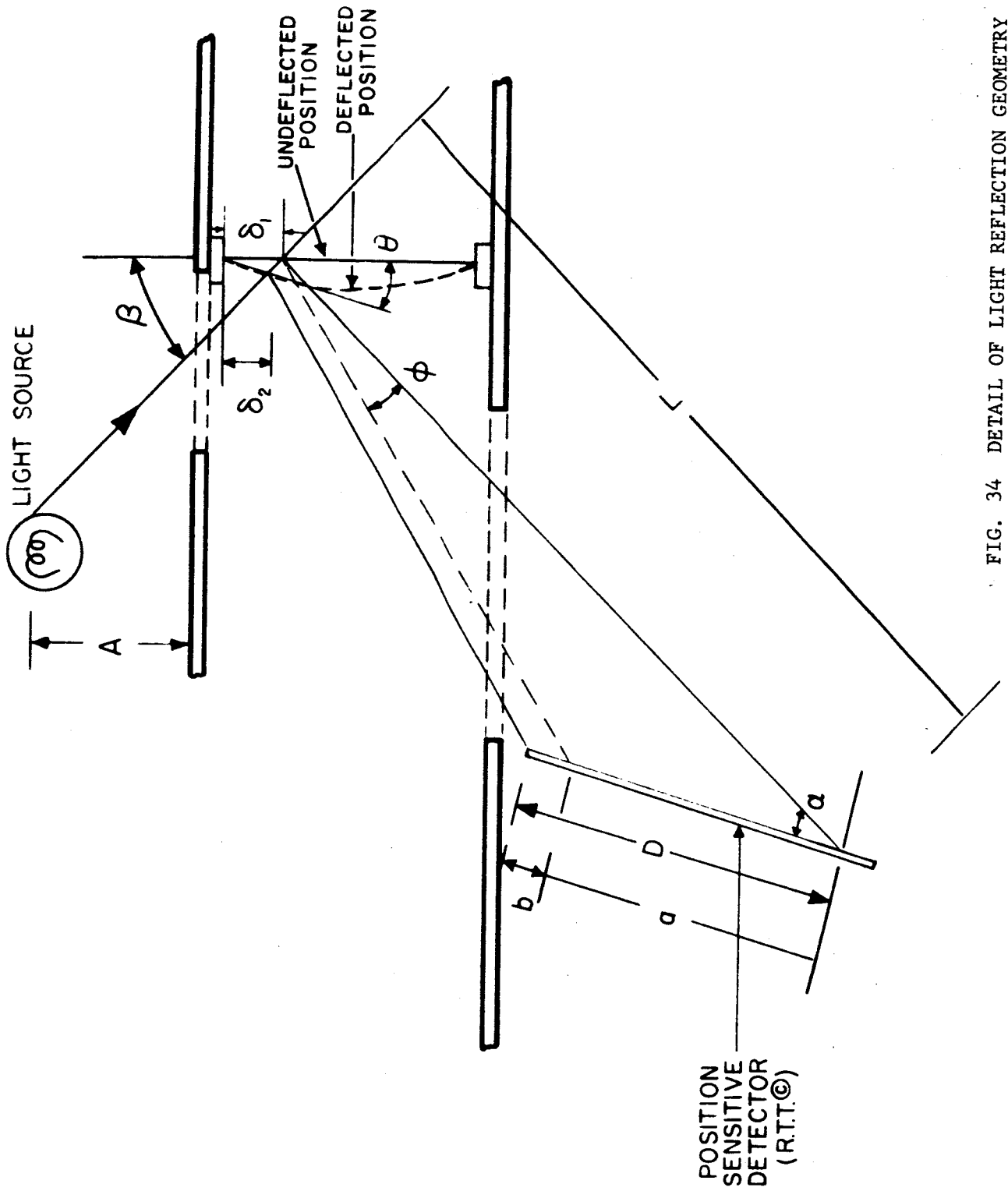


FIG. 34 DETAIL OF LIGHT REFLECTION GEOMETRY

pressure would cause the center of a 1-cm-diameter diaphragm to deflect from 0.0015 to 0.05 cm. It is unlikely, though, that a single diaphragm can cover this range. In order to be sturdy enough to resist bursting at high-differential pressures it would be too stiff to respond at very low-differential pressure. This need for multiple sets of gages may actually prove to be an advantage from the point of view of data pickoff. The amount of deflection of the light ray caused by a single diaphragm deflecting through the entire range of 0.0015 to 0.05 cm would be larger than could be contained within the 0.6 cm radius of the RTT version of the lateral photocell.

Using the foregoing diaphragm deflections and typical values of the optical system parameters depicted in Figs. 33 and 34, the anticipated excursion of the reflected light beam was estimated.

$$\begin{aligned}r &= 0.5 \text{ cm} \\ \beta &= 10^\circ \\ \alpha &= 90^\circ \\ \delta &= 0.125 \text{ cm} \\ L &= 1.6 \text{ cm}\end{aligned}$$

We found for a diaphragm deflection Δd of 0.05 cm that the total light spot travel would be 1.1 cm. For a Δd of 0.0015 cm the travel would be 0.010 cm.

One solution to the large travel of the light spot is to use a double size RTT which has a radius of 1.2 cm. However, a double size RTT would require some development. In view of the remarks in the first paragraph above, the most practical solution probably would be to use two or three sets of gages, each of which covered a portion of the pressure range.

The diaphragms would vary in response so that the full range of each resulted in a light spot travel of slightly less than 0.5 cm. It is impossible here to decide exactly how many gage sets would be required because the final choice must be a tradeoff between

so many variables; e.g., diaphragm size, diaphragm stiffness, the angle β , the angle α , etc. We believe that two sets might be sufficient and that three sets surely would be adequate.

8.2.1.3 Output Signal Level

It is convenient to place the light source and the detector the same distance from the diaphragm. Therefore, distance A in Fig. 34 is $1.6 \cos 5^\circ = 1.6$ cm. For a light source of about 1 watt output, about 100 mw of light will get to the detector. This is greater than the saturation power for the RTT; therefore, the detector output will be about 0.3 mv/0.001 cm independent of light power. The RTT can detect movements of the light spot of less than 0.010 cm. A movement of 0.010 cm will cause an output of 3 millivolts. There will be no problem in coupling a signal of this magnitude into any electronics needed. If a certain diaphragm deflection or light beam deflection should result in an output of less than 0.25 mv, it might be necessary to utilize a higher resistivity silicon for the RTT. This would increase the output.

8.2.1.4 Vibration Effects

Vibrations should cause no trouble in obtaining useful signals. The detector has a time constant greater than 10 microseconds. The electronics can have a bandpass set so that voltage variations due to vibrations are not seen.

8.2.2 Light Intensity Change Technique

The most straightforward approach is to shine light onto the pressure diaphragm and reflect it onto a photodetector which then determines intensity variation. A photodiode will have an output current given by

$$I = \frac{PAS}{4\pi D^2} \quad (57)$$

where

- P: light intensity in watts
- A: area of light spot on detector
- D: distance from source to detector
- S: detector sensitivity in amps/watt

A small change in light intensity on a detector is more accurately detected by using a differential method. Two detectors are set up so that light from one source shines on both by using a half-silvered mirror and a reflecting diaphragm (See Fig. 35). The parameters of Eq. 57 are set for each detector so that the output current of detector A equals that of B in the no-deflection condition. Then only the difference in outputs between A and B is seen in the amplifier.

For the setup shown in Fig. 34. the difference in output of the two detectors is given by

$$\Delta I = \left(\frac{PAS}{4\pi D^3} \right)_B \Delta d \quad (58)$$

where

- Δd : movement of the diaphragm
- $()_B$: indicates that the values of the parameters for detector B are used.

As an example, assume

- P = 0.1 watt
- S = 0.1 amp/watt
- A = 10^{-2} cm²
- d = 10 cm
- Δd = 0.001 cm

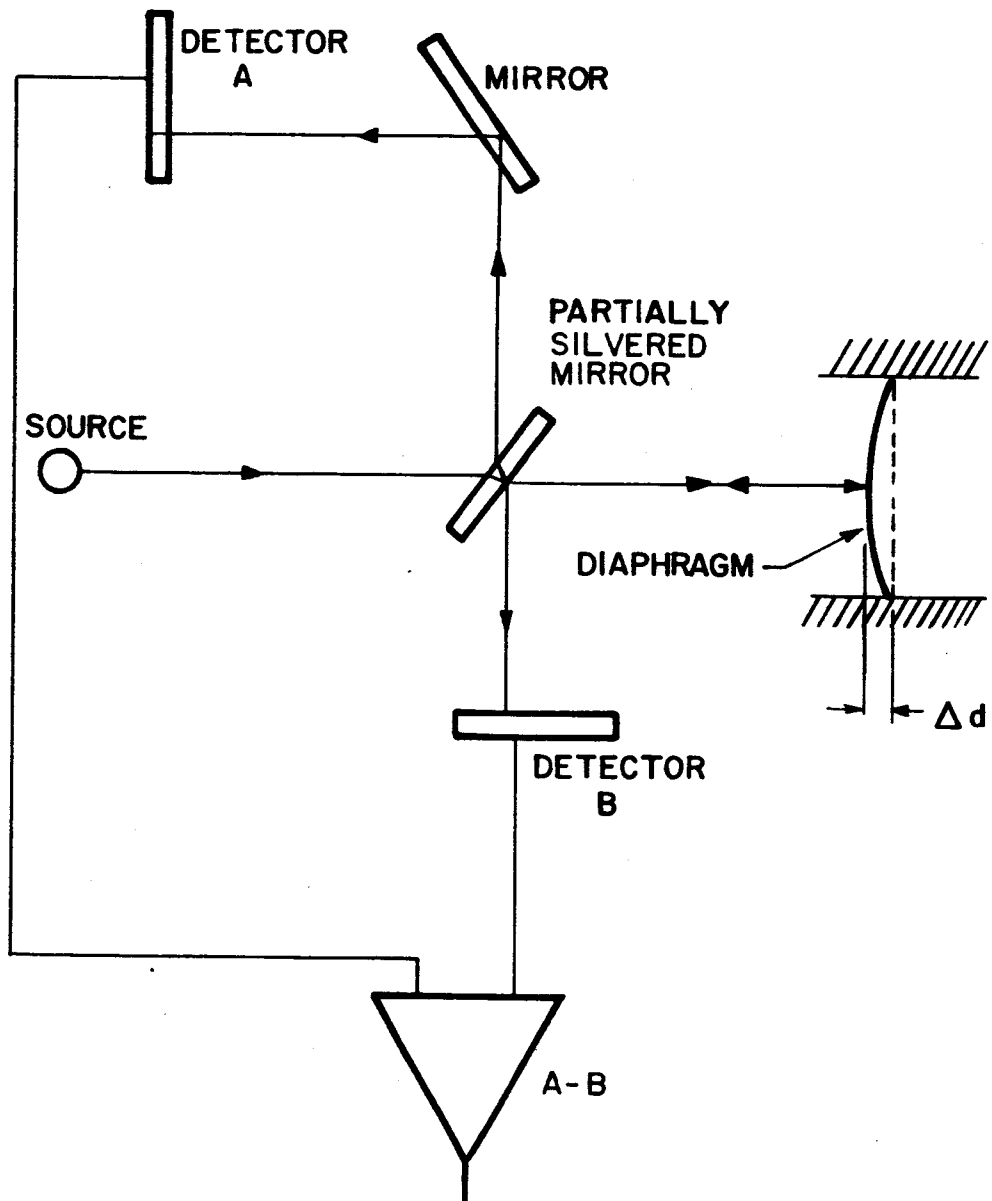


FIG. 35 INTENSITY VARIATION OF LIGHT METHOD OF SENSING DIAPHRAGM DEFLECTION

Then $\Delta I = 10^{-11}$ amp. At first glance, this signal appears to be too low for practical amplifiers. However, it is possible that this simple design could be optimized to increase $\Delta I/\Delta d$ by a factor of 100.

8.2.3 Interferometric Technique

The use of optics to sense mechanical deflection is a common technique when extreme accuracy is required. An interferometric method is standard in many laboratories. In this method, a phase difference between two beams of light from a single source appears when the length of one light path changes with respect to the other. The phase difference is seen as interference fringes where the beams come together. A detector can be set up to count the number of successive light and dark fringes. However, a complex setup would be required to determine the direction of fringe motion. Without this, pressure differential could be determined, but its direction could not.

8.2.4 Index of Refraction Change Technique

As a last technique, the change of phase of a light beam with pressure due to index of refraction change was investigated. This method divides the pressure duct with a fixed membrane and directly measures the pressure difference between each half of the duct. The index of refraction of the air is a function of pressure. The phase change is given by

$$\Delta\phi = \frac{2\pi L}{\lambda} K\Delta P \quad (59)$$

where

- L: light path length over which pressures are different
- λ : wavelength of light
- K: constant = 2×10^{-5} in English system
- ΔP : pressure difference in two compartments

As an example let

$$\begin{aligned}L &= 1 \text{ inch} \\ \lambda &= 2 \times 10^{-5} \text{ inch} \\ \Delta P &= 0.002 \text{ psi}\end{aligned}$$

This ΔP corresponds to the difference in dynamic pressure across a pressure diaphragm for a 0.1 degree angle of attack at the maximum altitude. With these values $\Delta\phi = 0.013$. Whether or not this technique can be implemented at high altitudes where the absolute pressure is very low requires additional study.

8.3 Spin Pressure Modulation

The only successful attempt at measuring winds in the mesosphere and above that we have encountered is the flights of Ainesworth, Fox and La Gow at Fort Churchill during the I.G.Y. (Ref. 23). They used an Aerobee equipped with a pitot-static tube and utilized the cyclical pressure measured at the static port in a method called spin pressure modulation.

The method can be visualized by examining Fig. 36. Owing to the rocket's angle-of-attack which varied from 1 to 20 degrees, the spin-pressure was modulated at the rocket spin-rate. In the continuum-flow region there existed during each modulation cycle two values of spin-pressure that were selected and converted to ambient pressure. Above 100 km, where conditions of free molecular flow existed for the pitot-static tube, ambient densities and winds were obtained from measurements of the modulation amplitude of the spin-pressure, the rocket velocity, and the rocket angle-of-attack. Because the amplitude of the pressure modulation was small and was obscured by the ambient atmosphere or by outgassing of the pressure sensor, an ac amplifier was connected to the output of the pressure sensor. In this way the ambient and residual gas signals were blocked, and the pressure modulation was passed and amplified.

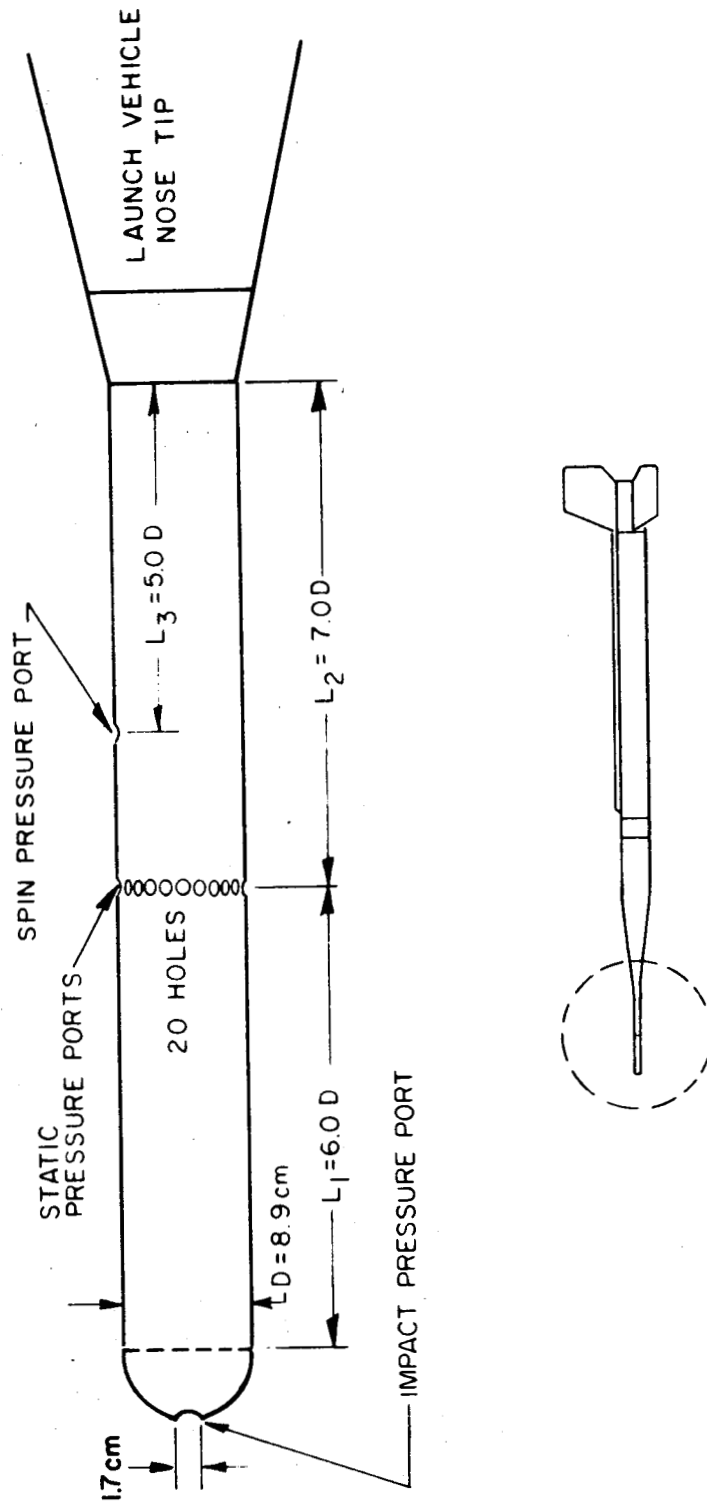


FIG. 36 CONFIGURATION OF A PITOT-STATIC TUBE

8.3.1 Spin-Pressure-Modulation Technique

In the present case the booster nominally will fly at an angle of attack of only +2 to -5 degrees. Therefore, it is necessary to make some changes in the Ainsworth technique which requires a larger angle of attack. We suggest three cylinders mounted orthogonally, each of which would rotate about its own axis. Actually, the third cylinder is superfluous, since two cylinders mounted orthogonally would be sufficient. Each of these rotating cylinders would contain a static pressure port that would be monitored. The reading from the pressure port when no wind is blowing is due to the impact of the air caused by the upward motion of the vehicle. A plot of the pressure readings of the spinning cylinder would tend to follow a cosine-squared curve as depicted in Fig. 37. Between 90 and 270 degrees the port would monitor base pressure and no attempt was made to estimate this pressure for the figure. If a wind were blowing, the resultant vector formed by the booster velocity and the wind velocity would cause the shock wave and pressure peak to shift to one side as depicted in Fig. 38. A measurement of the angle δ at which the pressure-peak occurs can be used to determine the direction and magnitude of the wind.

8.3.2 Expected Pressure-Peak Displacement

Reference 2 and similar sources were consulted to determine the envelope of expected maximum horizontal winds for the altitude range of interest. The maximum expected angle of pressure-peak displacement (angle δ of Fig. 38) was calculated using the maximum wind profile tabulated in Table IX and a typical velocity profile of a large liquid booster. The resulting angles of pressure-peak shift also are tabulated. A striking feature of this investigation is that the horizontal wind speed in the region of 30 to 100 km can be sufficiently high, compared to the vertical speed of a representative large launch vehicle, that the shift of the pressure-peak could be as high as 31 degrees.

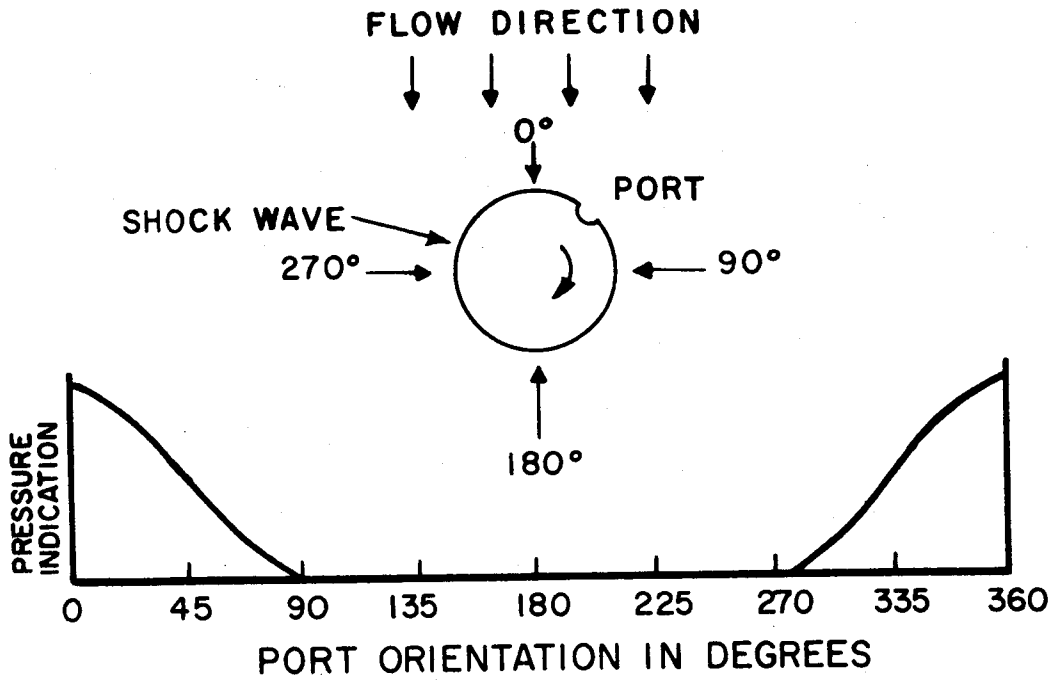


FIG. 37 PRESSURE PROFILE AROUND A CYLINDER IN A NORMAL FLOW FIELD SHOWN ABOVE

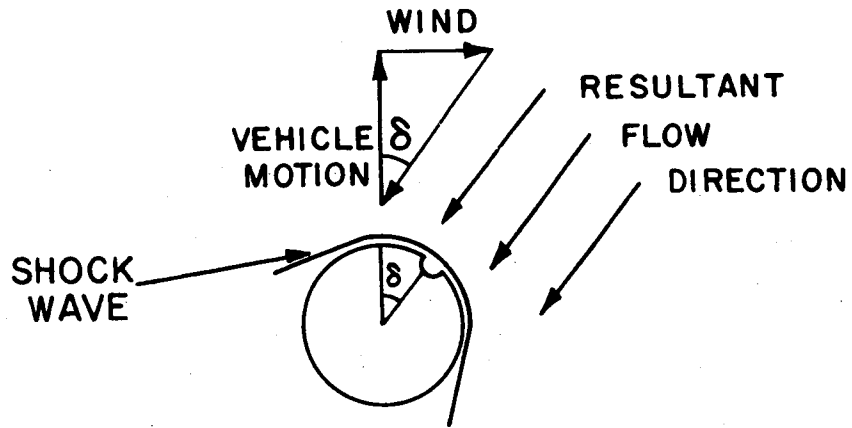


FIG. 38 PRESSURE-PEAK SHIFT CAUSED BY LOCAL WINDS

TABLE IX

MAXIMUM EXPECTED ANGLE OF SHIFT OF
PRESSURE-PEAK CAUSED BY WIND

Altitude (Kilometers)	Maximum Wind (Meters/Sec.)	Angle of Shift (Degrees)
30	50	17
40	150	31
50	175	27
60	200	24
70	230	22
80	250	19
90	290	17
100	300	17

8.3.3 Detecting Shift of Pressure Peak

There are three ways to detect the shift angle of the pressure-peak. One is to note the actual position where the pressure-peak occurs. However, if the peak were very flat it would be difficult to determine precisely the angle at which the pressure-peak occurs. Another method is to determine the angle where the pressure approaches ambient. This occurs when the pressure ports are aligned with the flow direction as at the 90° and 270° points in Fig. 39. The angle point midway between these two angles would be the angle of the pressure maximum. A third method is to locate two ports at opposite ends of a diameter or chord of the cylinder and to note the angle at which the difference of pressure between the two ports is zero. The last method appears to be the best in that it measures a pressure difference rather than an absolute value. The pressure reading when this method is used is sketched in Fig. 40. The pressure-peak lies midway between two successive crossover points.

8.3.4 Rate of Spin

In order to determine the fine structure of the wind fluctuations it appears necessary to have an instrument response that spins at the rate of 0.02 revolutions per second. Thus, the instrument

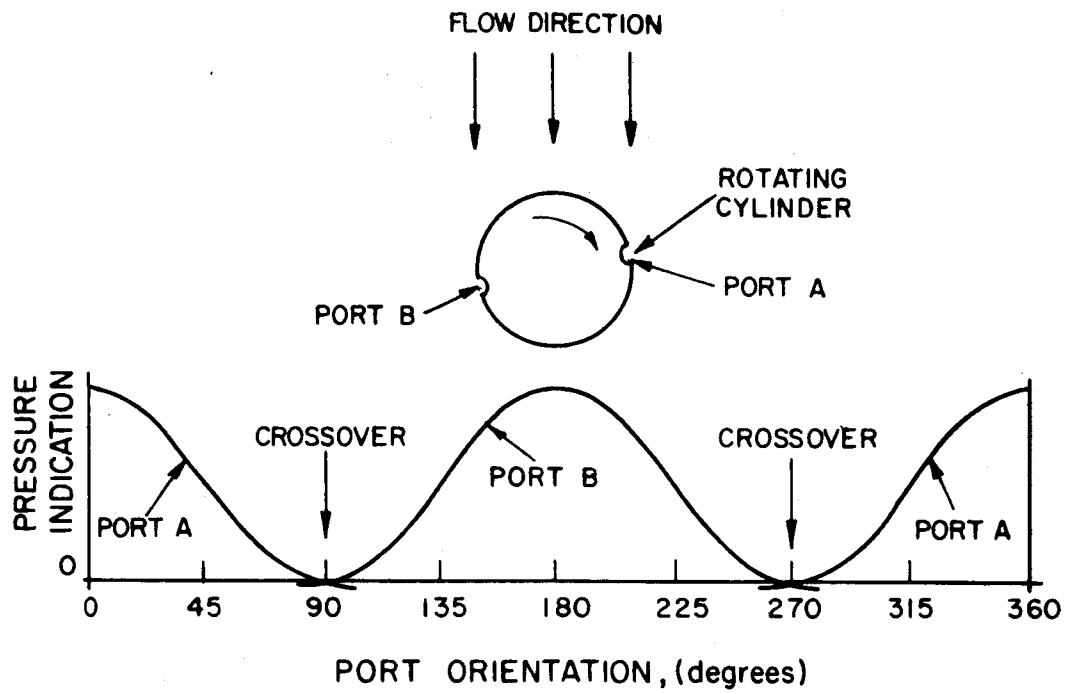


FIG. 39 CROSSOVER METHOD FOR DETERMINING WIND DIRECTION

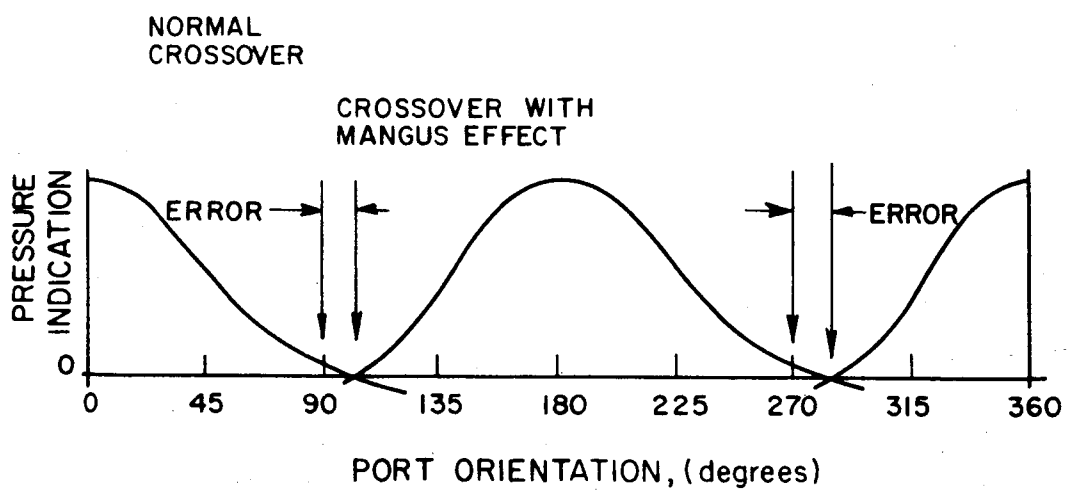


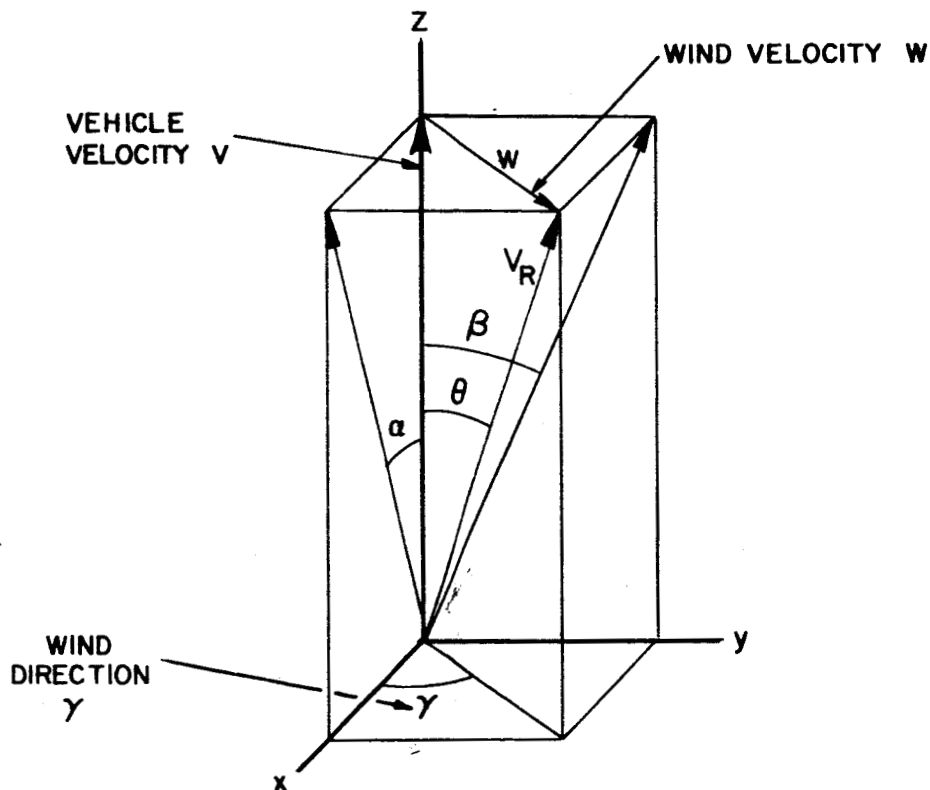
FIG. 40 ERROR CAUSED BY THE MANGUS EFFECT

would be capable of following winds that change at the rate of 0.131 meters/sec per meter of altitude. This rate is cited in Ref. 2 as the maximum wind shear that will be encountered.

The pressure difference on opposite sides of a rotating cylinder due to the Mangus effect was calculated from the formula $\Delta p = 2\rho Vv$ where Δp is the difference in pressure between the opposite ends of the cylinder diameter. At 60 km altitude, for instance, the pressure differential due to the Mangus effect is about three decades below the ambient pressure, and the artificial pressure differential will cause a negligible displacement of the crossover point.

8.3.5 Calculation of Wind Speed and Direction

The following derivation illustrates a method of determining the wind speed and direction using the spin pressure modulation technique.



Let V = vehicle velocity vector along z axis

W = wind vector

$V_R = V + W$ = resultant vector

θ = angle between V_H and V

γ = wind direction

The known quantities from the booster and spin pressure modulation ports or fixed Q-Ball ports are:

V , α , and β

Then

$$\tan \theta = \frac{W}{V}$$

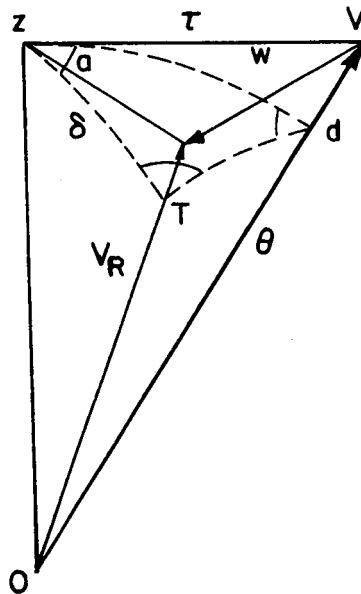
$$\tan \theta = \left[\tan^2 \alpha + \tan^2 \beta \right]^{1/2}$$

$$\text{Wind speed, } W = V \left[\tan^2 \alpha + \tan^2 \beta \right]^{1/2}$$

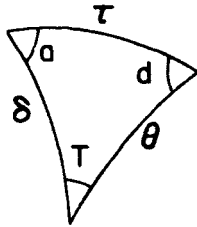
and the wind direction is represented by:

$$\gamma = \tan^{-1} (\tan \beta / \tan \alpha)$$

For the general case where there is an angle between the z axis and V , θ is calculated as before.



The wind is assumed to be horizontal so that the plane z, V, V_R is also horizontal. The spherical triangle formed by the dotted lines is used to find a .



$$\cos \delta = \cos \tau \cos \theta + \sin \tau \sin \theta \cos d.$$

$$\sin a = \frac{\sin \theta \sin d}{\sin \delta}$$

$$W^2 = (\overline{Z V})^2 + (\overline{Z V_R})^2 - 2 \overline{Z V} \overline{Z V_R} \cos a$$

$$W^2 = V^2 \sin^2 \tau + V^2 \cos^2 \tau \tan^2 \delta - 2 V^2 \sin \tau \cos \tau \tan \delta \cos a$$

$$W^2 = V^2 \left[\sin^2 \tau + \cos^2 \tau \tan^2 \delta - 2 \sin \tau \cos \tau \tan \delta \cos a \right]$$

The wind direction γ is the angle between W and $\overline{Z V}$.

$$\overline{Z V_R}^2 = W^2 + \overline{Z V}^2 - 2W \overline{Z V} \cos \gamma$$

$$\gamma = \cos^{-1} \left[\frac{(W^2 + \overline{Z V}^2 - \overline{Z V_R}^2)}{2W \overline{Z V}} \right]$$

Thus the wind direction is:

$$\gamma = \cos^{-1} \left[\frac{W^2 + V^2 \sin^2 \tau - V^2 \cos \tau \tan \delta}{2W V \sin \tau} \right]$$

8.4 Internal Accelerometers

All large launch vehicles carry internal accelerometers to monitor vehicle attitude for control purposes. These accelerometer

systems cannot be used for wind monitoring because their primary use as controls requires that they be too heavily damped to detect changes in attitude due to wind. Even if sensitive accelerometers were carried it would be extremely difficult to relate a change in vehicle attitude to a change in wind. The transfer functions which relate angle of pitch and yaw to wind for such a massive vehicle probably never will be known with any degree of certainty. Consequently, it appears that an internal accelerometer system does not meet the requirements.

8.5 Wind Sphere

Before we were made aware of the development program for the F-16 Q-Ball, we investigated at length the aerodynamic and mechanical characteristics of a rotatable sphere. The sphere would be carried in a housing similar to that of the Q-Ball of the X-15 airplane. The instrument would sense a change in the resultant wind by means of differential pressure gages in ducts which connect static pressure ports on opposite ends of a sphere diameter. A servodrive would rotate the sphere to maintain it relative to the wind so that the differential pressure is zero. The sphere displacement along with the vehicle velocity is a measure of the wind speed and direction. We investigated the requirements imposed on the system by the magnitude of the resultant wind change and the amount of gage deflection likely to occur due to wind, vehicle vibration and vehicle acceleration.

8.5.1 Instrument Drive Range

Referring to Table IX, it is seen that the maximum expected angle between the vehicle path and the resultant wind is 31 degrees occurring at 40 km altitude. Thus the wind sphere must be designed so that it can be rotated about 30 degrees in any direction. In a practical situation, however, a launch vehicle probably never would fly at such a large angle of attack, but this is the upper bound.

8.5.2 Required Response Speed

The maximum expected wind shear reported in Ref. 54 is 0.131 sec^{-1} for a 500 meter altitude layer. This means that the horizontal wind velocity will change by 0.131 meter/sec, as the vehicle rises 1 meter. It can be shown that for small changes

$$\frac{d\alpha}{dt} = \frac{\Delta\alpha}{\Delta t} = S$$

where α = angle of attack

S = wind shear

t = time

Using the maximum expected value of shear, the sphere must be capable of rotating at a rate of 0.131 rad/sec or 7.5 deg/sec.

8.5.3 Vibration

According to p. 16 of Ref. 54 a random noise vibration test level for the Saturn is 7.5 to 12.0 g, in the range of 20 to 2000 cps. This environment if encountered in flight could enter as an erroneous signal to the pickoff.

8.5.4 Sustained Acceleration

The burning of the fuel will cause an increasing acceleration which will have a maximum value at first stage burnout. The component of vehicle acceleration perpendicular to the diaphragm of a membrane-type differential gage mounted in the duct will be

$$a_D = a_v \sin\theta$$

where a_D = acceleration perpendicular to diaphragm

a_v = vehicle acceleration

θ = angle subtended by diaphragm and vehicle axis

8.5.5 Wind Pressure

The pressure detector will sense no pressure differential when the sphere is aligned correctly with the wind. Theoretically

the pressure varies as the cosine squared of the angle from the stagnation pressure at the foremost point to ambient at the equator. Aft of the sphere equator, or at angles greater than 90 degrees, a wake forms and the pressure is not accurately known. For the purposes of this analysis, however, it is assumed that a vacuum is formed on the leeward which is equal in magnitude to the increase of pressure on the windward side. The differential pressure at either end of a diameter of the sphere at the equator due to a shift in the direction of the remote relative wind is formulated below. This shift in resultant wind direction is illustrated in Figs. 37 and 38.

$$P_D = 2P_S \cos^2 (90-\delta) = 2 \sin^2 \delta$$

where P_D = differential pressure
 δ = shift of resultant wind

A one degree resultant windshift would result in a differential pressure of 6.1×10^{-4} times the stagnation pressure.

8.5.6 Pressure Equivalent of Acceleration

The following relationships derive the equivalent differential pressure produced by sustained acceleration.

$$P = \frac{F}{A} = \frac{ma}{A} = \frac{(W/g_0)a}{A} = \frac{w A t}{A} \frac{a}{g_0} = w t \frac{a}{g_0}$$

where P = pressure, psi
 F = force, lb
 A = area, in²
 m = mass, slugs
 a = acceleration, ft/sec²
 g_0 = gravity 32.2 ft/sec²
 w = specific weight, lb/in³
 t = thickness, in
 g = acceleration, gravities

The maximum component of acceleration normal to the diaphragm is 1.66 g and occurs when the angle of attack is 27 degrees and the vehicle acceleration is 35.98 m/sec², occurring at 49.6 km altitude.

8.5.7 Pressure Equivalent of Vibration

The pressure detector is assumed to be a diaphragm which responds to vibration as a second-order linear system. According to Deu Hartog's "Vibration Problems in Engineering," the lowest natural frequency encountered by a circular diaphragm is

$$\omega_n = 2.4 \frac{T}{\mu r^2}$$

where ω_n = natural frequency (rad/sec)

T = membrane tension (lb)

μ = mass per unit area (slugs/in²)

solving for T

$$T = 6.82 \mu r^2 f_n^2$$

where f_n = natural frequency in cycles per second.

Thus, the natural frequency can be adjusted by varying the tension.

When the diaphragm is excited by a sinusoidally varying force $F = F_0 \sin \omega t$, it will respond with peak deflections greater than those caused by an equivalent static force F_0 . The ratio of dynamic deflection at any frequency f or ω to static deflection is given by the relation:

$$\frac{d_{\text{dynamic}}}{d_{\text{static}}} = \frac{1}{1 - (f/f_n)^2} = \frac{1}{1 - (\omega/\omega_n)^2}$$

8.5.8 Pressure Sensor

One method of sensing a difference in pressure at each end of a duct is to use a pivoted vane which divides the duct and is

free to rotate in the direction of lower pressure. A mirror could be attached to the vane to reflect light from a lamp onto a photocell. As the vane deflects the photocell output would depart from the null, and this departure would be used to drive servomechanism amplifiers. Flexure pivots should be used rather than bearings in order to minimize static friction. The pivots and the vane must be structurally rigid to withstand accelerations due to gravity, vehicle acceleration and vibration.

An alternate method of detecting the differential pressure is a flexible diaphragm which divides the duct into two halves. An optical or capacitance data pickoff could be used. The diaphragm possesses the advantages of less mass and faster time response, and it has simpler structural requirements than the stiff vane since it does not fail by buckling. Accordingly, a diaphragm was selected for evaluation. A 1-inch circular diaphragm of polyethylene terephthlate (Mylar) 0.00025 inch thick was analyzed and the deflection, d, and stress calculated by the following equations:

$$\begin{aligned} \text{deflection} &= 0.0525 \sqrt[3]{p} \\ \text{stress} &= 5320 p^{2/3} \end{aligned}$$

where p is the pressure.

8.5.9 Deflection Due to Wind

The deflections and stresses are tabulated below for the model diaphragm when the sphere is exposed to a 1 degree change in resultant wind.

<u>ALTITUDE</u> (km)	<u>DIFFERENTIAL</u> <u>PRESSURE</u> (μ psi)	<u>DIAPHRAGM</u> <u>DEFLECTION</u> (inches)	<u>DIAPHRAGM</u> <u>STRESS</u> (psi)
30	820	0.0049	46.0
40	295	0.0035	23.5
47	149	0.00276	15.0
55	70	0.00216	9.1
68	13.2	0.00124	2.9
88	3.95	0.00083	1.3
100	0.395	0.00039	0.3

8.5.10 Deflection Due to Sustained Acceleration

The component normal to the diaphragm of the maximum sustained acceleration which is expected to be encountered is 1.66 g. This occurs about 49.6 km. Using the equation developed in Section 8.5.6, the equivalent differential pressure produced by sustained acceleration is 19.9μ psi on the model diaphragm, and the resulting deflection is 0.0015 inches.

8.5.11 Deflection Due to Vibration

The dynamic deflection due to vibration is given by the formula in Section 8.5.7. Engineering judgement is used to set the dynamic-static displacement ratio at about 1.04. This occurs at a frequency of $0.2 f_n$. The environment requires an upper frequency limit of 2000 cps. Therefore the diaphragm natural frequency must be 10,000 cps. This can be provided by adjusting the diaphragm tension to 5.2 lb/in. The maximum vibration encountered is 5.0 g. If this were static, it would be equivalent to a pressure of 62.5μ psi, causing a deflection of 0.00208 inches. The deflection ratio of 1.04 raises the deflection to 0.00215 inches.

9. VEHICLE AND ENVIRONMENT

This study was made for large, liquid-fueled launch vehicles in general, rather than for any one in particular. The Atlas-Centaur, Saturn and Nova are vehicles of this type. In order to establish the requirements imposed on the measurement system by the vehicle it was necessary to establish a model trajectory which is reasonably representative of large launch vehicles. Typical launch vehicle configuration and characteristics are contained in this section (Figs. 41, 42).

TABLE X
BOUNDARY LAYER THICKNESS (INCHES)

Saturn Missile Station	Mach 2.17	Mach 4.238	Mach 6.37	Mach 7.8
Third Stage C-5 3762	1.9	2.94	5.2	6.6
3411	5.0	8.75	14.6	17.8
3255	6.5	11.0	18.7	23.9
2732	9.85	16.7	28.6	35.9
2519	11.6	20.0	34.2	43.3
First Stage F-1-C				
365	23.7	39.8	67.5	86.0

*Saturn V Boundary Layer Estimates and Shock Patterns. NASA-GMSFC
Coordination Sheet No. AERO-H-192, May 22, 1963.

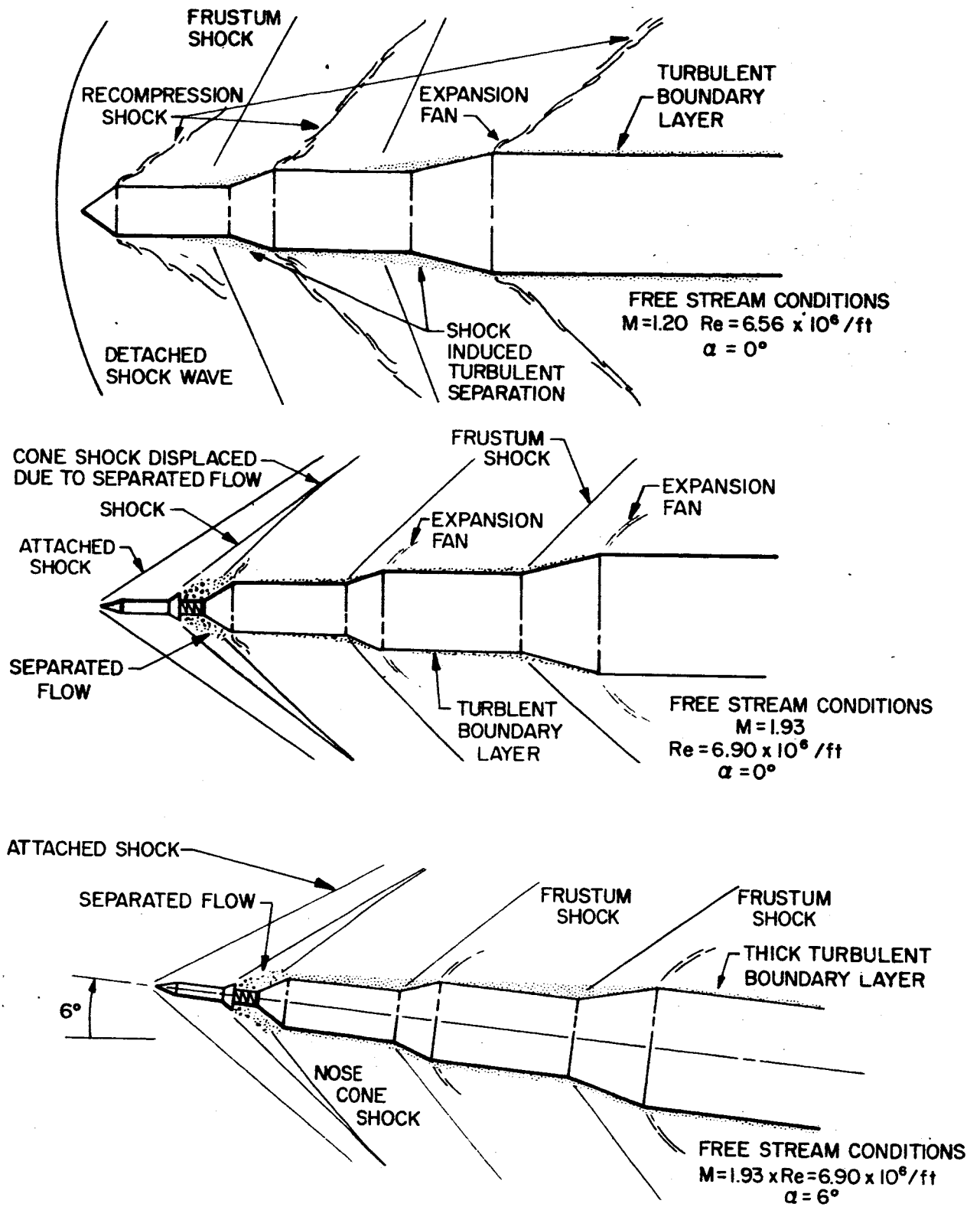


FIG. 41 LARGE LAUNCH VEHICLE CONFIGURATION

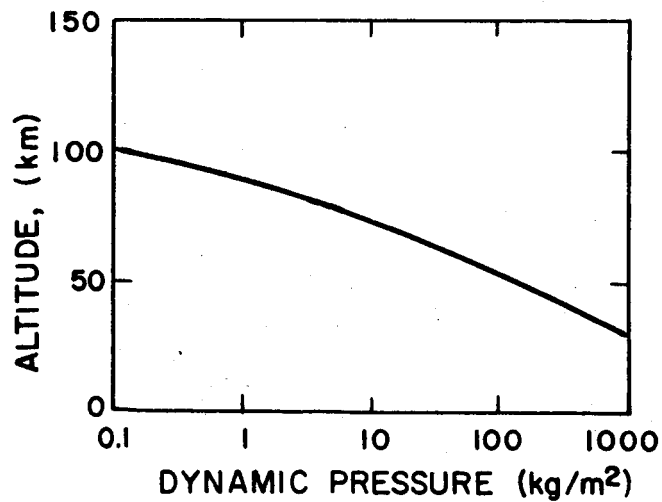
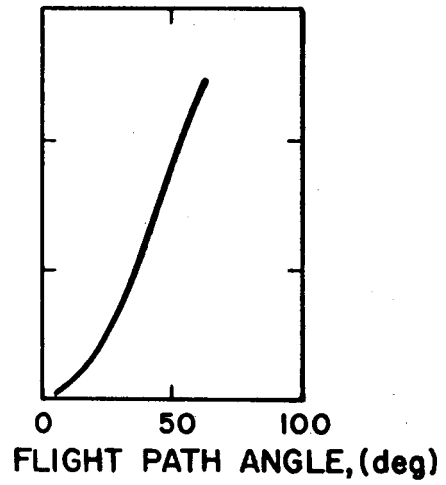
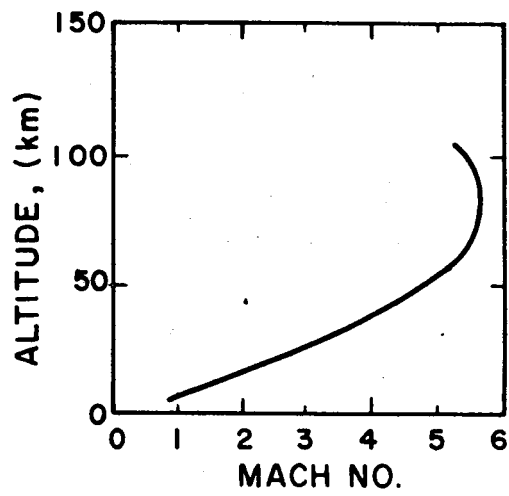
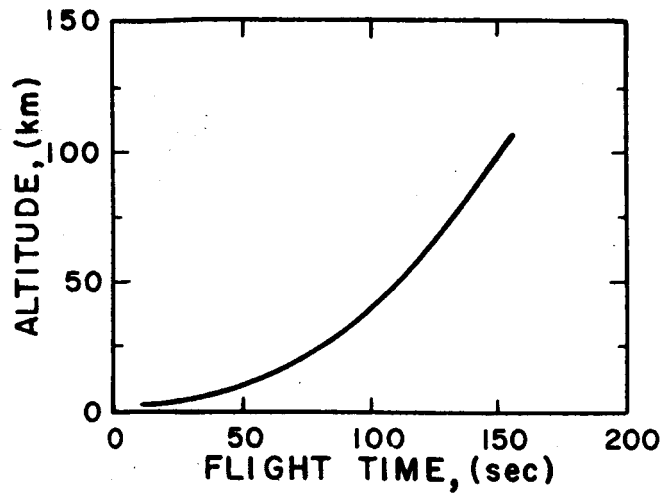


FIG. 42 MODEL LAUNCH VEHICLE PERFORMANCE DATA

REFERENCES

1. U. S. Standard Atmosphere, 1962, Committee on Extension to the Standard Atmosphere, Superintendent of Documents, U. S. Govt. Printing Office, Washington 25, D.C.
2. Ragsdale, G.C. and Wasko, P. E., "Wind Flow in the 80-400 km Altitude Region of the Atmosphere," NASA TN D-1573, March 1963.
3. White, Charles E., "Measurement Standards," Space/Aeronautics, October 1962, Part 2.
4. Survey of Pressure and Density Sensors for the N.O.L. HASP Program, Final Report, Wright Instruments, Inc., NOL-N 60-21-5603, April 1959.
5. Survey for Naval Ordnance Laboratory of High Altitude Atmospheric Temperature Sensors, Final Report, Wright Instruments, Inc., N-60921-6136, 1961.
6. Robinson, E., "New Meteorological Sensors to 150,000 Feet, Part I: Survey, Part II: Analysis;" Stanford Research Instruments, Proj. No. PAU-3692, April 1962 and September 1962. AD 284318
7. George, J.L. and Peake, W.H., "Survey of the Literature on Temperature Determination at Altitudes About 120,000 Feet," Ohio State University Research Foundation, Rept. No. 973-1, 15 February 1960. AD 235897
8. Hane, T.G., et al., "Preliminary Analysis of Methods for Temperature Determination at Altitudes Above 120,000 Feet, Ohio State University Research Foundation Rept. No. 973-2, 25 May 1960. AD 242206
9. Final Engineering Report - Temperature Measurements Above 120,000 Feet, Ohio State University Research Foundation Rept. No. 973-3, 1 September 1960. AD 252143
10. Kalinovskiy, A.B., and Pinus, N.Z., "Soviet Aerological Measurement," U.S. Dept. of Commerce JPRS Doc. No. 16691, 17 December 1962. AD 292217
11. Project Aries (Atmospheric Research Information Exchange Study), Science Communications, Inc., Final Report, Submitted to Office Naval Research under Contract No. 3071(00), 1 August 1960.
12. Marquardt, J.F., et al., "Study of Methods for Measurement of Atmospheric Parameters at Supersonic Speeds," Booz-Allen Applied Research, Inc., WADD Tech. Rept. 60-524, Prepared under Contract No. AF 33(616)-6273, July 1960.

13. Farrah, H.R., et al., "Study of Instrumentation for a Space Simulation Chamber," The Bendix Corp., Tech. Documentary Rept. No. AEDC-TDR-62-161, August 1962. AD 282518
14. Annals of IGY, 1958, Vol. VI, Pergamon Press, London, New York.
15. USAF Handbook of Geophysics; prepared by Geophysics Research Directorate ARDC, Chapter, "Luminance of the Atmosphere," The Macmillan Company, New York, Revised edition, 1960.
16. IGY World Data Center Rocket and Satellites, IGY Rocket Report Series No. 1, 30 July 1958.
17. Mass Spectrometer for Upper Air Measurements ARSJ Dec. 1961, p. 1773.
18. Rocket Exploration of the Upper Atmosphere, edited by R.L.F. Boyd and M.J. Seaton - Pergamon Press, Ltd., 1954, p. 43.
19. Pressure, Densities, and Temperature, Phys. Rev. 88, 1027-1032, December 1952.
20. Journal of Geophysical Research, Vol. 66, July-December 1961, p. 3191.
21. Space/Aeronautics Part 2, October 1962 (A Conover-MAST Publication)
22. Temperature, Its Measurement and Control in Science and Industry, Vol. 2, American Institute of Physics, Reinhold, p. 435.
23. Ainsworth, J.E., Fox, D.F., and LaGow, H.E., "Measurement of Upper Atmosphere Structure by Means of the Pitot Static Tube," NASA TN D-670, February 1961.
24. Spencer, N.W., "Research in Measurement of Ambient Pressure, Temperature and Density of the Upper Atmosphere by Means of Rockets," University of Michigan, Engr. Res. Inst. Report 2096-18-F, June 1958. AD 203-480
25. Ratcliffe: Physics of the Upper Atmosphere, 1960.
26. Nordberg, Wilhelm, "Present State of Experimental Research in the Mesosphere," Paper read at Meteorological Support for Aerospace Testing and Operation Meeting, Fort Collins, Colorado, 12 July 1963.
27. Miers, B.T. and Byers, N.J., "Rocketsonde Wind and Temperature Measurements Between 20 and 70 km for Selected Stations," Paper read at Meteorological Support for Aerospace Testing and Operation Meeting, Fort Collins, Colorado, 12 July 1963.
28. Masterson, J.W., Specification No. DRS-RD-G318-62, Hq. Pacific Missile Range, Pt. Mugu, California.
29. Swalley, Frank E., "Measurement of Flow Angularity at Supersonic and Hypersonic Speeds with the Use of a Conical Probe," NASA L-1216, 1961.

30. Cheng, Hsien K., "Hypersonic Shock-Layer Theory of a Yawed Cove and Other Three-Dimensional Pointed Bodies," WADC TN 59-335, U.S. Air Force, October 1959; Errata, June 1960.
31. Hinteregger, H.E., "Preliminary Data on Solar Extreme Ultraviolet Radiation in the Upper Atmosphere," J. of Geophysical Research, Vol. 66, No. 8, p. 2373, August 1961.
32. Judge, D.L., A.L. Morse, and G.L. Weissler, "Wavelength Analysis of Fluorescence from Gases Excited by Vacuum Ultraviolet Radiation," in a paper presented by the University of Southern California and prepared for the Upper Atmosphere Physics Laboratory, Air Force Cambridge Research Laboratories, USAF, Bedford, Mass., (unpublished).
33. Hass, G. and R. Tousey, "Reflecting Coatings for the Extreme Ultraviolet," J. Opt. Soc. Am., Vol. 49, No. 6, pp. 593-602, June 1959.
34. Ratcliff, A., "Physics of the Upper Atmosphere," Academic Press, Inc., New York, 1960.
35. American Institute of Physics Handbook, American Physical Society, 1960.
36. Newport, W.M. and W.E. Behring, Jour. Quantitative Spectroscopy and Radiative Transfer, Vol. 2, pp. 527-532, 1962.
37. Naval Research Laboratory Report 5608, July 21, 1961.
38. Byram, E.T., et al., Journal Geophysics Research, Vol. 61, 251, 1956.
39. Hakewessell, D., Air Density Measurement, Giainni Controls Corp., Technical Notes, No. 1, 1963.
40. Spencer, N.W., et al., "A Radioactive-Ionization Gage Pressure Measurement System," ERI, University of Michigan Sci., Report ES-1, May 1958.
41. Spencer, N.W., et al., "On the Use of Ionization Gage Devices at Very High Altitudes," ARS Journal, Vol. 1, No. 4, April 1959.
42. LaGow, H.E., R. Horowitz and J. Ainsworth, "Arctic Atmosphere Structure to 250 km Planetary and Space Science, Vol. 2, No. 1, October 1959.
43. Liu, V.C., "On Pitot Pressure in an Almost-Free-Molecule Flow - A Physical Theory for Rarefied Gas Flows," Jour. of the Aero/Space Sciences, Vol. 25, No. 12, pp. 779-85, December 1958.
44. Methods of Measuring the Upper Atmosphere, AFCRL Report 62-1021, August 1962. AD 295552
45. Dow, W.G. and N.W. Spencer, "The Measurement of Ambient Pressure and Temperature of the Upper Atmosphere," AFCRL Project M824, August 1953. AD 26616

46. Nagy, A.F., et al., "Measurements of Atmospheric Pressure, Temperature and Density at Very High Altitudes," University of Michigan College of Engineering, August 1961.
47. Arnold, A., "The Pressure-Versus-Height Relationship, A Measurement Question," USASRDL Tech. Rept. 2165, January 1961. AD 251541.
48. Belcher, J.T. and Gilbert, B.S., Qualification of F-16 Q-Ball and Total Temperature Measurements On-Board Vehicle SA-4, NASA-GMSFC MTP-AERO-63-57, July 1963, Conf.
49. Glass, D.R., Methods for Measuring Ambient Air Temperatures from High Speed Aircraft, Univ. of Michigan Engineering Research Inst., WADC Tech. Rept 57-705, Dec. 1957. AD 142169.
50. Barnes, T.G. and McDonald, C., Determination of Atmospheric Parameters by Acoustic Means, Schellenger Research Lab., Texas Western College Progress Rept. I, July 1962. AD 297431
51. Ruskin, R.E., et al., Development of the NRL Axial-Flow-Vortex Thermometer, Naval Research Rept. 4108, September 1952. AD 16694
52. Astheimer, R.W., An Infrared Radiation Air Thermometer, Barnes Engineering Co. Technical Paper, Stamford, Conn., October 1962.
53. Baur, J.P. and Belcher, J.T., F-16 Q-Ball Data Reduction Technique and Angle of Attack Evaluation on Saturn SA-4, NASA-GMSFC MTP-AERO-63-48, June 1963.
54. Environmental Test Specification for Saturn C-1 Block II, ASTR-TSR-1-62, Prepared by Reliability Office Astrionics Division, Marshall Space Flight Center, May 11, 1962.

APPENDIX

FILTERPHOTOMETRIC METHOD OF DENSITY DETERMINATION FOR THE CASE WHERE THE SUN IS LOW ON THE HORIZON

The method of determination of atmospheric density discussed in Section 5.2 is based on the assumption that the sun is directly overhead. Since large liquid-fueled vehicles usually are launched shortly after sunrise to avoid vehicle warping due to differential solar heating of the fuel tanks, the sun is near the horizon rather than overhead. The absorption, then, takes place horizontally through concentric spherical segments of the atmosphere rather than vertically through elements which, for all practical purposes, are rectangular parallelepipeds. A method of determining relative density using the Abel integral approach for the case of spherically symmetric shells of uniform density is presented here. Scattering is neglected.

From Beer's law the fractional decrease in intensity of electromagnetic radiation per unit path length is a constant. This constant is the product of the density $\rho(r)$ of the absorbing species at a distance r from the center of symmetry and the mass absorption coefficient μ , or

$$\frac{dI}{I dx} = - \mu \rho(r) \quad (1)$$

If the unattenuated intensity of the monochromatic radiation is I_0 and if the intensity detected at P of Fig. A-1 by the rocket at a distance y from the earth's center is $I(y)$, then

$$\int_{I(y)}^{I_0} \frac{dI}{I} = -\mu \int_0^{\infty} \rho(r) dx$$

or
$$\ln I_0 - \ln I(y) = -\mu \int_0^{\infty} \rho(r) dx \quad (2)$$

This equation contains the quantity $\ln I(y)$ which one can measure and $\rho(r)$ which one wants to know. It is an integral equation of the Abel type and suggests the inversion (Ref. 1):

$$\rho(r) = \frac{2}{\pi\mu} \int_r^{\infty} \left[\frac{d}{dy} \ln I(y) \right] \frac{dy}{\sqrt{y^2 - r^2}} \quad (3)$$

An example of how a numerical integration of the above equation may be performed follows (Ref. 2). Other methods appear in the literature (Ref. 3).

To derive $\rho(r)$ from the measured function $I(y)$ introduce a new variable Z defined by

$$Z = \sqrt{y^2 - r^2} \quad (4)$$

Substituting Eq. 4 into Eq. 3 we obtain

$$\rho(r) = \frac{2}{\pi\mu} \int_0^{\infty} \left[\frac{d}{dy} \ln I(y) \right] \frac{dZ}{y}$$

For the numerical integration one has to differentiate the measured function $\ln I(y)$ and for a certain r value (i.e. $r = r_1$) plot the function:

$$\frac{1}{y} \frac{d}{dy} \ln I(y)$$

as a function of the variable Z . The area under this curve from $Z = 0$ to $Z = \infty$ represents the relative density of the atmospheric shell of radius r_1 . The data reduction procedure would be as follows:

1. Plot $\ln I(y)$ from observed data. A typical result is sketched in Fig. A-2.
2. Plot $\frac{1}{y} \frac{d}{dy} \ln I(y)$ from step 1. A typical result is depicted in Fig. A-3.
3. Plot $\frac{1}{y} \frac{d}{dy} \ln I(y)$ versus Z for $r = r_1$, selecting convenient intervals along Z axis from the relation,

$$Z = \sqrt{\frac{y^2 - r_1^2}{1}}$$

Substituting the various conveniently spaced values of Z will give various values of y from the above relation. The value of the function $\frac{1}{y} \frac{d}{dy} \ln I(y)$ can be read from Fig. A-3 and plotted as Fig. A-4.

Additional discussions of the use of this method in other fields are contained in Refs. 4 through 8.

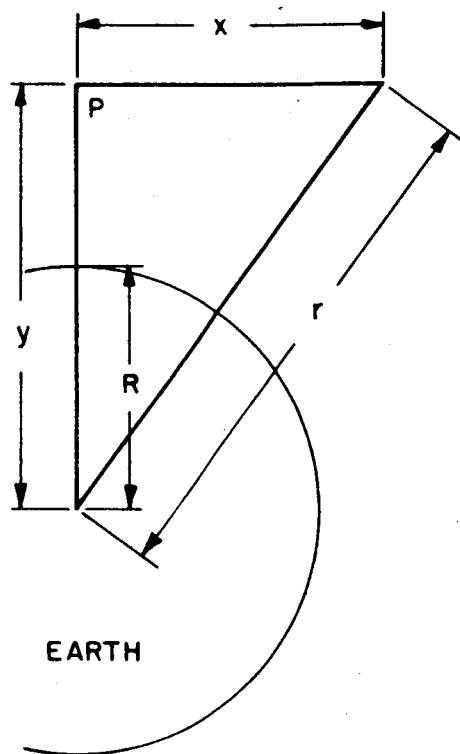


FIG. A-1

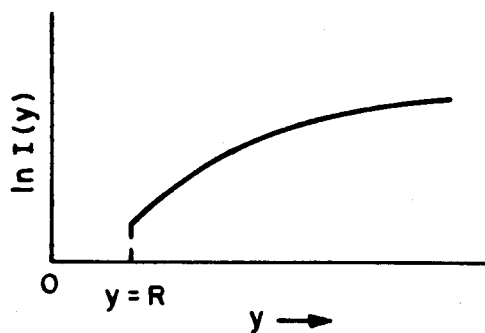
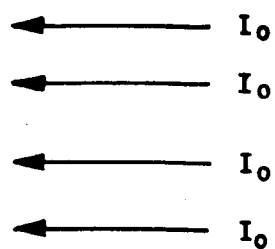


FIG. A-2

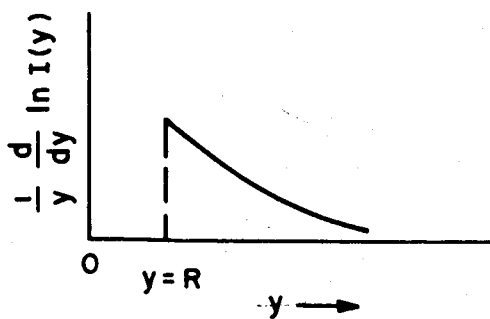


FIG. A-3

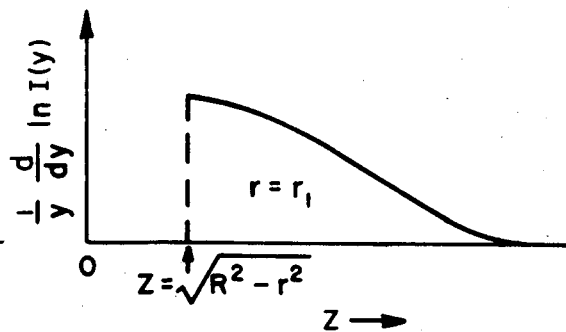


FIG. A-4

REFERENCES FOR APPENDIX

1. See for example: E. T. Whittaker and G. N. Watson, A Course of Modern Analysis (Cambridge University Press, 1920) p. 229
2. W. Elenbaas, The High Pressure Mercury Vapor Discharge (North-Holland Publishing Company, 1951) p. 14
3. R. W. Fowler, Statistische Mechanik (Leipzig, 1931)
4. A. Unsold, Physik Der Sternathos Pharen (Berlin, 1938)
5. W. Larenz, Z. Physik, 129, 1951, pp. 327-342
6. W. J. Pearce, Plasma-Jet Temperature Measurement, Optical Spectrometric Measurements, ed. by D. D. Dickerman (The University of Chicago Press, 1961) p. 135
7. H. N. Olsen, The Physics of Fluids, Vol. 2, 1959, pp. 614-623
8. F. C. Hurbut, J. App. Phys. Vol. 30, 1959, pp. 273-279